Title

Electrochemistry of two-dimensional electrodes with moir′e superlattices

Author

Zhang, Kaidi

Publication Date

2024

Peer reviewed|Thesis/dissertation

Electrochemistry of two-dimensional electrodes with moiré superlattices

by

Kaidi Zhang

A dissertation submitted in partial satisfaction of the

requirements for the degree of

in

Chemistry

in the

Graduate Division

of the

University of California, Berkeley

Committee in charge:

Professor Kwabena D. Bediako, Chair
Professor Jeffrey Long
Professor James Analytis

Spring 2024

Electrochemistry of two-dimensional electrodes with moiré superlattices

Abstract

Electrochemistry of two-dimensional electrodes with moiré superlattices

by

Kaidi Zhang

in Chemistry

University of California, Berkeley

Professor Kwabena D. Bediako, Chair

In this thesis, we explore the novel electronic properties and reactivity of twisted bilayer and trilayer graphene (tBLG and tTG), and twisted bilayer transition metal dichalcogenides (TMDs) through systematic theoretical and experimental studies. We demonstrate that rotational misalignment in these materials leads to significant changes in their electronic band structures, primarily through the formation of flat bands at certain 'magic' angles. These flat bands result in enhanced electron correlation effects and localized electronic states that significantly alter the materials' electrochemical and electronic properties. For graphene-based systems, we have found that the electron transfer kinetics at the electrode-electrolyte interface can be tuned by manipulating the twist angle between the layers. This effect is more pronounced in trilayer graphene, where we discovered that localization of electronic density of states plays a significant role in altering electron transfer kinetics. This finding aligns with the conventional understanding of how defects enhance electrochemical activity. However, in trilayer systems, we extend that understanding to consider the lateral proximity of electronic density of states, hinting at the importance of surface density of states in influencing reactivity. In the case of TMDs, our investigations suggest that twisting can similarly modulate electronic properties and potentially improve catalytic activities, particularly for hydrogen evolution reactions, a critical reaction for hydrogen production in clean energy technologies. We delve into novel methods to probe hydrogen evolution on moiré superlattices of TMDs, noting the limitations and challenges encountered. This thesis enriches our understanding of moiré materials and lays the groundwork for future innovations in the field of moiré catalysis.

To

everyone who helped me;
everyone who accompanied me;
everyone who expects highly of me;
everyone who drives me forward by example.

"It's not who I am underneath, it's what I do that defines me."
-Bruce Wayne, aka. Batman

Contents

List of Figures

List of Tables

Acknowledgments

I am profoundly grateful to my parents for their unwavering support and nurturing, which have made it possible for me to freely chase my dreams. My scientific journey has been deeply influenced by my mentors and advisors, whose guidance has been invaluable. I extend my deepest appreciation to my advisor, Kwabena Bediako, for continually inspiring me to grow as a scientist and for providing myriad opportunities over the past five years that have significantly enhanced my skills and critical thinking. I am immensely grateful.

My journey into scientific research began under the guidance of my undergraduate advisor, Kenneth Poeppemeier, who provided the foundational environment for my career. Within his lab, my mentor Justin Hancock showed immense patience and dedication. Justin, thank you for your guidance and for introducing me to the life of a graduate student and the core of scientific inquiry.

I also owe much to my mentor Yun Yu, whose patience and perseverance have deeply influenced my approach to scientific challenges and were crucial in advancing my projects.

I am thankful for my colleagues in the Bediako lab—Lilia Xie, Valerie McGraw, Jonathon Nessralla, Samra Husremovic, Madeline Van Winkle, Matthew Erodici, Zhizhi Kong, Oscar Gonzalez, Isaac Craig, Sonal Maroo, Shannon Fender, Garrett Hegel, and Sifei Du. Your support and advice have been indispensable. Special thanks to Matt and Zhizhi from my cohort for their exceptional support and friendship. To Sonal, Matt, and Zhizhi, sharing our lab suite has been one of the most enjoyable aspects of my daily lab life. To my skiing buddies—Zhizhi, Lilia, Matt, Isaac, Shannon, Garrett, and Sifei—I cherish our shared hobby and look forward to more adventures on the slopes. To my gaming buddies, Oscar and Garrett, keep practicing; I look forward to our next Smash Bros matchups!

My role as a Graduate Student Instructor was enriched by Jon Rittle and Saul Perlmutter, who entrusted me with significant teaching responsibilities that were both challenging and fulfilling. I also want to recognize my lab mentee, Bryan Junsuh Kim, for his collaboration on the trilayer project. Bryan, I wish you the best in your future scientific endeavors.

Finally, I am grateful to my long-time friends—Ruiqi, Lin, Tianhan, Yiyun, Coco, Boyang, Zinan, Alan, Daniel, Nicole, Ziyi, and Wenyi—and to my new friends who have welcomed me with warmth and support. To Jonathon Tsao and Allison Schmitt, thank you for your immense help as I transition to the next chapter of my life. Your friendship has exemplified the true meaning of community and support.

Chapter 1

Overview and introduction

1.1 Growing importance of innovation in energy conversion devices

In the landscape of modern technology, tackling the substantial challenge of improving energy conversion efficiency while simultaneously reducing environmental emissions is critical.[24] The progression towards sustainable energy production and storage is increasingly dependent on the development and deployment of novel materials that can enhance electron transfer reactions.[74, 145] The discovery and application of such materials rely heavily on an in-depth understanding of the kinetics of reactions and the precise engineering tailored to optimize these reactions for specific applications.[151, 47, 29] At the heart of these technological advances are systems like electrochemical catalysts, fuel cells, and metal-air batteries, which fundamentally operate based on heterogeneous interfacial reactions.[74] This underscores the essential nature of both theoretical and experimental insights into these reactions, highlighting their significance in driving forward more efficient and environmentally benign energy solutions.

1.2 Electron transfer reactions and models to understand them

Heterogeneous electron transfer (HET) reactions, essential in the realm of electrochemistry, occur at the solid-liquid interface and are broadly categorized into two types: outer-sphere and inner-sphere. These classifications, which were initially applied to homogeneous electron transfer among metal complexes by Nobel laureates Marcus and Taube, provide a useful framework for understanding the kinetics of HET reactions. [27, 161]

In inner-sphere HET reactions, similar to their homogeneous counterparts, a central metal atom or a bridging molecule, ion, or ligand in a reactant or product molecule makes direct contact with the electrode surface. This direct contact facilitates electron transfer between the reactant and the electrode. This mechanism is particularly crucial in important electrocatalytic reactions for energy conversion, such as the oxygen evolution reaction (OER) and hydrogen evolution reaction (HER),

which proceed through an inner-sphere pathway. [4, 144]

Conversely, outer-sphere HET reactions involve an intervening layer of solvent molecules, constituting the Inner Helmholtz Plane (IHP). Here, the reactant or product species is positioned in the Outer Helmholtz Plane (OHP) of the Electrical Double Layer (EDL), outside the solvent layer and immediately adjacent to the electrode surface. Electron transfer in this scenario occurs via a tunneling process or electron hopping between the reactant or product in the OHP and the electrode surface adjacent to the IHP. [4, 25]

It is rare for a reaction to be universally categorized as purely outer-sphere or inner-sphere. However, understanding these distinctions is critical for enhancing our grasp of the kinetics and mechanisms underlying HET reactions. [18]

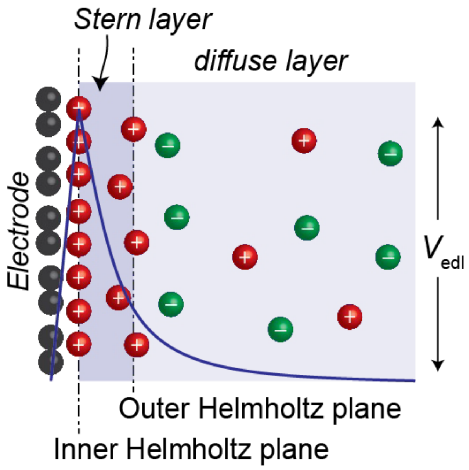

Figure 1.1: Structure of the electrical double layer electrified at a solid–electrolyte interface for outer-sphere HET, showing the potential drop across the interface (blue line). The voltage consumed due to the double layer capacitance is V_{edl}.

Schmickler and Santos highlighted the hexaaminеruthenium(III/II) chloride ($Ru(NH_3)_6^{3+/2+}$) and various iron(II/III) complexes as exemplary outer-sphere heterogeneous electron transfer (HET) systems.[144, 18] These well-characterized redox probes, including ferrocene ($Fe^{0/+}$) in non-aqueous solutions, play pivotal roles in studying processes critical for energy conversion and environmental science.[18]

One of the key applications of these outer-sphere redox systems is in the measurement of the electrochemically active surface area (EASA), which relies on reversible electron transfer processes that are purely diffusion-controlled. A simple one-electron transfer reaction, such as that involving the ferrocyanide ion ($Fe(CN)_6^{2+/1+}$), is typically used to determine the active electrode surface

area.[46, 208] This is done through cyclic voltammetry combined with the Randles-Sevcik equation, assuming the diffusion coefficient of the redox couple is accurately known.[4]

Furthermore, the efficiency of electrodes made from new materials can be assessed using outer-sphere HET. By understanding the electrode properties through studies of HET, several models have been developed to characterize the kinetic behavior at this interface, providing insights necessary for optimizing electrode design and enhancing their performance in various applications.[191]

Marcus theory provides a powerful framework for understanding homogeneous outer sphere electron transfer reactions between two chemical species.[112] Likewise, Gerischer's seminal formulation, describes the HET rate constant, k_{ET}, in the weak coupling (outer-sphere) limit as shown in equation 1.1 [51]:

$$k_{ET} = \nu_n \int_{-\infty}^{\infty} \varepsilon(E) f(E) DOS(E) W_{ox}(\lambda, E) dE \tag{1.1}$$

where ν_n is the nuclear frequency factor, $\varepsilon(E)$ is the proportionality function, $f(E)$ is the Fermi function, $DOS(E)$ is the density of states of electrode, $W_{ox}(\lambda, E)$ is the probability density function of the reactant and λ is the reorganization energy. In this model, illustrated in Figure 1.2, the electron transfer rate for an oxidation (reduction) reaction is proportional to the probability of finding an occupied (empty) state of some specified energy in the solution and the probability of finding an empty (occupied) state of that energy in the electrode/metal.

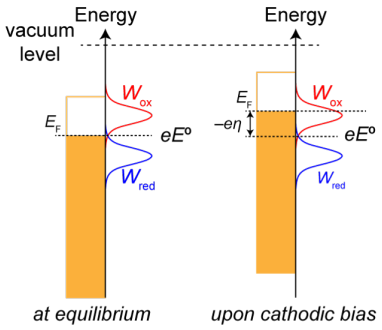

figure 1.2: Schematic of Gerischer's model, illustrating the Fermi level of the metal electrode (E_F) in relation to the probability distributions of occupied (W_{red}) and empty (W_{ox}) states in solution at equilibrium and after applying a cathodic overpotential, η.

For bulk metals, varying the electrode potential changes the driving force of the reaction by electrostatically moving the entire band manifold of the electrode relative to the donor/acceptor states of the dissolved molecule. In this bulk metal case, the Fermi level position (E_F) within the band does not change appreciably. The Gerischer model has also been popular in semiconductor electrochemistry where an applied electrochemical bias alters the degree of band bending and the densities of electrons and holes at the semiconductor–solution interface, but not the position of the band edges at the semiconductor–solution interface.[144]

The complexities increase in the electrochemistry of two-dimensional (2D) materials, which are elaborated upon in Chapters 2 and 3. This sophisticated approach underscores the critical role of understanding kinetic behaviors at the electrode interface for advancing electrochemical technologies.

Electronic factors delineated in the Gerischer model extend beyond outer-sphere charge transfer, providing valuable insights into the broader scope of electrochemical processes. Schmickler's theory of electrocatalysis is particularly notable, addressing how electrochemical reactions occur in the strong-coupling (inner-sphere) limit.[144, 139, 141, 142] This involves the adsorption of an intermediate at the electrode, a common feature in electrocatalysis, which is significantly influenced by the structure and dispersion of the electronic bands in the electrode near the Fermi level (E_F).

Schmickler's model challenges the traditional view of the metal electrode merely acting as an electron reservoir, as posited by the wide-band approximation. Instead, it highlights the critical role of d-bands with a significant density of states (DOS) near E_F for optimal catalytic activity. The theory emphasizes that the strong coupling of these narrow bands to reactant states near E_F is essential for efficient catalysis. This is because such a configuration facilitates effective electronic interactions between the electrode and the transition states of the adsorbed intermediates, enhancing the electron transfer processes crucial for catalytic reactions. [141]

The nuances of these interactions, where the coupling between the electrode surface and the transition states of intermediate formation takes center stage, will be elaborated in Chapter 4. This discussion will delve deeper into the molecular dynamics and electronic structure considerations that define the effectiveness of electrocatalysts, underscoring the sophisticated interplay between electronic properties and catalytic performance.

1.3 Two-dimensional electrode offers unparalleled degrees of freedom for tuning electron transfer reactions

The advancement of electrode surfaces for HET is anchored in the discovery of materials that enable direct electron transport across a solid-liquid interface with minimal energy barriers, as well as the capability to selectively stabilize or destabilize specific intermediate states, directing the most efficient pathway to a desired product. Van der Waals (vdW) or two-dimensional (2D) materials, like graphene and transition metal dichalcogenides (TMDs), are at the forefront of this endeavor due to their distinctive properties.

Graphene, first isolated in 2004[49], exemplifies the remarkable potential of 2D materials in various disciplines, from electronics to electrochemistry. Graphite, the bulk form of graphene, consists of Bernal-stacked (i.e. AB-stacked) graphene, where half of the carbon atoms in the adjacent layers sit on top of the empty centers of hexagons in the other layer.[185] One-atom-thick carbon lattice of graphene (see Figure 1.3a) offers high electrical and thermal conductivities, key for rapid electron transport.[156] However, the delocalized π bonding network across its basal plane typically results in weak adsorption energy for reaction intermediates, presenting a challenge for its electrocatalytic activity.[73] Despite this, graphene's edge sites and doped versions exhibit increased

activity due to a higher density of states at the Fermi level, improving its suitability for outer-sphere charge transfer reactions and processes like the hydrogen evolution reaction (HER).[56, 73, 204]

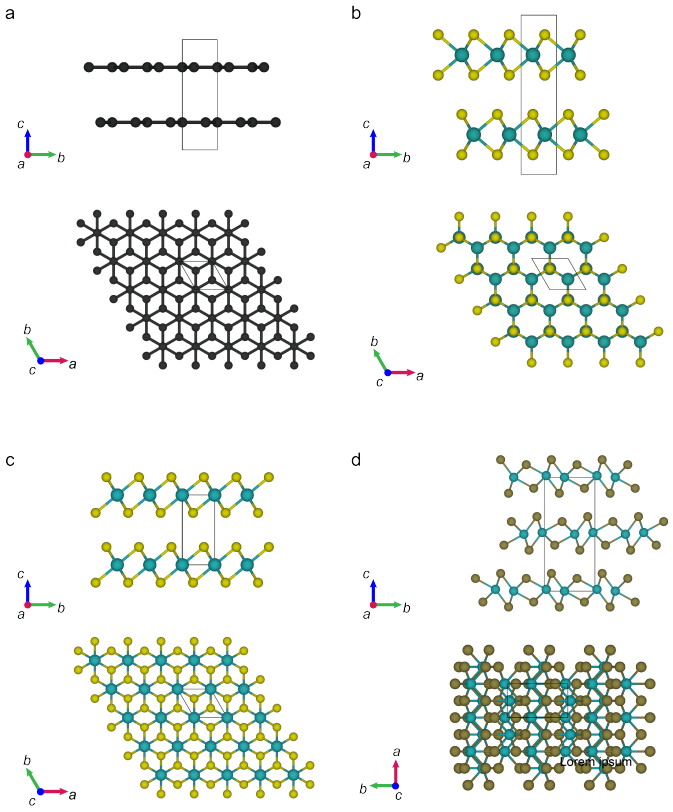

figure 1.3: The crystal structure viewing down from the a and c axis of **a** graphene **b** 2H phase MoS_2 as a typical 2*H* phase TMD **c** 1*T* phase MoS_2 as a typical 1*T* phase TMD **d** $1T'$ phase $MoTe_2$ as a typical $1T'$ phase TMD. The black rectangles/parallelograms represent the unit cell of the crystal in different perspectives.

In the realm of TMDs, characterized by the general formula MCh_2 where M is a transition metal and Ch is a chalcogen, the ability to exist in different structural phases—such as the trigonal prismatic 2*H* phase and the octahedral 1*T* phase—results in varied electronic structures. The 2*H* phase typically exhibits semiconducting behavior, whereas the 1*T* and distorted $1T'$ phases display metallic characteristics. For instance, MoS_2 is most stable at room temperature in the 2*H* phase (see Figure 1.3b), but it can also be converted to the 1*T* polymorph via electrochemical etching (Figure 1.3c).[45] Some of the group six TMDs are metastable in the octahedral geometry and distort into the $1T'$ structure.[6, 146] Notably, 2*H* phase edge sites of MoS_2 show a favorable hydrogen adsorption free energy [66, 207], while efforts to maximize the number of these sites or mimic their

activity on the basal plane through sulfur vacancies have enhanced catalytic performance.[95, 93, 8, 70] Metallic polymorphs, with their higher conductivity, have shown greater activity, making them particularly attractive for catalytic processes.[181, 146, 116]

The construction of vdW heterostructures through the strategic assembly of different 2D layers expands the scope of possibilities, enabling the creation of novel quantum materials and devices with custom-designed properties (see Figure 1.4).[48] This methodology, often compared to assembling atomic-scale LEGO blocks, grants researchers the freedom to combine layers without the constraint of crystallographic commensurability, offering an unprecedented degree of freedom in materials design.[1] Unlike LEGO, these materials maintain weak interlayer interactions, allowing them to be reoriented at various angles [15, 14], introducing a versatility that is unparalleled in other material families.

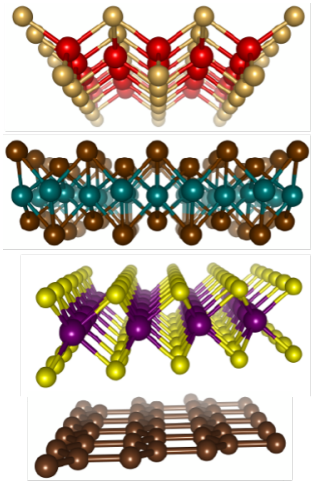

figure 1.4: 2D atomically thin layers can be assembled deterministically into well-defined heterostructures.

Rise of moiré materials and their potential application for electrochemistry

Several methods have been utilized to enhance the electrochemical activity of 2D materials for electrochemical reactions, such as electrostatic gating [178, 106, 60, 177], heteroatom doping [28, 73], lattice straining [95], substrate engineering [94] and heterostructure design [148]. The integration of ”twistronics” into the field of electrochemistry offers groundbreaking opportunities to further exploit the unique properties of moiré materials for advanced electrochemical applications. This innovative approach involves adjusting the twist angle between two layers of 2D materials, such as graphene, to induce moiré patterns or superlattices.[14] These patterns arise from in-plane quasiperiodic modulations in the crystallographic registry when two homologous layers are stacked with a slight interlayer twist. A simple case is illustrated in Figure 1.5a for the simple case of twisted bilayer graphene (tBLG). The wavelength λ_m of these patterns is inversely related to the twist angle

θ, profoundly influencing the material's electronic properties due to the electronic hybridization of the layers (see equation 1.2).

$$\lambda_m = \frac{\sqrt{3}a}{2\sin\left(\frac{\theta}{2}\right)} \tag{1.2}$$

where a is the carbon-carbon bond length in graphene (1.42 Å). The resultant moiré wavelength varies significantly with the twist angle, ranging from approximately 140 nm at a 0.1°twist to about 1.4 nm at 10°.

At specific twist angles, termed "magic angles," the alteration in the band structure of materials like tBLG is particularly significant (see Figure 1.5b,c).[16] For example, at a twist angle of about 1.1°, the band structure shows an extremely flat band near the Fermi level. [81, 71] This flatness leads to a substantial enhancement in the DOS at the Fermi level, facilitating the emergence of exotic physical phenomena such as unconventional superconductivity [16, 109], ferromagnetism [149], and Mott insulator behavior [15] at low temperatures.

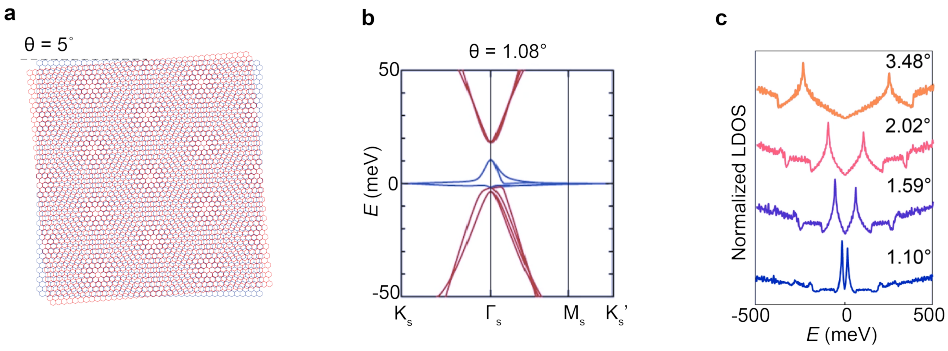

figure 1.5: **a**, Moiré pattern formed when the twist angle between two layers of graphene is 5°. **b**, Electronic band structure of the tBLG when the twist angle is 1.08°. The "flat band" appears near the Fermi level. The energy scale is relative to E_F. Adapted from reference [16]. **c**, Calculated local density of states of twisted bilayer graphene near the magic angle. Enhancement of DOS appears near the Fermi level. Adapted from [81].

The implications of these flat bands for electrochemistry are profound. The increased local DOS near the Fermi level can potentially enhance both inner- and outer-sphere electron transfer reactions. This enhancement could lead to more efficient and selective electrochemical reactions by altering the adsorption potential of reactants, thereby modifying the kinetics of reactions at the interface. Such control over the quantum capacitance and precise alignment of the DOS around the Fermi level with the energy of specified reactants is pivotal in utilizing twisted 2D layers for electrochemical applications.

Moreover, similar band flattening effects have been successfully predicted and realized in TMDs, where a broader range of magic angles leads to the flattening of the conduction band minimum and the valence band maximum [33, 201, 175, 157] and more complex graphene assemblies [14, 127, 83, 150]. This demonstrates the versatility and broad applicability of twistronics across various types of 2D materials. In addition to the intriguing physics associated with these magic angles and their profound impact on electronic properties, their potential in the field of chemistry, particularly electrochemistry, has not been fully realized.

The concept of using twist angle as a means to tune the catalytic activity of 2D materials represents a relatively unexplored yet promising platform. By precisely controlling the twist angle and thereby the electronic properties, it is possible to optimize the band structure of 2D materials to further enhance their performance in interfacial electrochemical reactions. This novel approach could lead to significant advancements in the design and functionality of electrochemical interfaces, paving the way for the development of highly efficient and selective electrochemical systems.

1.4 Scanning electrochemical microscopy for probing electrochemistry on 2D materials

Several advanced techniques have been developed to characterize the properties of 2D materials that are critical for their electrochemical performance. For instance, detailed morphology and crystal orientation of 2D flakes can be readily visualized by high-resolution transmission electron microscopy (HRTEM) combined with electron diffraction.[117, 111] X-ray characterization techniques such as X-ray absorption spectroscopy (XAS) can provide quantitative structural information such as the oxidation state, coordination number, and interatomic distances.[123, 124] Raman spectroscopy is especially powerful in probing the evolution of structure and surface chemistry of 2D materials due to its sensitivity to the layer number, defects, strain, and doping level.[41, 125, 196] However, concerning electrochemical characterization, conventional electroanalytical techniques suffer from their inability to isolate or resolve the contributions of heterogeneities at electrode surfaces. An alternative electrochemical testing platform involves the fabrication of individual 2D flakes into on-chip devices [187, 209], where local measurement may be performed by selectively exposing 2D flakes using lithography. This approach has provided a more direct strategy to spatially resolve electrochemical activity and identify potential active sites. However, the dimensions of on-chip devices in the current stage are limited to micrometer scales, while higher spatial resolution is required to reveal the behaviors of (sub)nanoscale heterogeneities, which may include atomic defects and step edges. The throughput of this technique is also limited by the fact that only a small portion of the 2D material can be probed at a time.

Scanning electrochemical microscopy (SECM) is an electroanalytical scanning probe technique capable of obtaining the electrochemical activity map of a sample with high spatial resolution. This electrochemical characterization technique was introduced by the groups of Bard [5] and Engstrom [40] in 1989. In an SECM experiment, an ultramicroelectrode is scanned over the sample to build an electrochemical map that depends on both the topography and the electrochemical activity of

the substrate. Scanning electrochemical cell microscopy (SECCM) was derived from SECM and introduced by Unwin in 2010. [36, 37] In an SECCM experiment, an electrolyte-filled nanopipette is brought into contact with the sample to form a miniaturized liquid cell and perform localized electrochemical measurements. Both techniques are suitable for carrying out spatially resolved, localized electrochemical characterization with their resolution defined by the probe size. The success of applying scanning electrochemical probe techniques for localized measurement stems from the exceptional spatial resolution realized by miniaturization of the electrochemical probes (i.e., nanoelectrodes or nanopipette) that may attain spatial resolutions ≤ 10m nm.[133, 184] Shrinking the physical size of the probes down to the nanometer range also permits steady-state response readily attained at the nanogap/nanocell. Well-established theories in combination with finite-element simulations for various regimes of measurements have granted SECM/SECCM the capabilities to quantitatively interpret the electrochemical data. [133, 4] We will focus on the working principles, development, and application of SECCM, particularly pertinent to probing 2D materials.

Working principle of SECCM

A double barrel (theta) nanopipette was originally used as the SECCM probe.[36] Two quasi-reference counter electrodes (QRCEs) are placed in each channel filled with an electrolyte solution. The electrochemical cell consists of a meniscus droplet formed at the end of the pipette. A potential (V_1) is applied between the QRCEs to induce an ionic conductance current through the hanging meniscus. The change of ion current upon meniscus contact is detected with high sensitivity, allowing any surface to be probed regardless of its conductivity. The probe moves laterally while the pipette height is adjusted to maintain a constant meniscus shape and resolve topographical features (constant-distance mode). An additional voltage (V_2) between the substrate and QRCE is applied to implement voltammetric and chronoamperometric experiments at the substrate.

A simpler SECCM configuration based on single barrel nanopipettes (Figure 1.6) has been developed for synchronous electrochemical/topographical imaging with high spatial and temporal resolution.[7, 192, 194] The QRCE is kept at a desired voltage relative to the conductive substrate so that a measurable current will flow upon meniscus contact with the substrate, which causes the instrument to halt the vertical approach. Imaging is usually operated in a "hopping mode" where the nanopipette lands onto the substrate at a series of predefined locations. Local voltammetric experiments are carried out to construct an electrochemical activity map. Due to the relatively smaller size of a single-channel nanopipette, direct topographical/electrochemical imaging is achieved with much higher spatial resolution.

Application of SECCM to 2D materials

SECCM has been instrumental in various breakthrough studies involving 2D materials. It has provided insights into the heterogeneous electron HET kinetics at graphene and TMD surfaces, identifying how defects and edge sites enhance or impede electron transfer.[58, 56] For materials like MoS_2 and WS_2, SECCM has been used to distinguish between the catalytic activities of different crystallographic facets and defects at an unprecedented resolution, aiding in the design of better

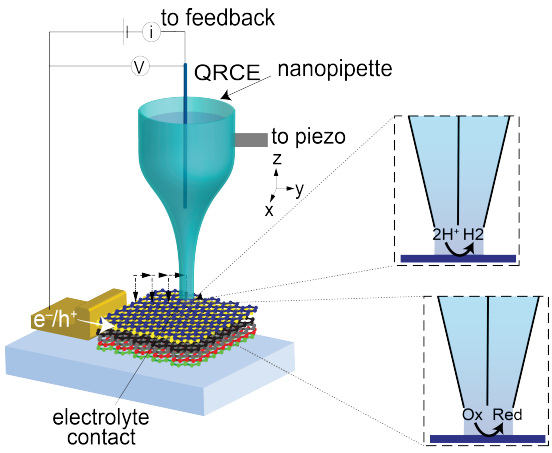

figure 1.6: Working principles of the SECCM. An Ag/AgCl quasi-reference counter electrode (QRCE) is put into the pipette. The pipette approaches the sample via the piezo until a cell is formed between the pipette and the surface of the sample. The two enlarged pipette apertures show how the redox reaction and HER can occur in the droplet.

catalysts. SECCM has also explored the effects of structural phase transitions within TMDs on electrochemical properties, demonstrating how localized strain and material interfaces affect the electrochemical dynamics and catalytic properties.[65] By precisely measuring ionic and electronic transport through 2D layers, SECCM has furthered the development towards advanced batteries and supercapacitors, providing detailed feedback on ion intercalation and storage mechanisms at the nanoscale.[174] A compilation of the studies is listed in Table 1.1.

Table 1.1: Summary of SECCM studies of 2D materials

Technique/Mode	Materials	Reactions	Reference
SECCM, double-barrelled pipette	CVD graphene	$FcTMA^{2+/+}$	[58]
SECCM, double-barrelled pipette	Mechanically exfoliated graphene	$Ru(NH_3)_6^{3+/2+}$	[56]
SECCM, double-barrelled pipette	Mechanically exfoliated graphene	$Ru(NH_3)_6^{3+/2+}$	[56]

Continued on next page

Table 1.1: Summary of SECCM studies of 2D materials (Continued)

Technique/Mode	Materials	Reactions	Reference
SECCM hopping mode	CVD graphene on Cu	$Ru(NH_3)_6^{3+/2+}$	[103]
SECCM, single-channel pipette	twisted bilayer graphene/h-BN	$Ru(NH_3)_6^{3+/2+}$, $Co(phen)_3^{3+/2+}$	[192]
SECCM, single-channel pipette	twisted trilayer graphene/h-BN	$Ru(NH_3)_6^{3+/2+}$, $Co(phen)_3^{3+/2+}$	[194]
All-solid SECCM	Multilayer CVD graphene	$Fe(CN)_6^{3-/4-}$	[76]
SECCM, double-barrelled pipette	Monolayer CVD graphene	H^+ permeation	[9]
SECCM, double-barrelled pipette	Mechanically exfoliated graphene and h-BN	H^+ permeation	[174]
SECCM hopping mode	h-BN on metal substrates	HER	[104]
SECCM, single-channel pipette	Edge-enriched N-doped, P-doped, NP-codoped CVD graphene	HER	[86]
SECCM, single-channel pipette	N-doped r-GO	HER	[75]
SECCM-LEIS	N-doped r-GO	$Fe(CN)_6^{3-/4-}$	[22]
SECCM hopping mode	CVD curved graphene, NSdoped graphene	HER	[31]
SECCM hopping mode	Mechanically exfoliated MoS_2, WS_2, $MoSe_2$, WSe_2	$Ru(NH_3)_6^{3+/2+}$	[13]
SECCM, single-channel pipette	Mechanically exfoliated MoS_2	$Ru(NH_3)_6^{3+/2+}$, $FcMeOH^{+/0}$	[114]
SECCM hopping mode	Cleaved MoS_2 crystal	HER	[8]

Continued on next page

Table 1.1: Summary of SECCM studies of 2D materials (Continued)

Technique/Mode	Materials	Reactions	Reference
SECCM, single-channel pipette	Cleaved MoS_2, WS_2 crystal	HER	[159]
SECCM hopping mode	$1H$ MoS_2, MoS_2/WS_2	HER	[155]
SECCM hopping mode	Mechanically exfoliated p-type WSe_2	$Ru(NH_3)_6^{3+/2+}$, HER	[63]
SECCM hopping mode	Mechanically exfoliated p-type WSe_2	HER, anodization of WSe_2	[65]
SECCM carrier generation-tip collection	Mechanically exfoliated n-type WSe_2	I_2/I–	[64]
SECCM-PL	Mechanically exfoliated WS_2, p-type WSe_2, WSe_2/WS_2	I_2/I–	[43]
SECCM-PL	CVD MoS_2	Oxidation of MoS_2	[153]
SECCM carrier generation-tip collection	Mechanically exfoliated n-type WSe_2	I_2/I–	[162]
SECCM hopping mode	n-type MoS_2/p-type Cu_2O	HER	[203]
SECCM hopping mode	CVD monolayer $2H$-MoS_2 on GC	HER	[108]
SECCM hopping mode	CVD monolayer $2H$-MoS_2 on GC	HER	[107]

Despite its powerful capabilities, SECCM faces challenges such as tip fabrication reproducibility, limited throughput due to slow scanning speeds, and the complexity of interpreting data from highly localized measurements. Future advancements in SECCM technology may include automated, high-throughput systems and integration with other characterization techniques like atomic force microscopy (AFM) or Raman spectroscopy to provide complementary physical and chemical information.

SECCM stands as a critical tool in the arsenal of techniques for studying 2D materials. Its ability to provide localized, high-resolution electrochemical data makes it indispensable for advancing our

understanding of these materials' fundamental properties and pushing forward their technological applications. The continuous evolution of SECCM promises to open new pathways for the precise engineering of 2D materials tailored for specific applications, marking a significant step forward in nanoscale material science. SECCM will excel at probing complex 2D material heterostructures electrochemistry which remains a mostly untapped area of research. We will delve into our studies which utilize SECCM to probe for electrochemical reactions on moiré materials.

1.5 Overview of remaining chapters

In Chapter 2 titled "Tunable Electrochemistry with Moiré Flat Bands and Topological Defects at Twisted Bilayer Graphene," we delve into the profound impact of moiré patterns in twisted bilayer graphene (tBLG) on electrochemical kinetics. The chapter begins by outlining the significance of controlled charge transfer in electrochemical applications and how two-dimensional materials, particularly graphene, offer unique opportunities for modulation of these processes through structural and electronic manipulation.

We explore the concept of "twistronics," which involves adjusting the twist angle between layers of 2D materials to alter their electronic properties drastically. The focus is on how these adjustments affect the electron density states and, consequently, the electrochemical behavior of the material. We describe the experimental setup and methodologies used to fabricate tBLG with controlled twist angles and investigate their electrochemical properties through various analytical techniques.

The chapter presents detailed experimental results demonstrating how the moiré patterns influence electrochemical activity, particularly through the creation of flat bands at "magic angles." These flat bands significantly enhance the local electronic density of states, leading to increased electron transfer rates at specific sites within the moiré pattern, particularly at AA stacking sites.

Furthermore, we discuss the implications of these findings for designing advanced materials for energy conversion applications, such as in fuel cells and batteries. The chapter concludes by highlighting the potential of using moiré engineering and twistronics not just for tuning the electronic properties of graphene but also for other 2D materials, suggesting a broad applicability of these techniques in future material science and engineering challenges.

This exploration not only advances our understanding of the fundamental properties of 2D materials but also opens up new pathways for the design of materials with tailor-made electronic properties for specific electrochemical applications.

In Chapter 3 on "Anomalous Interfacial Electron Transfer Kinetics in Twisted Trilayer Graphene," we explore the nuanced influence of graphene's stacking order and twist angles on electron transfer reactions at electrode-electrolyte interfaces. This investigation delves into how the structural configurations of twisted trilayer graphene (tTG), particularly through moiré patterns formed by varying twist angles, systematically alter the electronic structure, notably the density of states (DOS) and the localization of these states.

The chapter begins by laying a theoretical foundation that connects established electron transfer models with the novel phenomena observed in tTG. Experimental techniques such as Scanning Electrochemical Cell Microscopy (SECCM) and Scanning Tunneling Microscopy (STM) are utilized

to characterize the electrochemical properties and confirm the uniformity and accuracy of the twist angles in graphene layers.

A significant finding discussed is the dramatic variation in electron transfer kinetics depending on whether the graphene layers are stacked naturally (ABA and ABC) or twisted (M-t-B and A-t-A configurations). These variations highlight the critical role of electronic structure, especially the effects of localized and flat electronic bands that emerge at specific 'magic angles' and stacking domains (e.g., AAA and AAB).

The chapter further investigates how these structural modifications influence electron transfer rates, revealing that not just the density but also the spatial distribution of electronic states—down to the atomic level—affects electrochemical reactivity. This insight challenges traditional models of electron transfer by demonstrating that the three-dimensional localization of electronic states across different graphene layers can lead to significant differences in reaction kinetics.

The conclusions drawn from this chapter underscore the potential of using structural engineering of graphene via twistronics to develop electrodes with highly controlled and enhanced electrochemical properties. This approach holds promise for advancing applications in energy conversion and storage technologies, where efficient and tailored electron transfer processes are crucial.

Chapter 4 delves into the innovative realm of moiré superlattices within transition metal dichalcogenides (TMDs), highlighting their potential to revolutionize hydrogen evolution reaction (HER) catalysis. It begins by contextualizing the importance of hydrogen as a sustainable energy source and introduces the basic mechanisms of HER, emphasizing the critical role of catalyst interaction strengths as described by the Sabatier principle and visualized through "volcano plots." The discussion extends to the computational strategies used to predict these interactions and the optimal properties of catalysts for efficient HER.

The chapter proceeds to explore the unique electronic and structural properties conferred by twisting and stacking TMDs, which can significantly influence their catalytic behavior. It explains how the lack of 180° rotational symmetry in TMDs leads to the formation of distinctive moiré patterns, potentially creating ultraflat bands that enhance catalytic sites' density and activity.

Furthermore, the chapter discusses the synthesis of high-quality TMDs tailored for catalytic applications, emphasizing the control over material purity and phase, which are pivotal for achieving desired electrochemical properties. Techniques like SECCM and new methods involving TEM windows are introduced as advanced approaches for probing the catalytic activities of these engineered materials. These methodologies not only allow for precise measurements of reaction kinetics on nano-engineered catalysts but also pose challenges that need systematic exploration to fully harness their potential.

Finally, the chapter concludes by reflecting on the implications of these findings for future research and applications. It calls for continued innovation in synthesis and characterization techniques to unlock the full potential of TMD moiré superlattices in catalysis, suggesting a path forward that could lead to the development of next-generation catalysts for sustainable energy solutions.

Chapter 2

Tunable electrochemistry with moiré flat bands and topological defects at twisted bilayer graphene

Portions of this chapter appear in the following manuscript,
Yun Yu et al. "Tunable angle-dependent electrochemistry at twisted bilayer graphene with moiré flat bands". In: *Nat. Chem.* 14.3 (2022), pp. 267–273

2.1 Introduction

In electrochemical reactions, the flow of charge from electrode to electrolyte drives chemical transformations at the interface, and such interfacial electron transfer reactions underpin key technologies that interconvert electrical and chemical energy.[145, 68, 12, 55] Traditionally, controlled doping or compositional modification of materials has been among the primary knobs for altering the electronic structure of surfaces and tuning their physicochemical properties.[145, 68] Advances in developing atomically thin, so-called two-dimensional (2D) materials, have provided new avenues for controlling interfacial charge transfer and surface reactivity.[32, 74] Unlike bulk 3D materials in which the electrochemically active surface represents only some fraction of the total material, individual layers of these low-dimensional systems are 'all surface'. As a result, their electronic properties are exceptionally manipulable by structural modifications and other external electromagnetic perturbations. Accordingly, in addition to compositional/chemical doping [74, 23], other degrees of freedom emerge for modulating heterogeneous charge transfer at 2D layers including defect engineering [70, 205], strain tuning [176, 95], and field modulation by electrostatic gates [178, 177, 114]. Specifically, defects and edge sites present at 2D surfaces are recognized as reactive hot spots in interfacial charge transfer processes owing to their modified electronic properties [74]. However, the small areal fraction of edge sites[56] constrains the maximized utilization of the whole surface. In addition, it is generally challenging to achieve rational control of atomic defects[205] and an optimized selectivity of the defect-induced enhancement.[113] 2D

atomic layers are also the building blocks for the design of artificial van der Waals (vdW) materials through the deterministic assembly of multiple layers.[48] These vdW heterostructures possess weak interlayer interactions that allow arbitrary azimuthal orientations ('twist angles') between the 2D lattices to be independently controlled, introducing a unique degree of freedom for modulating the electronic properties of 2D materials.[30, 3] Since the discovery of twisted bilayer graphene in 2018, numerous work has discovered an extraordinarily wide and growing collection of exotic physics in twisted 2D layers.[15, 16, 14, 188, 149, 109, 127, 83] For example, twisting a graphene bilayer from a Bernal (AB) stacking configuration to a 'magic angle' (MA) of 1.1° results in the formation of electronic bands with very weak dispersion in momentum space (so-called "flat" bands)[10, 175, 81]. More work has shown that these flat bands produce an array of intertwined correlated electronic phases, including correlated insulating states[15], unconventional superconductivity[16, 188, 109], and orbital magnetism[149, 109]. Analogous architectures comprised of other 2D transition metal compounds have also recently been found to display flat bands and associated correlated electron behavior[175, 33, 201, 157], revealing this concept as a general approach for precisely tailoring the electronic structures of 2D solids. In twisted 2D materials such as these, topological defects are formed at the intersection of soliton walls between different stacking domains.[2] Apart from hosting low-temperature correlated electron physics, these topological defects are conceptually analogous to structural atomic defects that generate localized states that can impact interfacial charge transfer chemistry. While a handful of studies interrogating the effects of interlayer twist on chemical reactivity have been reported[72, 35, 34], these experiments have been restricted to large twist angles ($\geq 7^\circ$) well outside the flat band and 'magic angle' regime. The possibility of exploiting this concept of flat-band topological defects to modulate interfacial charge transfer rates has therefore remained unexplored.

Here, we probe the kinetics of a heterogeneous electron transfer reaction at well-defined twisted bilayer graphene (tBLG) surfaces and show that the kinetics can be strongly tailored by the interlayer moiré twist angle, θ_m, at small angles ($0.22^\circ \leq \theta_m \leq 5^\circ$). In tBLG, the azimuthal misorientation between two homologous layers creates an in-plane quasiperiodic modulation in the crystallographic registry, revealed as a moiré superlattice pattern that displays alternating regions of AA, AB/BA, and saddle-point SP stacking configurations (Figure 2.1a) [190, 81, 79]. The periodicity of the moiré supercells, also known as the moiré wavelength, λ_m, and the size of the mini-Brillouin zone of the moiré superlattice (Figure 2.1b) are both highly dependent on θ_m. Hybridization between adjacent Dirac cones results in an electronic band structure that is strongly modified by the twist angle[15, 10] as shown in Figure 2.1c for MA-tBLG ($\theta_m = 1.1^\circ$). At this θ_m, the bands around 0 eV become remarkably flat, creating a massively enhanced electronic density of states (DOS) concentrated within a narrow energy range of ≈ 20 meV (Figure 2.1d)[15, 10]. At larger θ_m, the bands become more dispersive, with increasing bandwidths and higher energies associated with the locations of the van Hove singularities (vHS) (Figure 2.2). As we now show, these moiré flat band-originated DOS enhancements at vHS play a critical role in governing the heterogeneous electron transfer rate at a graphene–electrolyte interface, making θ_m a descriptor of the interfacial reaction kinetics. We also demonstrate that spatially localized moiré flat bands allow the reaction kinetics to be precisely tuned by the topological defect (AA stacking) density, which is modulated as a function of θ_m.

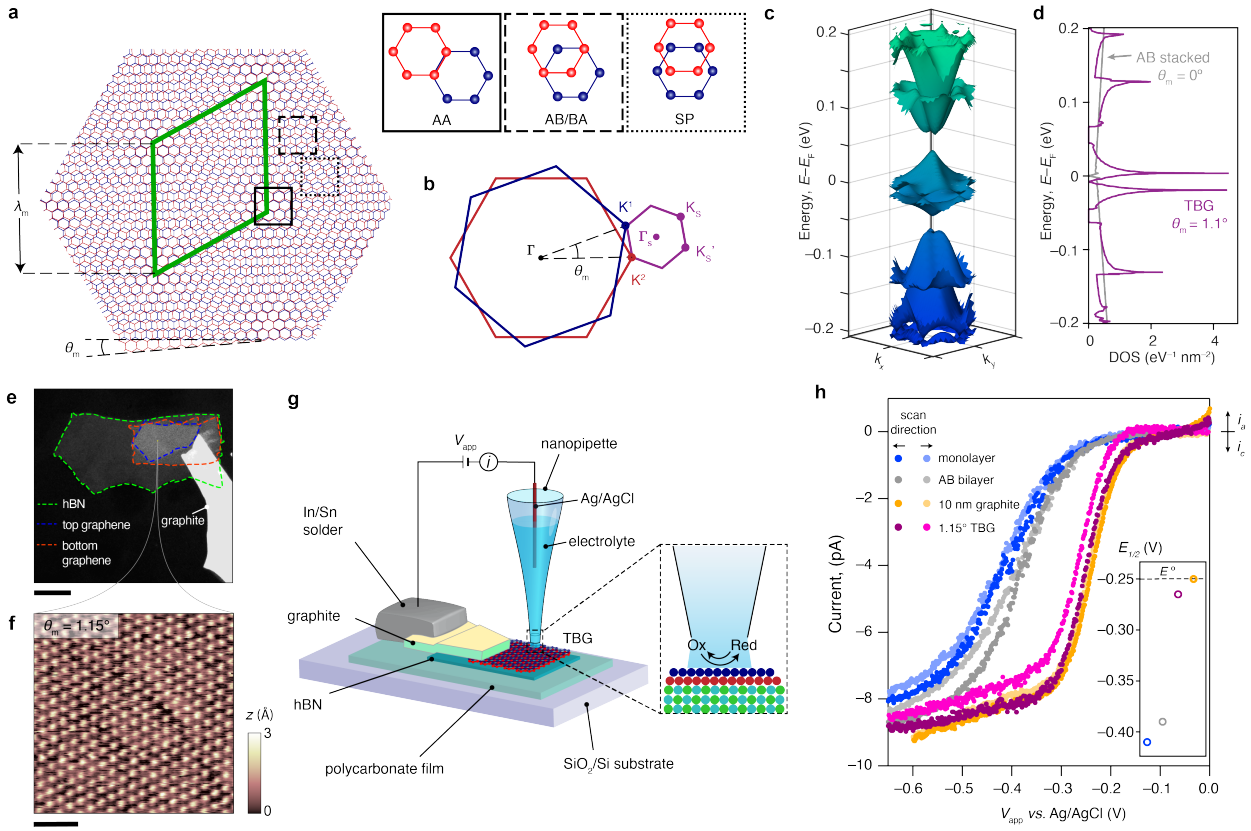

Figure 2.1: **a**, Schematic of a moiré pattern in tBLG and the three stacking configurations (AA, AB/BA, and SP). The moiré wavelength λ_m is determined by the interlayer twist angle θ_m by $\lambda_m = \frac{\sqrt{3}a}{2\sin(\frac{\theta}{2})}$, where $a = 2.46$ Å is the lattice constant of graphene. **b**, The mini-Brillouin zone of a tBLG superlattice generated from the difference between two wavevectors (K1 and K2). **c,d**, Calculated moiré band **c** of $1.1°$ tBLG and corresponding DOS **d**. **e**, Optical image of a tBLG/hBN heterostructure connected to a graphite contact. The dashed lines highlight the two graphene monolayers rotated by θ_m and the underlying hBN flake. Scale bar: 10 µm. **f**, Constant-current STM image of $1.15°$ tBLG acquired from the region marked with a yellow dot in **e**. The image was taken with a 0.1 V bias and a 100 pA set point. Scale bar: 50 nm. **g**, Schematic of local voltammetric measurement at a tBLG surface in an SECCM setup equipped with a single channel nanopipette probe (diameter ≈ 100 nm). The electrochemical bias is applied to the tBLG via the In/Sn and graphite contact with respect to the quasi-reference counter electrode (Ag/AgCl) inside the nanopipette filled with electrolyte. **h**, Representative steady-state voltammograms of 2 mM $Ru(NH_3)_6^{3+}$ in 0.1 M KCl solution obtained at separate, freshly prepared graphene monolayer (blue), Bernal stacked bilayer (grey), 10 nm thick graphite (orange), and $1.15°$ tBLG (purple). Scan rate: 100 mV/s. The inset shows the half-wave potentials of each CV compared to E^0.

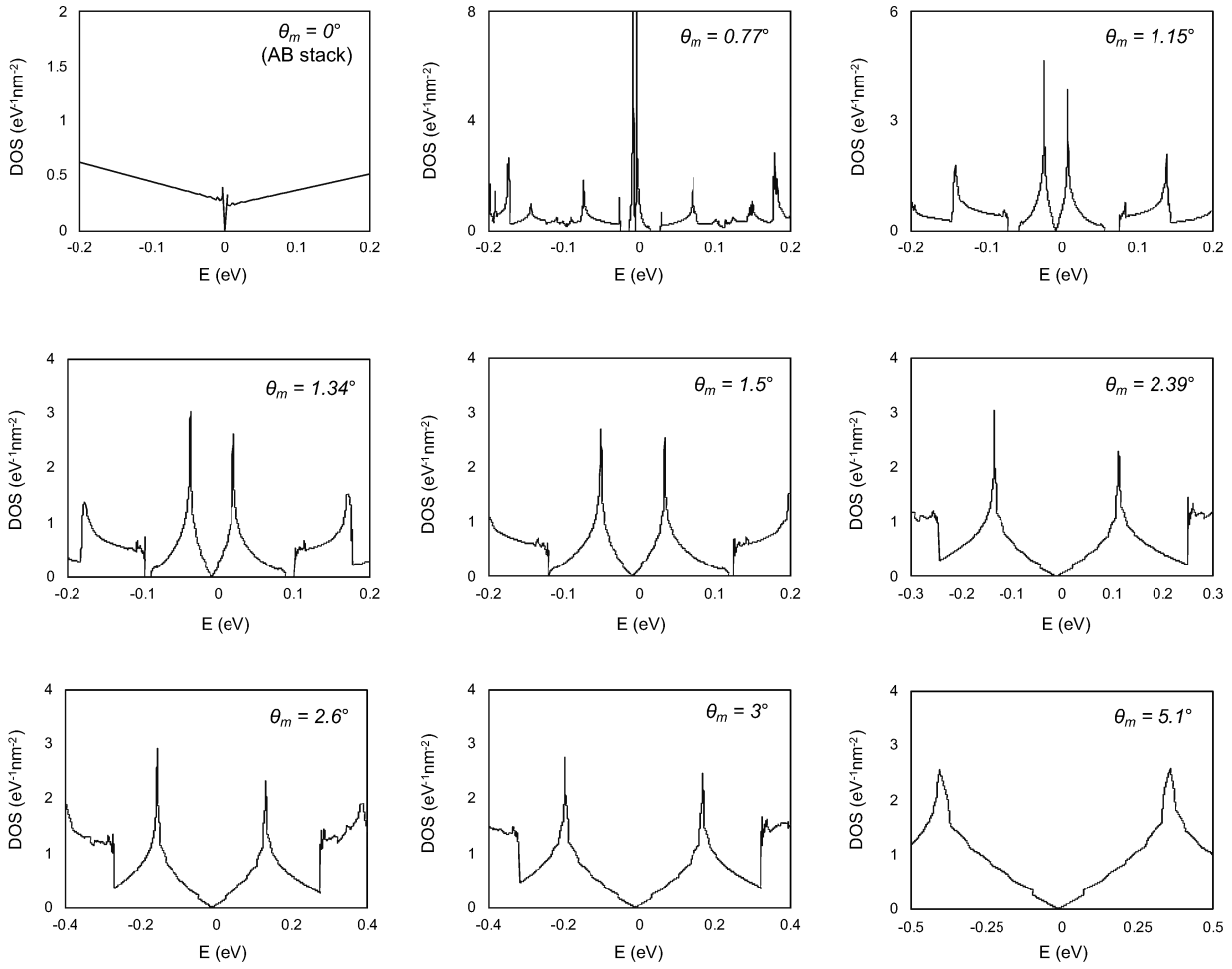

Figure 2.2: Calculated DOS of twisted bilayer graphene with various twist angles.

2.2 Interfacial electrochemistry at magic angle graphene

We fabricated hexagonal boron nitride (hBN)-supported tBLG samples with controlled interlayer twist angles in the range of $0.22° - 5.1°$. Graphene and boron nitride (hBN) flakes were mechanically exfoliated onto SiO_2(285 nm)/Si substrates from their bulk crystals using the well-established "scotch tape" method. Twisted bilayer graphene (tBLG) samples were prepared using the "tear and stack" technique[15] (see Figure 2.3) on a temperature-controlled heating stage equipped with an optical microscope and a micromanipulator. A thin poly(bisphenol-A carbonate) (PC) film attached to a polydimethylsiloxane (PDMS) stamp was used to pick up individual hBN flakes (10–20 nm thick) on the SiO_2/Si substrate. The picked-up hBN was aligned with half of a graphene monolayer, which was then torn along the edge of the hBN. The stage was rotated to a desired moiré twist angle, then the picked-up graphene was placed over the remaining portion of the graphene to form the

tBLG/hBN heterostructure. A thick graphite flake (10–100 nm thick) was then picked up to partially overlap with the graphene to form the immediate electrical contact to the tBLG. The PC film was then delaminated from the PDMS stamp and placed onto a fresh SiO_2/Si chip. Sn/In contacts were made to the graphite contact using the micro-soldering method.[53]

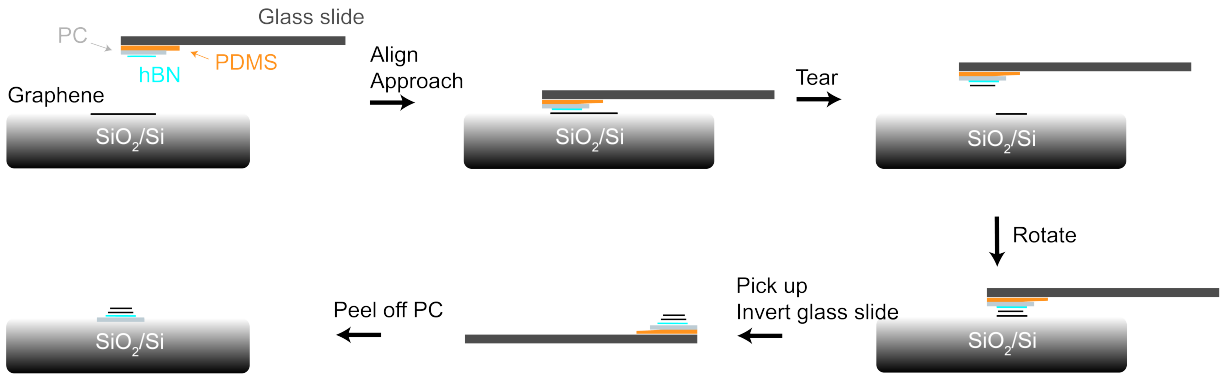

Figure 2.3: A schematic for the "tear and stack" method to make the tBLG samples. Polydimethylsiloxane (PDMS) and polybisphenol A carbonate (PC) are attached to a glass slide. The conjunction of the two polymers is used to pick up hBN. Graphene is first approached by hBN and part of it is torn off from the substrate due to strong vdW interaction between the graphene and the hBN. The remaining piece of graphene is rotated with the substrate. It is picked up again by the torn graphene on the hBN. The whole stack is then inverted and transferred on to a new SiO_2/Si wafer.

Figure 2.1e shows an optical micrograph of a tBLG/hBN sample in contact with a graphite flake as the electrical contact. The pristine surfaces of these graphene moiré superlattice samples are characterized by atomic force microscopy and scanning tunneling microscopy (STM). Figure 2.1f shows a typical constant-current STM image of an exemplary tBLG/hBN sample displaying a clear moiré superlattice pattern as observed previously.[81] For ultraclean tBLG surfaces such as these, the strong electronic localization of flat bands in real space makes it possible to visualize the AA sites as elevated spots, while AB/BA and SP sites appear lower in STM topography.[81, 164] The twist angle ($\theta_m = 1.15 \pm 0.05°$) and uniaxial heterostrain ($\varepsilon = 0.21 \pm 0.12\%$) were obtained from the STM images by fitting the tunneling intensities to a linear combination of bi-variate Gaussians. The mesh was constructed by performing Delaunay triangulation on the Gaussian centers (Figure 2.4), enabling us to measure the three sides of each moiré triangle, λ_1, λ_2, and λ_3. The local twist angles and uniaxial heterostrain are measured through their effects on the moiré patterns as described in reference [190]. A random sampling approach of STM on each sample is used to ensure reasonably uniform local twists throughout a tBLG sample before electrochemical measurements.

Scanning electrochemical cell microscopy (SECCM) with ca. 100 nm spatial resolution allows

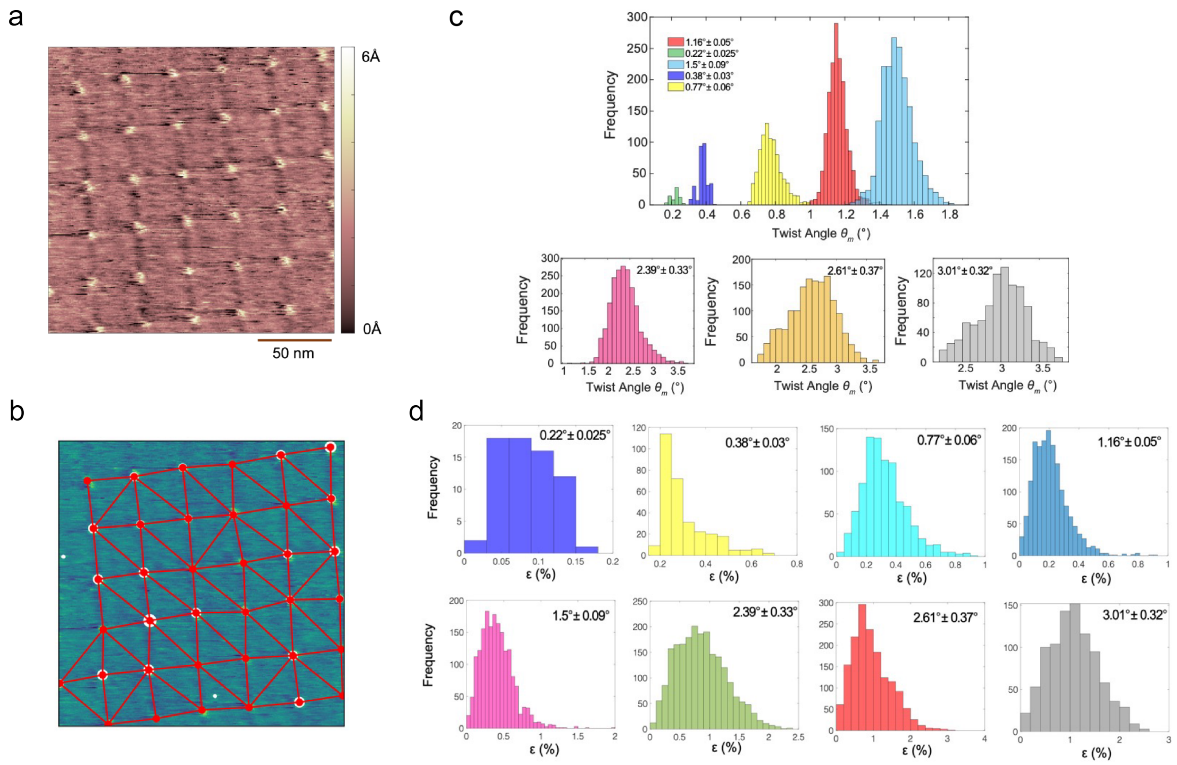

Figure 2.4: **a,b**, A representative STM image of tBLG moiré patterns **a** and the corresponding Delaunay triangulation on the Gaussian centers of AA sites **b**. **c**, Histograms of the local twist angles of each twist bilayer graphene samples. **d**, Histograms of the local heterostrain of each twist bilayer graphene samples.

us to obtain electrochemical measurements exclusively at the basal plane of tBLG (Figure 2.1g). A quartz nanopipette (diameter < 500 nm filled with 2 mM hexaammineruthenium(III) chloride and 100 mM aqueous potassium chloride is used to make meniscus contact with the sample surface, creating a confined electrochemical cell in which localized voltammetry is performed at a series of locations.[56, 113] Typical steady-state voltammograms of $Ru(NH_3)_6^{3+}$ reduction obtained at the basal planes of hBN-supported monolayer graphene, Bernal (AB) stacked bilayer graphene, 10 nm thick graphite (≈ 30 layers), and $1.15°$ tBLG are shown in Figure 2.1h. The anodic shift of the half-wave potential, $E_{1/2}$ (potential at $i = i_\infty/2$, where i_∞ is the diffusion-limited current plateau), with increasing graphene thickness is consistent with the electroreduction of $Ru(NH_3)_6^{3+}$ proceeding more rapidly with augmented DOS from increasing numbers of layers.[56] Remarkably, the $1.15°$ tBLG shows a massive enhancement in reaction kinetics, approaching that of graphite notwithstanding its consisting of only two graphene layers, and exhibiting nearly electrochemically reversible behavior

at the basal plane of this atomically thin electrode.

2.3 Quantum capacitance and interfacial charge transfer model

Interpreting the heterogeneous electron transfer kinetics at these tBLG surfaces mandates the consideration of some physicochemical properties that are integral to electrochemical interfaces of low-dimensional materials. Applying an electric potential (V_{app}) across a solid–solution interface results in the formation of an electrical double layer adjacent to the solid surface, which serves to screen the excess charge. At low-dimensional materials like graphene, the charged ions of the double layer also act cumulatively as an effective electrostatic 'gate' that shifts the Fermi level, E_F, relative to the band edges of the material via dynamic electron/hole doping. Consequently, a significant fraction of V_{app} is consumed as a change of the chemical potential (V_q), while the remainder is confined in the electric double layer (V_{dl}). The contribution from V_q is modeled by introducing an additional capacitance, the so-called quantum capacitance (C_q)[98, 61], in series with the double layer capacitance (C_{dl}) as shown in Figure 2.5a. C_q depends on the electronic structure of the material and is a function of the chemical potential. To evaluate C_q in tBLG, we computed electronic band structures for tBLG over a range of θ_m and determined theoretical C_q values as a function of V_q in each case.

Quantum capacitance (C_q) describes the variation of electrical charges with respect to the chemical potential (V_q). Theoretical C_q values with respect to V_q was calculated based on the following equation[186]:

$$C_{\mathrm{q}} = e^2 \int_{-\infty}^{+\infty} D\left(\epsilon\right) F_{\mathrm{T}}\left(\epsilon - eV_{\mathrm{q}}\right) \mathrm{d}\epsilon \tag{2.1}$$

$$F_{\mathrm{T}}(\epsilon) = (4k_{\mathrm{B}}T)^{-1}\mathrm{sech}^2(\epsilon/2k_{\mathrm{B}}T) \tag{2.2}$$

where $D(\epsilon)$ is the density of states, which we center at the CNP, $F_T(\epsilon)$ is the thermal broadening function and kB is Boltzmann's constant. We assumed T = 300 K for our experimental conditions. The total electric double-layer capacitance is governed by the compact layer capacitance. Hence, we used a constant $C_{dl} = 10\ \mu\mathrm{Fcm}^{-2}$ to simplify the calculation.[179] We solved the self-consistent equations relating V_{app}, V_q, V_{dl}, C_q and C_{dl} using Simpson integration and nonlinear least squares

$$V_{\mathrm{app}} = V_{\mathrm{dl}} + V_{\mathrm{q}} \tag{2.3}$$

$$\frac{V_{\mathrm{dl}}}{V_{\mathrm{q}}} = \frac{C_{\mathrm{q}}}{C_{\mathrm{dl}}} \tag{2.4}$$

to obtain C_q vs. V_q and V_{dl}/V_{app} vs. V_{app} shown in Figure 2.5.

Figure 2.5b shows that higher values of C_q near the charge neutrality point are observed in tBLG for $1^\circ \leq \theta_m \leq 2^\circ$, suggesting that a lower fraction of V_{app} would be consumed on C_q in tBLG around these values of θ_m due to an enhanced DOS near E_F. To directly evaluate the effect of

this θ_m-tunable quantum capacitance on V_{dl}, Figure 2.5c shows how V_{dl}/V_{app} evolves as a function of V_{app} as θ_m is tuned. Higher values of V_{dl}/V_{app} are also observed near charge neutrality for $1° \leq \theta_m \leq 2°$, consistent with the angle dependence of C_q in Figure 2.5b. These results show how moiré-derived flat bands can promote bulk metal-like behavior (increased C_q and higher V_{dl}/V_{app}) in low-dimensional electrodes.

To consider the impact of partitioning V_{app} into V_q and V_{dl} in the electrochemistry of tBLG, we turn to the Gerischer–Marcus[144, 4], or Marcus–Hush–Chidsey (MHC) formalism with the consideration of electrode DOS[62, 87], which describes the heterogeneous electron transfer rate constant, k_{red} (for an electroreduction reaction) in the weak coupling (outer-sphere) limit. In this framework, k_{red} is governed by the distribution and overlap of the electronic energy states, and electron transfer takes place from any occupied state to any unoccupied receiving state with matching energy. Ultimately, k_{red} is the integral of the overlap between the electronic states of the electrode and those of the solution-phase molecule at all energies. When we include considerations brought about by a finite C_q, k_{red} can be modeled as:

$$k_{red} = \nu \int_{-\infty}^{+\infty} D\left(\epsilon - eV_{dl}\right) f\left(\epsilon - eV_{app}\right) W_{Ox}\left(\epsilon\right) d\epsilon \tag{2.5}$$

$$W_{Ox} = \left(4\pi\lambda k_B T\right)^{-1/2} e^{\frac{-\left(\epsilon-\epsilon^0-\lambda\right)^2}{4\lambda k_B T}} \tag{2.6}$$

where ν is the integral pre-factor that considers the strength of the electronic interactions between the reactant and electrode, D_ϵ is the DOS of the electrode, $f(\epsilon)$ is the Fermi-Dirac function, $W_{Ox}(\epsilon)$ is the normalized probability distribution representing the electronic states of the reactant, λ is the reorganization energy, k_B is the Boltzmann constant, and ϵ_0 is the energy corresponding to the standard potential, E_0. In Figure 2.52d, we consider the result of applying a potential bias V_{app} across the solid–electrolyte interface. In this case, e_F is shifted by eV_q relative to the band edge, while eV_{dl} shifts the entire band relative to the energy of the redox molecule. This means that ultimately, the energetic alignment of electron donor-acceptor states is affected by the relative contributions from V_{dl} and V_q, and k_{red} is governed by D_ϵ near e_F. Since $D\epsilon$ is controlled by θ_m, this analysis predicts that k_{red} should display a dependence on θ_m.

2.4 Angle-dependent electrochemical kinetics

Figure 2.6 examines this expectation. tBLG samples with a range of θ_m (exemplary STM images are shown in Figure 2.6a) are used to measure steady-state voltammograms of $Ru(NH_3)_6^{3+}$ reduction. We note that measured values of ε are $< 1\%$ in all our samples and therefore contribute minimally to the perturbation of the interfacial charge transfer kinetics. Based on the established model for voltammetric SECCM experiments [56], we performed finite element simulations of the characteristic voltammetric responses to extract the standard rate constant, k^0, from the experimental cyclic voltammetry (CV) data. This kinetic parameter k^0 denotes the intrinsic electron transfer rate defined in the Butler–Volmer (BV) formulation [4]:

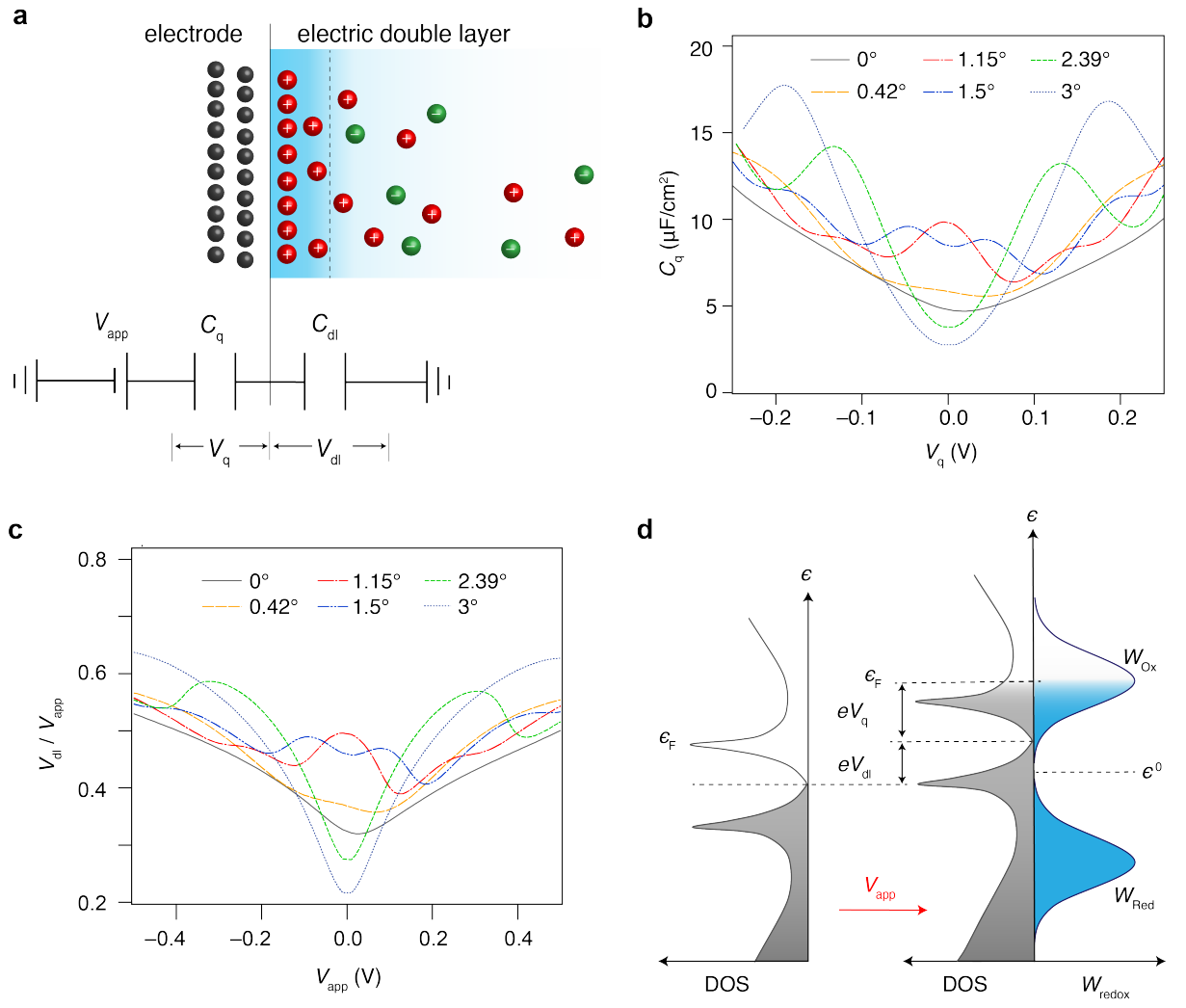

Figure 2.5: **a**, Schematic of the electrode-electrolyte interface represented as the double-layer capacitance (C_{dl}) in series with the chemical quantum capacitance (C_q). **b**, Calculated C_q as a function of the chemical potential (V_q) for various twist angles. **c**, Calculated potential drop on the double layer (V_{dl}) as a function of the applied potential (V_{app}) for various twist angles. V_q and V_{app} are relative to the charge neutrality potential. **d**, Energy diagram depicting that the charge transfer rate is determined by the overlap of electronic states between the electrode (DOS) and the probability distributions representing the solution-phase redox molecules (W_{ox} and W_{red}). Upon applying V_{app}, the Fermi level is shifted by eV_q relative to the band edge, while the band structure is shifted eV_{dl} with respect to the electronic states of the molecule.

$$k_{red}^{BV} = k^o e^{-\alpha \frac{F}{RT}(V_{app} - E^0)} \tag{2.7}$$

where α is the transfer coefficient and F is the Faraday constant.

The finite-element simulation for the steady-state cyclic voltammograms was conducted on COMSOL Multiphysics (version 5.4). The geometry of the pipette was built in a 2-D axisymmetric model as shown in Figure 2.7a. The radii of the droplet were assumed to be the same as the aperture of the pipette. The modules "transport of dilute species" and "electrostatics" were used in conjunction to simulate the mass transport of redox-active molecules in the electrochemical cell defined by the nanopipette and the meniscus.

The steady-state mass transport of redox species was simulated by solving the Nernst–Planck equation:

$$D_i(\frac{\partial^2 c_i}{\partial r^2} + \frac{1}{r}\frac{\partial c_i}{\partial r} + \frac{\partial^2 c_i}{\partial z^2}) = -\frac{z_i F c_i D_i}{RT}(\frac{\partial^2 \phi}{\partial r^2} + \frac{1}{r}\frac{\partial \phi}{\partial r} + \frac{\partial^2 \phi}{\partial z^2});\ 0 < r < r_s, 0 < z < l \tag{2.8}$$

where *r* and z are the coordinates in directions parallel and normal to the sample surface, respectively. r_s and l are the width and the height of the simulation space, respectively. $l = 30$ m is set to ensure that the simulation space is much larger than the aperture size. The meniscus formed between the nanopipette and the sample surface was presented as a cylinder with a height of h. The contact (electroactive) radius, a_s, was set equivalent to the nanopipette radius, a, consistent with previous reports[85, 130]. c_i, z_i, and D_i are the concentration, charge number, and diffusion coefficient of either the oxidized form (c_O) or the reduced form (c_R). ϕ is the electric potential in solution, solved by the Poisson equation:

$$\frac{\partial^2 \phi}{\partial r^2} + \frac{1}{r}\frac{\partial \phi}{\partial r} + \frac{\partial^2 \phi}{\partial z^2} = -\frac{\Sigma_i z_i F c_i}{\varepsilon \varepsilon_0};\ 0 < r < r_s, 0 < z < l \tag{2.9}$$

where $\varepsilon = 80$ is the dielectric constant of the solvent water and ε_0 is the vacuum permittivity. The c_i and z_i in Equation 2.9 include the ions of the supporting electrolyte (0.1 M KCl) in addition to the redox active species c_O and c_R. The rate of heterogeneous electron-transfer reaction is governed by the Butler–Volmer equations:

$$k_{red} = A(E) k^0 e^{-\alpha \frac{F}{RT}(V_{app} - E^0)} \tag{2.10}$$

$$k_{ox} = A(E) k^0 e^{(1-\alpha) \frac{F}{RT}(V_{app} - E^0)} \tag{2.11}$$

where k^0 is the standard rate constant, A(E) is the potential dependent pre-factor to account for the effects of DOS (Figure 2.7d), α is the transfer coefficient, F is the Faraday constant, E^0 is the standard potential, and V_{app} is the applied electrochemical potential. For the simulation of $Ru(NH_3)_6^{3+/2+}$, only the oxidized form (c_O) is initially present in the solution. For $Co(phen)_3^{3+/2+}$, equal concentration of the oxidized form (c_O) and reduced form (c_R) were present. Flux was considered to be zero apart from the contact surface. The general boundary conditions are shown below:

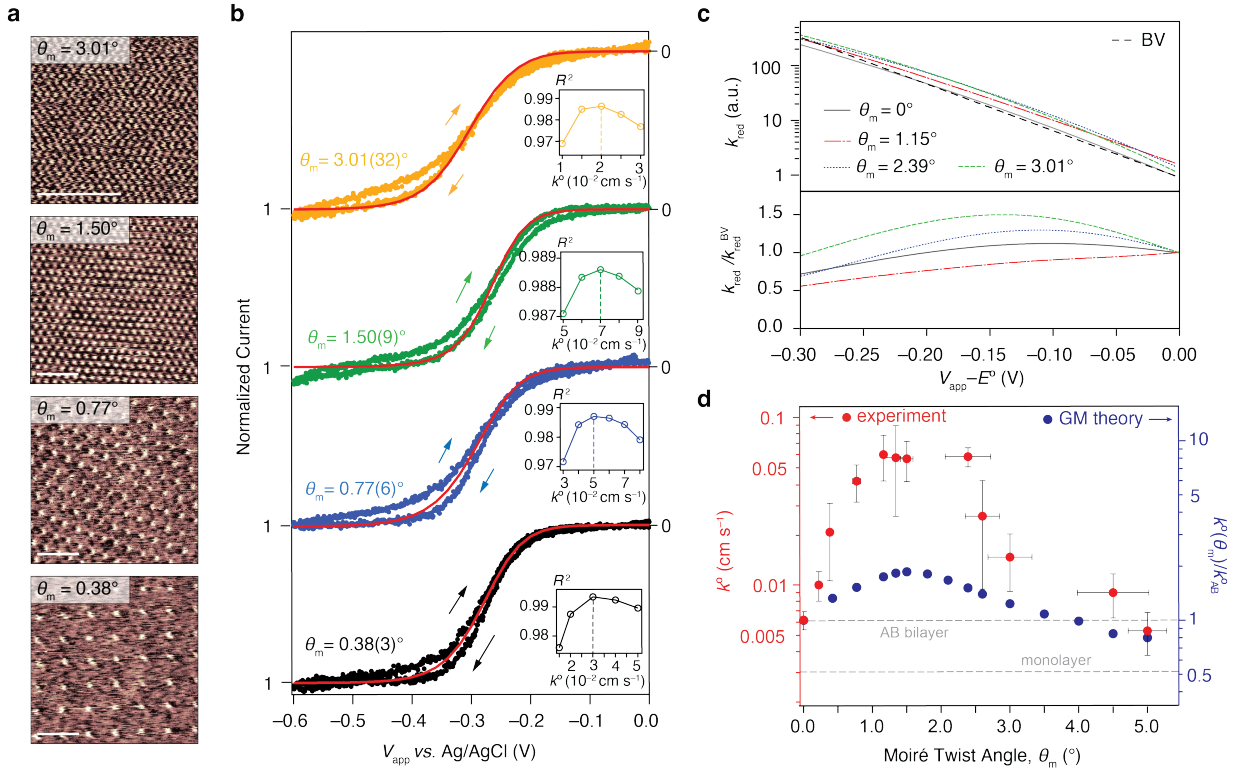

Figure 2.6: **a**, Constant current STM images of tBLG with θ_m = 0.38°, 0.77°, 1.5°, and 3°. Scale bars: 50 nm. **b**, Representative steady-state voltammograms of 2 mM $Ru(NH_3)_6^{3+}$ in 0.1 M KCl solution obtained at tBLG with θ_m = 0.38°, 0.77°, 1.5°, and 3°. The current vs. potential curves were normalized to the mass transfer limiting current. The simulated voltammograms are depicted by solid red lines and the insets display the R^2 values from comparisons of experimental voltammograms to simulated curves using different rate constants. Scan rate =100 mV/s. **c**, Top: k^{red} vs. V^{app} dependence for different θ_m calculated with Gerischer–Marcus (GM) framework compared to the trend of the BV model with a constant pre-factor (for clarity, the BV trace is shown only for the case where $\theta_m = 0°$). Bottom: potential-dependent pre-factor, $A(V^{app}) = k_{red}/k_{red}^{BV}$. **d**, Standard rate constants (k^0) extracted from the experimental voltammograms as a function of twist angle compared to the theoretical values. Each red dot denotes the mean value of the k^0 values obtained from a series of measurements on one sample. The horizontal and vertical error bars represent the standard deviations of θ_m and k^0, respectively. The dashed lines show the experimental k^0 values of monolayer and AB bilayer for comparison.

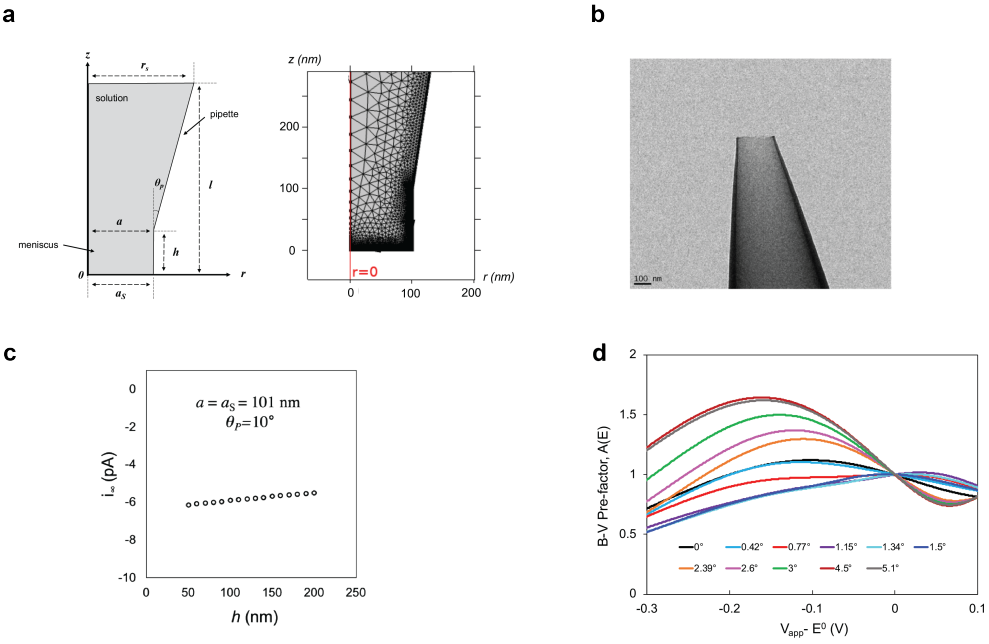

Figure 2.7: **a**, Geometry of the simulation space and an example of mesh used for simulations. **b**, TEM image of a nanopipette with an orifice radius of $a = 101nm$ and taper angle of $\theta_p = 10°$. **c**, Simulated mass transport limiting current (i_∞) as a function of the meniscus height, h. $a = a_S = 101nm$ and $\theta_p = 10°$. **d**, Potential dependent pre-factor, $A(E)$ of various twist angles. $A(E)$ is the ratio of k_{red} calculated using MHC model and k_{red} described in BV model. $A(V_{app} = E_0) = 1$.

$$c_O = c_O^*, c_R = c_R^*;\ 0 < r \leq r_s, z = l; (bulk) \tag{2.12}$$

$$\frac{\partial c_i}{\partial n} = 0;\ 0 < z \leq h, r = a_s;\ h < z < l, r = a + (z - h)\tan(\theta_p);\ (no\ flux) \tag{2.13}$$

$$J_O = -J_R = k_{red}c_O - k_{ox}c_R;\ 0 < r \leq a_s,\ z = 0;\ (sample\ surface) \tag{2.14}$$

where J_O and J_R are the inward flux of the oxidized and reduced form, respectively. c_O^* and c_R^* are the bulk concentrations, $\frac{\partial c_i}{\partial n}$ is the normal derivative of concentration. The potential drop across the Helmholtz layer was implemented by defining the surface charge density, σ, at the sample surface:

$$\sigma = (V_{dl} - \phi)\varepsilon_H\varepsilon_0/d_H;\ 0 < r \leq a_s,\ z = 0; \tag{2.15}$$

where $\varepsilon_H = 6$ and $d_H = 0.5$ nm are the dielectric constants and the thickness of the Helmholtz layer yielding $C_{dl} = 10$ µF/cm^2. V_{dl} is the double-layer potential relative to the charge neutrality point. The steady-state current was evaluated by integrating the total flux of the reactants (J_O) normal to the sample surface:

$$i = 2\pi F \int_0^{a_s} J_O r dr \tag{2.16}$$

For studies of the $Ru(NH_3)_6^{3+/2+}$ couple, D_O and D_R were set to 6.5×10^{-6} cm^2/s [154]. $D_O = D_R = 7.6 \times 10^{-6} cm^2/s$ and $E_0 = 0.15V$ vs Ag/AgCl were used for simulation of $FeMeOH^{0/+}$. $\alpha = 0.5$ was used for all simulations consistent with previous studies on graphene thin films[173]. E^0 was determined from electrochemically reversible voltammograms obtained on a gold or platinum electrode right before the experiments on graphene. For studies of the $Co(phen)_3^{3+/2+}$, $D_O = D_R = 3.7 \times 10^{-6}$ cm^2/s were used for simulation. The pipette taper angle, θ_P, was consistent with pipettes fabricated with the same program reported in a previous study (Figure 2.7b,c).

To extract k^0 from an experimental curve, we generated a series of simulated voltammograms with varying k^0 values and evaluated the residuals of each relative to the experimental curve (based on a sigmoidal fit of the voltammogram), to obtain the coefficient of determination (R-squared, R^2) of each simulated curve. The best fit is determined from the highest R^2 value which is equivalent to the one with the lowest residuals. This procedure is demonstrated in Figure 2.8 where the R^2 values versus different simulated rates are plotted in the bottom right insets of the representative voltammograms.

Figure 2.6c shows that the theoretical k_{red} values that are derived from the Gerischer–Marcus model can be reasonably fit by the BV model with a constant pre-factor for small overpotentials (V_{app}–$E_0 < 0.2V$), but deviations between these two cases become pronounced at larger overpotentials (V_{app}–$E_0 > 0.2V$).[120] Due to the mass-transport limitations in the experiment, we only extracted kinetic information at low overpotentials ($< 0.2V$). Nevertheless, we still apply this small correction for the potential dependence of the apparent rate constant in BV equations.

Figure 2.6d shows the resultant dependence of k^0 on θ_m extracted from the experimental voltammograms (red markers). As implied by the voltammograms in Figure 2.1h, we find the k^0 extracted from tBLG for $1° < \theta_m < 2°$ is strongly enhanced over that of Bernal (AB)-stacked bilayer graphene ($\theta_m = 0°$). By comparison to Bernal bilayer graphene, there is minimal enhancement of k^0 for $\theta_m > 4°$, and for $\theta_m < 1°$, k^0 decreases monotonically with θ_m. We attribute the enhancement of k^0 between $\theta_m = 1°$ and $\theta_m = 2°$ to the elevated DOS arising from the flattened bands that are energetically matched with the formal potential of $Ru(NH_3)_6^{3+/2+}$ (see Figure 2.9).

Our assertion on the criticality of energy matching with the flat bands in dictating the enhanced electron transfer kinetics at tBLG was tested by measurements of the electrochemical kinetics of ferrocenemethanol (FcMeOH) and tris(1,10-phenanthroline)cobalt(II), $Co(phen)_3^{2+}$, which possess formal potentials that are poorly aligned with the charge neutrality point of graphene and, for that matter, the flat bands of small angle ($\theta_m < 2°$) tBLG (see Figure 2.9. For $FcMeOH^{+/0}$, inherently facile kinetics leads to nearly reversible voltammetric responses of FcMeOH[56, 169]

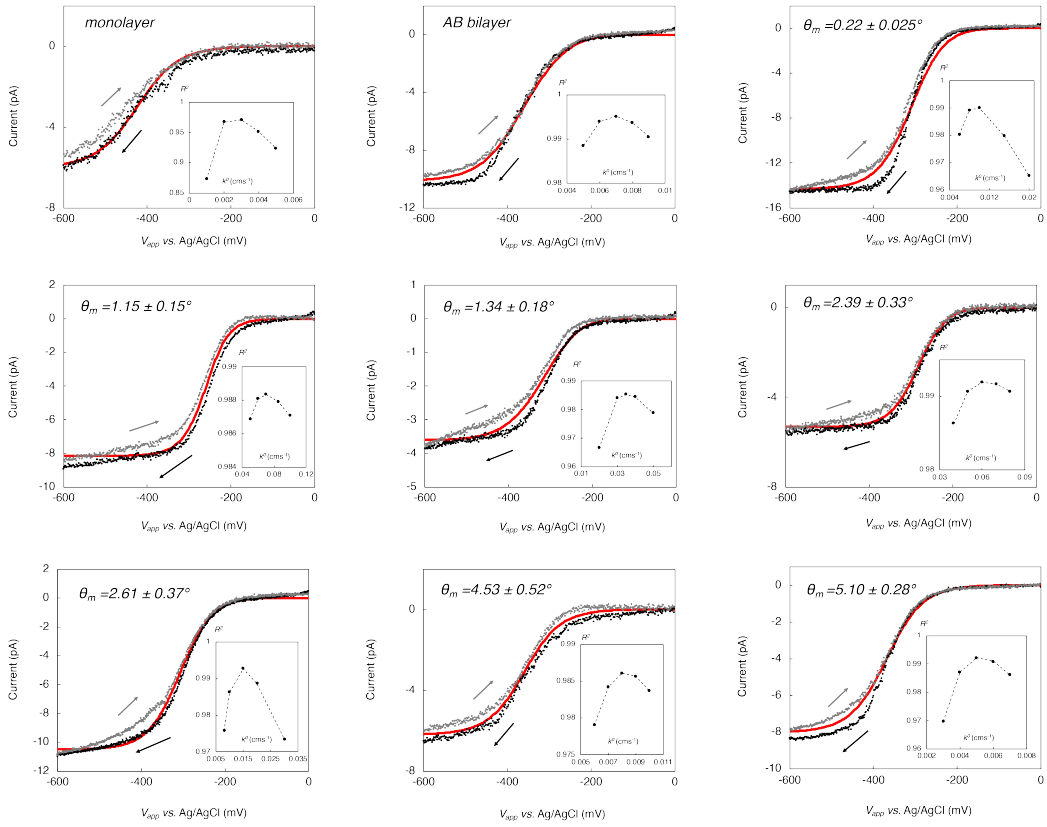

Figure 2.8: Representative steady-state voltammograms of $Ru(NH_3)_6^{3+}$ fit to simulations (red lines) in addition to those shown in Figure 2.6b. The solution contains 2 mM $Ru(NH_3)_6^{3+}$ and 0.1 M KCl. Scan rate: v = 100 mV/s. The black dots and grey dots represent the forward and reverse scans, respectively. The insets show the R^2 values for each simulation. The red lines represent the simulated curve of best fit from the rate constant at maximum R^2.

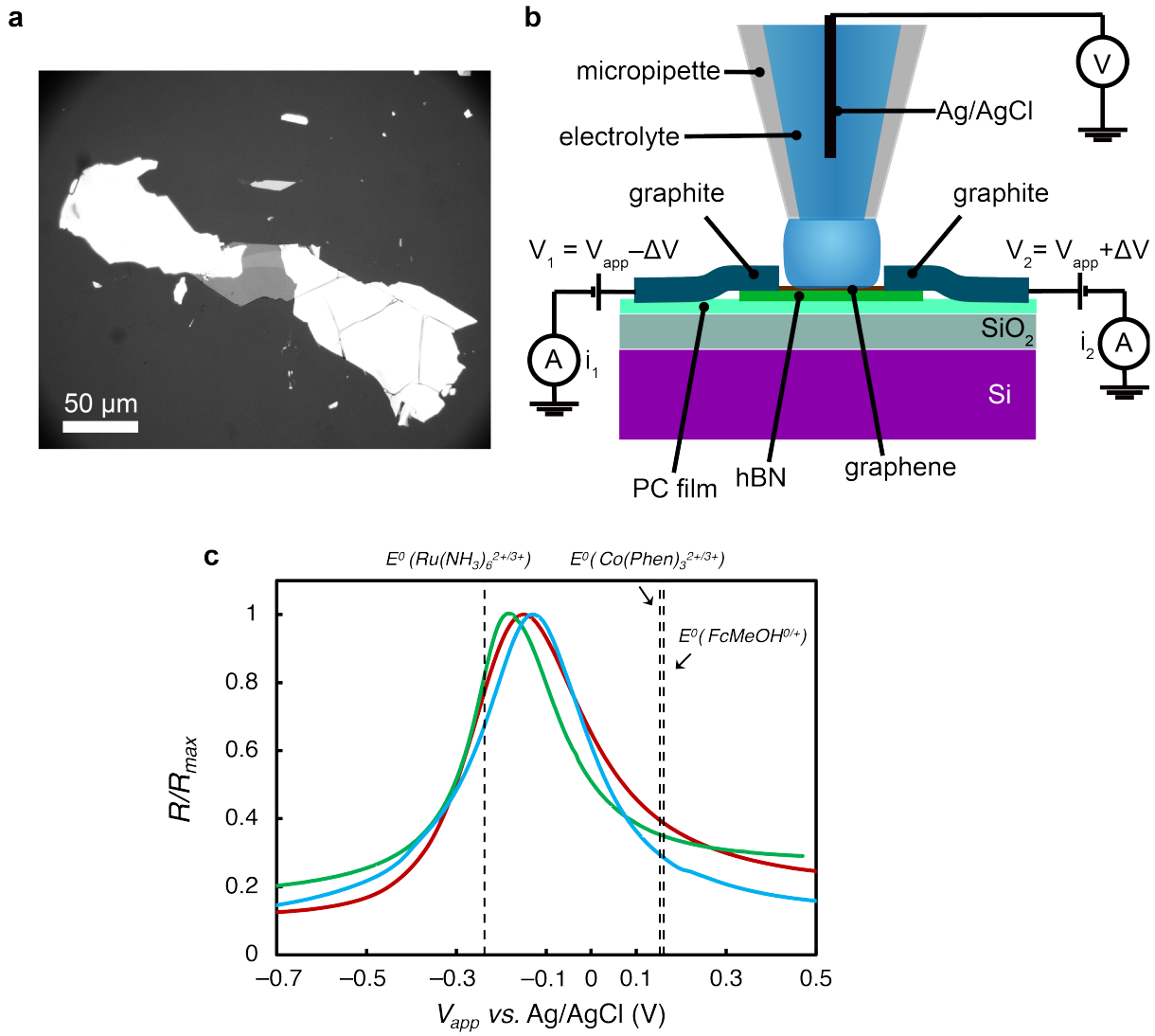

Figure 2.9: **a**, Optical micrograph of a representative device for in situ conductance measurements. **b**, Schematic of conductance measurement. The micropipettes are filled with 2 mM $Ru(NH_3)_6^{3+}$ in 0.1 M KCl aqueous solution. **c**, Flake resistance as a function of the electrochemical bias obtained from 3 different AB-stacked bilayer graphene samples, showing the position of the charge neutrality point (maximum resistance) relative to the E^0 values of the three redox couples interrogated in this study.

at all θ_m (see Figure 2.10a-c). However, the intrinsically slow kinetics of $Co(Phen)_3^{3+/2+}$ allowed us to extract rate constants from the voltammograms obtained at various θ_m (see Figure 2.10d,e), revealing a considerably weaker dependence of k_0 on θ_m compared with that of $Ru(NH_3)_6^{3+/2+}$. These results precisely match our expectation for energetically misaligned donor–acceptor electronic states involving the flat bands; the electrochemical kinetics are not substantially dependent on the electronic flat band.

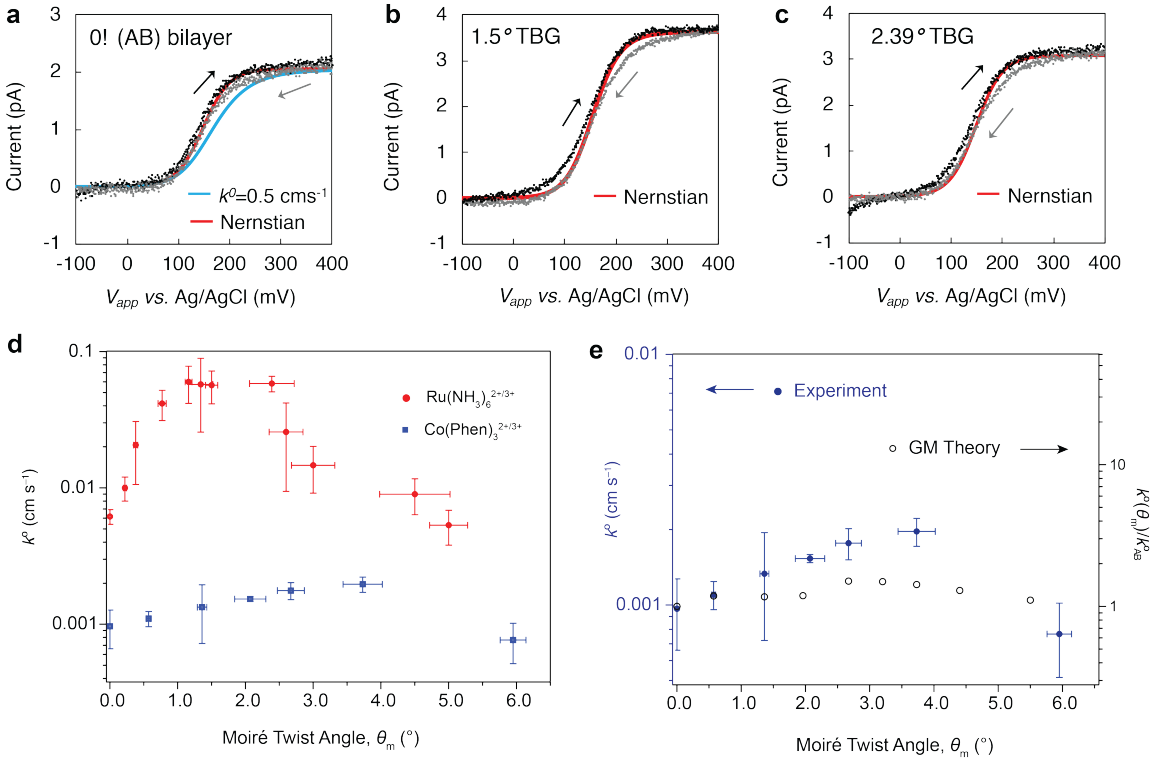

Figure 2.10: **a-c**, Steady-state voltammograms of ferrocenemethanol (FcMeOH) obtained at an AB (0°) stacked bilayer **a**, 1.5° tBLG **b**, and 2.39° tBLG **c** graphene along with simulations of electrochemically reversible voltammograms. The black dots and grey dots represent the forward and reverse scans, respectively. Solution contains 1 mM FcMeOH and 0.1 M KCl. Scan rate v = 100 mV/s.**d**, k^0 extracted from the experimental voltammograms as a function of twist angle for the $Co(Phen)_3^{3+/2+}$ (blue squares) and $Ru(NH_3)_6^{3+/2+}$ (red circles) redox couples. **e**, k^0 for $Co(Phen)_3^{3+/2+}$ extracted from the experimental voltammograms (blue filled circles) as a function of twist angle compared to the values calculated with GM framework (black open circles). The horizontal and vertical error bars represent the standard deviations of θ_m and k^0, respectively.

Figure 2.6d also shows the theoretical dependence of k^0 for $Ru(NH_3)_6^{3+/2+}$ on θ_m (blue markers) calculated from the Gerischer–Marcus model (equations 2.5 and 2.6), manifesting a qualitatively

consistent trend. The maximum enhancement is predicted between $\theta_m = 1.2°$ and $\theta_m = 1.6°$, where the optimal combination of DOS and energy match is achieved after incorporating the effects of quantum capacitance. For $\theta_m > 2°$, the position of vHS becomes further apart from E^0, the magnitude of DOS gradually decays, and k^0 diminishes as a result. While qualitatively descriptive of the experimental data, interestingly, these calculations greatly underestimate the enhancement due to flattened bands in the range $0 < \theta_m < 3°$. To explain this substantial disparity between the Gerischer–Marcus model and our experimental results (the anomalous enhancement of k^0 at low twist angles) as well as the observed monotonic decrease in k^0 with decreasing θ_m for $\theta_m < 3°$, we evaluated the experimental and theoretical real-space variations in k^0 throughout the moiré superlattice.

2.5 Spatial variation in electrokinetics at graphene moiré superlattices

The electronic flat band formed in tBLG moiré superlattices is strongly localized in real space. The local DOS (LDOS) vs. energy at the three stacking regions (AA, AB/BA, and SP) in MA-tBLG ($\theta_m = 1.1°$) is shown in Figure 2.11a. These calculations show how the prominent enhancement of DOS near charge neutrality is strongly localized at AA sites with much lower DOS found at AB/BA or SP stacking sites, in agreement with previous studies.[81, 164] In contrast, Figure 2.11b shows a very weak real-space partitioning of the overall DOS in tBLG with $\theta_m = 3°$ where flat bands are largely absent. Instead, in this regime the LDOS is generally insensitive to the local stacking order. These localization effects can be visualized in the real space LDOS maps shown in Figure 2.11c. Importantly, as a consequence of DOS localization, the interfacial properties of moiré superlattice electrodes are also strongly modulated in real space. Specifically, Figure 2.11c also shows that the potential drop across the double layer (V_{dl}) should be nearly uniform in real space over the moiré structure for $\theta_m = 3°$, whereas V_{dl} would be concentrated at AA sites for $\theta_m = 1.1°$ due to higher LDOS and C_q. Similarly, these calculations predict an enhancement of the electroreduction rate constant, k_{red} for $Ru(NH_3)_6^{3+/2+}$ at AA sites near zero overpotential ($V_{app} = E^0$). The massive LDOS at the matched energy results in significant augmentation of the integral between D_ϵ, $f(\epsilon)$ and $W_{Ox}(\epsilon)$ described in equations 2.5 and 2.6. As the overpotential increases, E_F shifts over the flat band due to the charging of C_q. The enhancement effects from the flat band are diminished at high overpotentials (V_{app}–$E^0 = -0.13V$), leading to a uniform k_{red} distribution across the moiré unit cell. For $\theta_m = 3°$, the calculated maps of k_{red} show minimal spatial variation over all potentials, as expected. Theoretical maps at $\theta_m < 1°$ resemble those of $\theta_m = 1.1°$, showing strong localization of LDOS, V_{dl}, and k^0 at AA sites only scaled by the change of λ_m (see Figure 2.12). To compare these theoretical results to the experiment, we measured the local stacking order-dependent electrokinetics over the moiré superlattice sites.

Even though experimentally, local electron transfer kinetics at isolated AA stacking regions are not directly measurable owing to the spatial resolution limit (ca. 100 nm) in our SECCM setup, we can reliably extract local k^0 values for AA stacking regions (k^0_{AA}) from the ensemble k^0 measured in

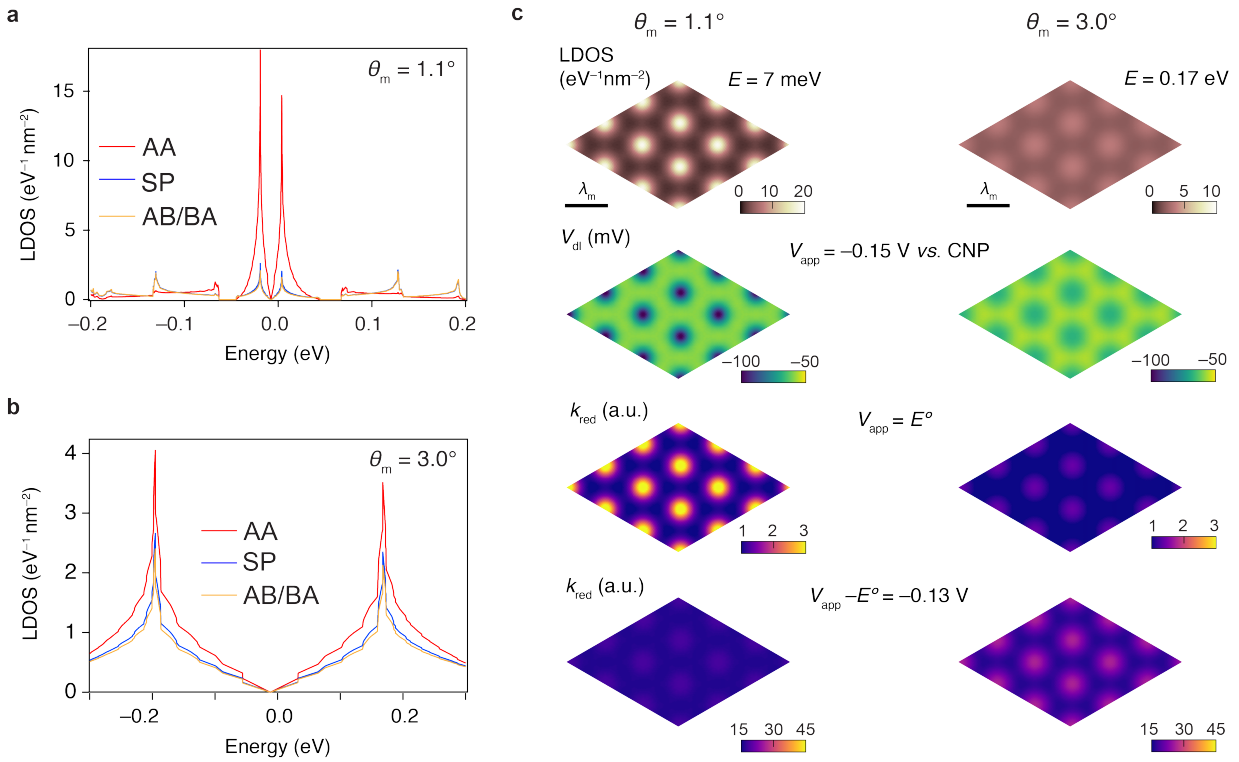

Figure 2.11: **a-c**, Calculated LDOS vs. energy at AA, AB/BA, and SP in tBLG of $\theta_m = 3°$ **a** and 3°**b**. **c**, Calculated real space maps of LDOS, V_{dl}, and k_{red} for tBLG of $\theta_m = 1.1°$ (left column) and 3°(right column). The LDOS are mapped at the energy corresponding to the vHS of each angle. The Vdl values are calculated at $V_{app} = –0.15V$ vs. charge neutrality potential (CNP). Maps of k_{red} are shown at lower overpotential (third row) and higher overpotential (fourth row). The scale bars represent the length of λ_m (12.8 nm for $\theta_m = 1.1°$, and 4.7 nm for $\theta_m = 3°$).

the meniscus covering multiple moiré unit cells. To do so, we take advantage of the independently measurable rate constant for AB stacking (k^0_{AB}), which is determined from standalone measurements at AB bilayers (i.e., $\theta_m = 0°$) (Figure 2.1h and Figure 2.6d). Considering the ensemble current as arising from the sum of local currents weighted by the area fraction, A, of each domain (AA, AB/BA and SP), the ensemble rate constant, k^0, may be written as:

$$k^0 = A_{AA}k^0_{AA} + A_{AB}k^0_{AB} + A_{SP}k^0_{SP} \tag{2.17}$$

Where k^0_{AA}, k^0_{AB}, and k^0_{SP} denote the respective local rate constants at AA, AB/BA, and SP domains. To simplify the analysis, we assume $k^0_{AB} \approx k^0_{SP}$ —a reasonable approximation given the very similar LDOS calculated (Figure 2.11a–c) and measured by STM (Figure 2.6a)[81]. These considerations reduce equation 2.17 to,

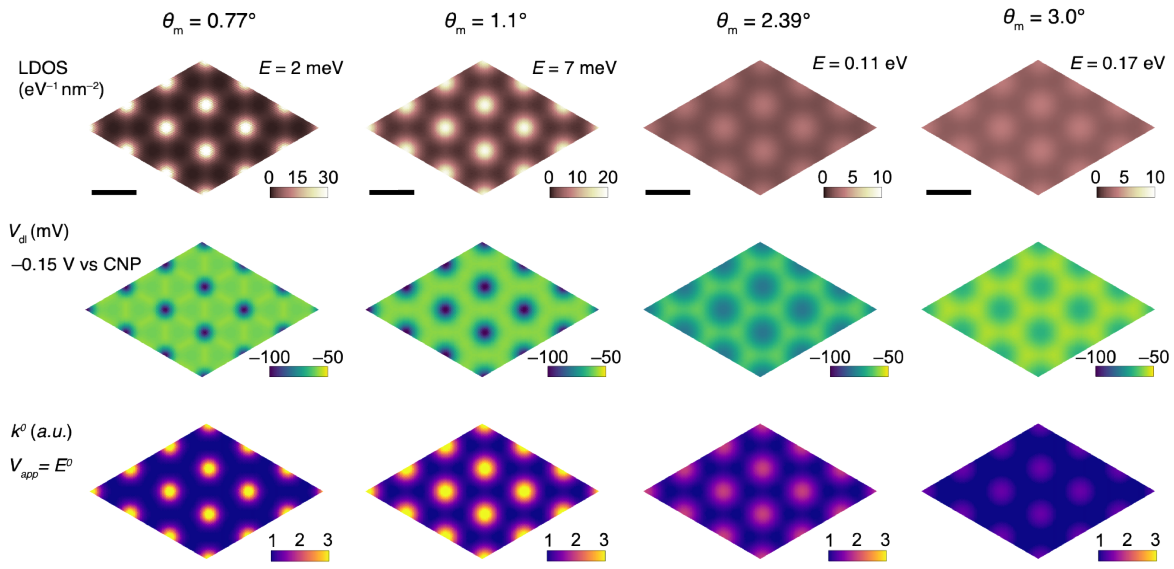

Figure 2.12: Calculated real space maps of LDOS, V_{dl}, and k_{red} in tBLG with $\theta_m = 0.77°$, $1.1°$, $2.39°$ and $3°$. The DOS and activity are strongly localized at AA regions for $\theta_m < 2°$ in comparison with tBLG with $\theta_m > 2°$.

$$k^0 = A_{AA}k^0_{AA} + (1 - A_{AA})k^0_{AB} \tag{2.18}$$

To determine area fraction values for equation 2.18, we have previously employed four-dimensional scanning transmission electron microscopy, 4D-STEM[79], to reveal that AAA increases monotonically with θ_m until θ_m reaches $\approx 2°$ due to a spontaneous lattice reconstruction process involving localized rotations[190, 79, 195], after which area fractions approach values expected from a rigid moiré. From these established measurements we know AAA, AAB/BA, and ASP as a function of θ_m. These insights allow us to extract experimental values for kºAA as a function of θ_m in Figure 2.13a. Interestingly, we find that kºAA is insensitive to twist angle for $\theta_m < 1.5°$, showing a fairly constant value around 0.2 cm/s. This trend is remarkably consistent with our previous structural measurements[79] that unveiled the geometric effects of lattice reconstruction. This effect is depicted in Figure 2.13b. At $\theta_m < 1.5°$, positive local rotations centered on the AA stacking sites, where flat band wave functions are predominantly localized (Figure 2.13c), cause the atomic geometry in these regions to be nearly insensitive to the global θ_m, 'pinning' the local rotation to $\approx 1.2°$. On the other hand, localized negative rotation in AB/BA regions produces a local atomic geometry that closely matches Bernal stacked bilayer graphene[79]. Thus, our measurements show that for $\theta_m < 1.5°$, the primary effect that drives the θ_m-dependent ensemble k^0 shown in Figure 2.6d is the change in the moiré wavelength (and attendant AA stacking area fraction), whereas

the local electrochemical activities remain effectively constant (plateau in k^0_{AA} for $\theta_m < 1.5°$ in Figure 2.13a). This convergence of local electrochemical behavior is also manifest in plots of k^0_{AA} as a function of the net local AA rotation after lattice relaxation, θ_T^{AA} (inset of Figure 2.17a). At larger θ_m, the enhancement from flat bands and the atomic reconstruction process both diminish, causing k^0_{AA} to eventually become similar to k^0_{AB} for $\theta_m \geq 4$. As a result, k^0_{AA} exhibits a monotonic downward trend with the increase of the local and global moiré angle at AA sites (inset of Figure 2.13a).

While this local θ_m dependence is qualitatively supported by the theoretical k^0_{AA}, k^0_{AB}, and k^0_{SP} values that are plotted in parallel with the experimental values in Figure 2.13, we find a large discrepancy between the experimental k^0_{AA} values and those calculated using the Gerischer–Marcus model alone. Crucially, Figure 2.13 reveals that the discrepancy between theory and experiment in overall k^0 (Figure 2.6d) originates from this underestimation in k^0_{AA} specifically (Figure 2.13a). Further, this large, anomalous enhancement of the electron transfer rate (over that predicted from the Gerischer–Marcus theory) near and below the MA, which originates from the topological defects of the moiré with AA-localized flat bands, cannot be explained merely by the commensurability of energetic overlap between donor–acceptor states, nor by the enhanced DOS (Figure 2.2d). Instead, this observation may be explained by modifications to the electronic coupling strength (ν in equation 2.5) with θ_m. At present, our theoretical analyses in Figure 2.6d and Figure 2.13 do not consider a dependence of ν on θ_m via changing local stacking configurations and band flatness. However, it is reasonable to expect that ν should be strongly impacted by the localized flat band structure and this should then make a considerable contribution to the electron transfer rate according to equation 2.5. Indeed, the electronic transmission coefficient is increased at graphene zigzag edges in the non-adiabatic regime owing to localized electronic edge states at E_F.[132] By analogy, the highly localized flat bands in small angle tBLG (Figure 2.11c) would result in significantly larger real-space overlap of the electronic wave functions of the tBLG and solution-phase redox complexes, inducing an additional augmentation of the measured rate. The effects of moiré reconstruction and pinning of the local rotation field near the MA ($\approx 1.2°$)[79] would then keep this enhancement constant for $\theta_m < 2°$, precisely as observed in Figure 2.13a. Additionally, it is conceivable that greater local potentials (higher local V_{dl} in Figure 2.11c) at AA sites could also modify the structure of the electric double layer and/or create a shorter electron tunneling distance between the electrode and redox species, through electroosmosis and/or stronger electrostatic interactions with the charged complexes, and thus a transition to the adiabatic regime.[4]

2.6 Conclusion

The intriguing interfacial electron transfer behavior of tBLG demonstrated here suggests that in addition to low-temperature correlated electronic phases, moiré-derived flat bands in vdW architectures present a highly tunable material platform to systematically manipulate and fundamentally probe interfacial charge transfer and (electro)chemical transformations at well-defined surfaces. In lieu of introducing foreign dopants or structural defects that can be difficult to control, we have demonstrated the feasibility of activating the pristine graphene basal plane surface with topological defects that

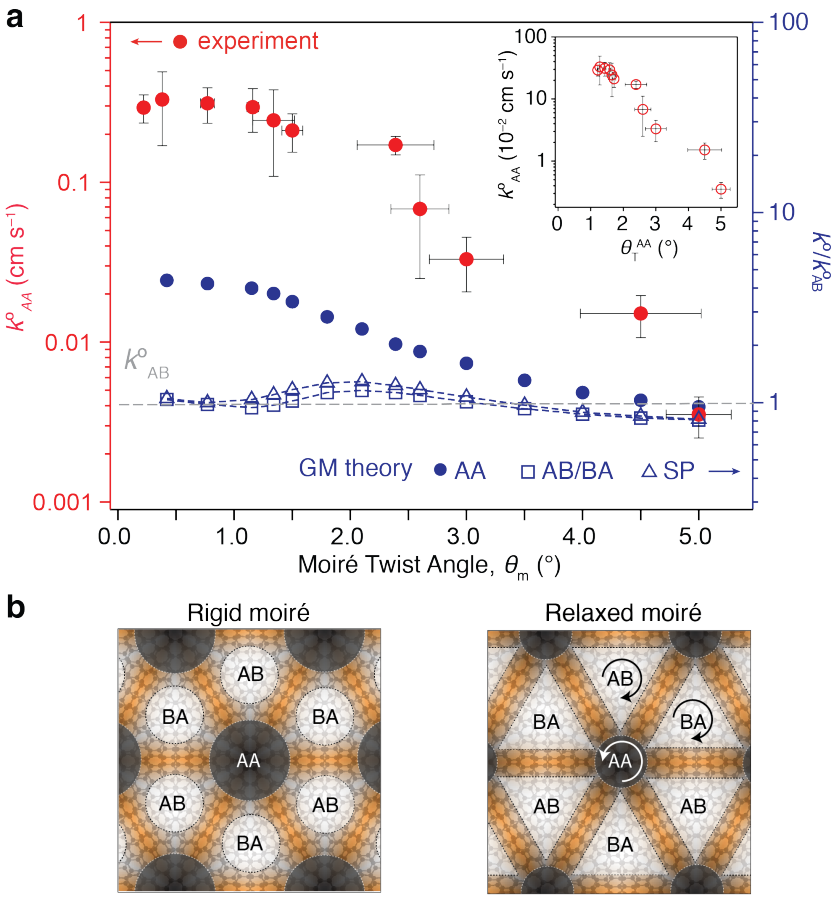

Figure 2.13: **a**, Experimental local k^0 at AA sites as a function of θ_m extracted from Figure 2.6d compared to the theoretically predicted (Gerischer–Marcus, GM) values of k^0 at AA, AB/BA, and SP stacking regions. The horizontal and vertical error bars represent the standard deviations of θ_m and k^0_{AA}, respectively. The dashed line shows the experimental k^0 values of AB bilayer represented as k^0_{AB}. The inset shows the local k^0 at AA sites as a function of the local net rotation angle of AA sites due to lattice relaxation, θ_T^{AA}. b, Schematic illustration of the lattice relaxation (atomic reconstruction) process, which modifies the area fraction and local net interlayer rotation angle of the various stacking configurations through localized rotational deformations of the moiré superlattice.

originate from the structural symmetry breaking in twisted bilayers.[2] The AA stacked sites in which the flat bands are strongly localized bear an analogy to the structural defects that have been shown to produce enhanced DOS and promote interfacial charge transfer.[74, 205, 56, 132] However, here we show, simply by the precise control of the interlayer twist angle, flat bands that are intrinsically localized to nanoscale domains in real space, may be exploited to control the rate constant for an outer-sphere charge transfer reaction. We anticipate that flat-band engineering with moiré architectures is a general strategy to tune the chemical reactivity of a variety of 2D surfaces. The wide array of 2D transition metal compounds and the generality of the moiré superlattice approach for engineering flat bands in these materials as well[175] foreshadows this 'twistronic' topological defect and moiré flatband approach as a versatile new avenue for also tailoring (electro)catalytic (inner-sphere) reactions where interfacial reactivity is governed by the structure and dispersion of the electronic bands of the electrode near E_F, which determine the adsorption energetics of intermediates[68].

Chapter 3

Anomalous interfacial electron transfer kinetics in twisted trilayer graphene

Portions of this chapter appear in the following manuscript,
Kaidi Zhang et al. "Anomalous Interfacial Electron-Transfer Kinetics in Twisted Trilayer Graphene Caused by Layer-Specific Localization". In: *ACS Cent. Sci.* (2023)

3.1 Introduction

Electron-transfer (ET) reactions at electrode–electrolyte interfaces are fundamental to electrochemical energy conversion.[145, 121, 68] The collective of microscopic theories and models for interfacial ET, inclucing the Marcus–Gerischer formalism,[144, 88, 4, 143, 50, 52] the so-called Marcus–Hush–Chidsey (MHC) model,[62, 193] and the density of states (DOS)-incorporated MHC (MHC–DOS) model,[87] highlight the importance of the electronic structure of an electrode on heterogeneous electrochemical rates. These frameworks motivate the discovery of new approaches to manipulate the band structure of electrodes as a means of controlling the performance limits of energy conversion and storage devices. Even though the electrode DOS was originally treated as invariant with energy/overpotential and delocalized, recent work has shown that the energy dependence of the DOS can be an important factor in electrochemical reactions.[87] Further, the effect of local DOS beyond the global electrode DOS has been identified as critical in understanding interfacial ET kinetics. On semiconductor or semimetallic electrodes, local electronic structure differences have been shown to affect ET kinetics,[131] and atomic defects at electrode surfaces provide a striking, albeit challenging to control, an example of the pronounced effect of local structural/electronic modifications on interfacial reactivity. Atomic vacancies[95], kinks, and step edges[70, 57, 169] are typically associated with massively enhanced interfacial reactivity compared to atomically pristine surfaces. The effect of these defects is typically explained in the context of providing increased DOS at energies that are desirable for charge transfer or formation of a surface-bound catalytic intermediate (such as mid-gap states in a semiconducting material.[70, 95]) However, the dangling bonds at such sites would invariably introduce a strong spatial localization of these large electronic

DOS. For this reason, beyond the augmented DOS magnitude, we might consider that localization may play a key role in facilitating interfacial ET to the necessarily localized electronic states on the solution-phase molecule/complex/ion. Yet, a systematic experimental examination of the effects of electronic localization on heterogeneous interfacial charge transfer has been intractable owing to the considerable synthetic challenge of constructing pristine electrode materials that would allow a deterministic modulation of this property separate from the overall DOS.

Azimuthal misalignment of atomically thin layers produces moiré superlattices and alters the electronic band structure, in a manner that is systematically dependent on the interlayer twist angle.[84, 91] The formation of flat electronic bands, particularly at a series of 'magic' moiré angles leads to a diversity of correlated electron physics.[15, 59, 19, 3] Notably, these flat bands imply a large DOS that is highly localized in real space[81]. Small-angle twisted bilayer graphene (tBLG) exhibits a recently discovered angle-dependent electrochemical behavior[192], where outer-sphere ET kinetics can be tuned nearly tenfold simply by varying moiré twist angle, θ_m, between 0° and 2°.

The stacking order of graphene in multilayers strongly alters the resulting electronic properties of the system.[90, 89, 182, 210, 97, 197, 128, 127, 59, 42] As shown in Figure 3.1, whereas Bernal (ABA-stacked) trilayer graphene displays dispersive bands, rhombohedral (ABC) graphene possesses a non-dispersive, or 'flat', electronic band close to the Fermi level, which is responsible for the emergence of correlated electron phenomena at low temperatures.[206, 20]

More pronounced flat bands are produced in twisted trilayer graphene (tTG) structures. Rotationally misaligned (by a moiré 'twist' angle θ_m) monolayer and Bernal stacked bilayer forms a 'monolayer-twist-bilayer' (M-*t*-B) heterostructure (Figure 3.2a).[183, 100] Systematically alternating the angle between adjacent graphene layers such that the top layer is perfectly aligned with the bottom layer results in an 'A-*t*-A' heterostructure (Figure 3.2b)[127, 59, 42] that possesses extremely flat bands at a magic angle around $1.5°$ (Figure 3.1). These flattened electronic bands, which manifest as large DOS that are localized on AAB and AAA sites in M-*t*-B and A-*t*-A tTG, respectively (Figure 3.2c,d), now introduce distinctive possibilities for systematically probing the dependence of interfacial ET on electronic structure generally and in particular, the effects of electronic localization. For example, even within the tTG family, larger DOS are found in A-*t*-A as compared to M-*t*-B near their respective magic angles (Figure 3.2c,d), properties that naively might be expected to correlate with interfacial ET rates, based on MHC theory.

3.2 Fabrication and electrochemistry of tTG

Scanning electrochemical cell microscopy (SECCM)[169] measurements were carried out on non-twisted (ABA, ABC) and twisted trilayer graphene samples that were fabricated into devices as discussed in Chapter 2.[192] As shown in Figure 3.5a, naturally occurring ABA and ABC trilayers were mechanically exfoliated from bulk graphite and identified using optical microscopy together with confocal Raman spectroscopy.[110, 26] M-*t*-B and A-*t*-A tTG samples were prepared by the 'cut-and-stack' approach, resulting in samples possessing uniform θ_m around the 'magic angles' of about 1.34° for an M-*t*-B device and 1.53° for an A-*t*-A device.

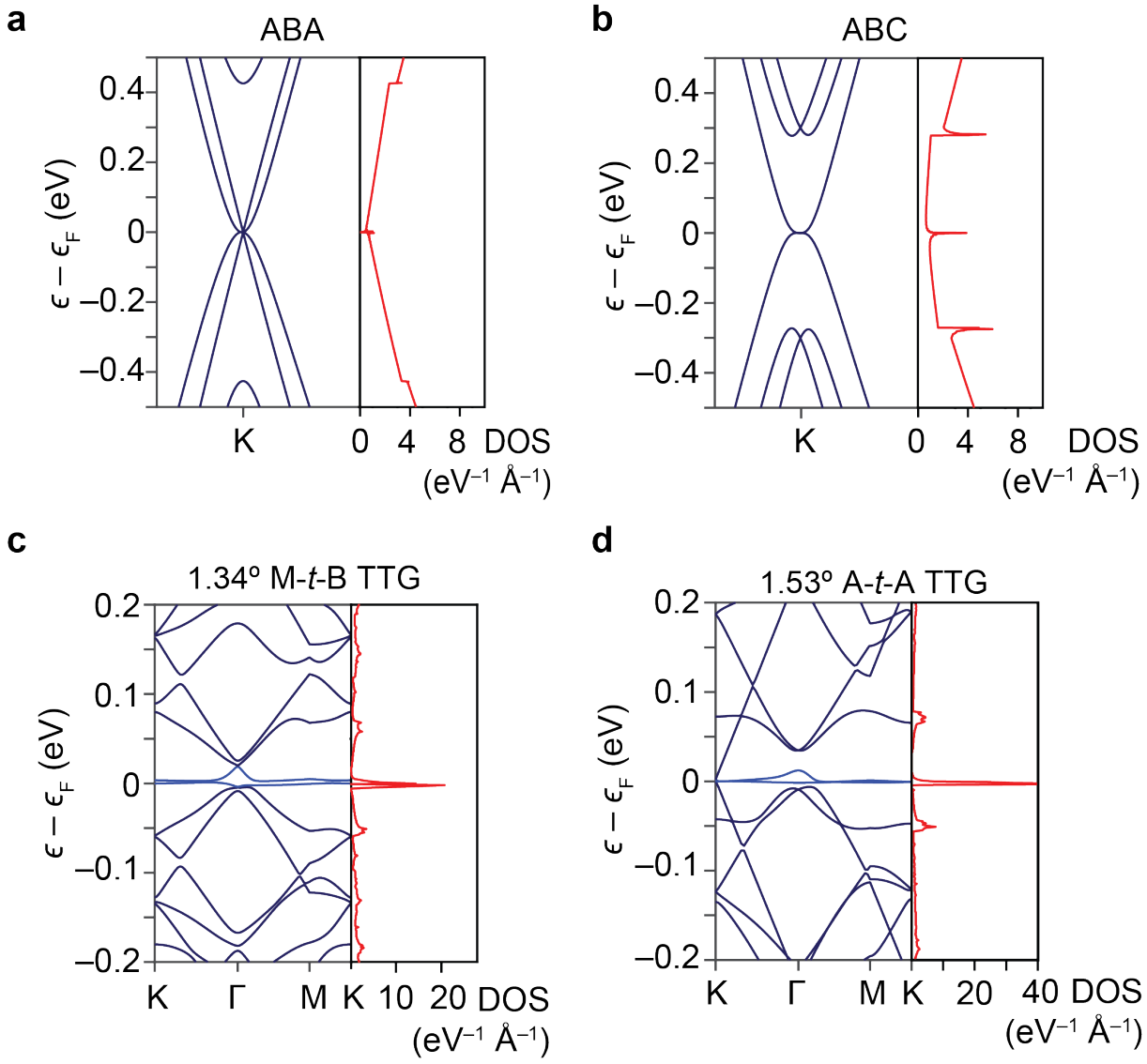

Figure 3.1: **a–d**, Computed electronic band structures (see Methods) for ABA **a**, ABC **b**, 1.34° M-*t*-B **c**, and 1.53° A-*t*-A **d**.

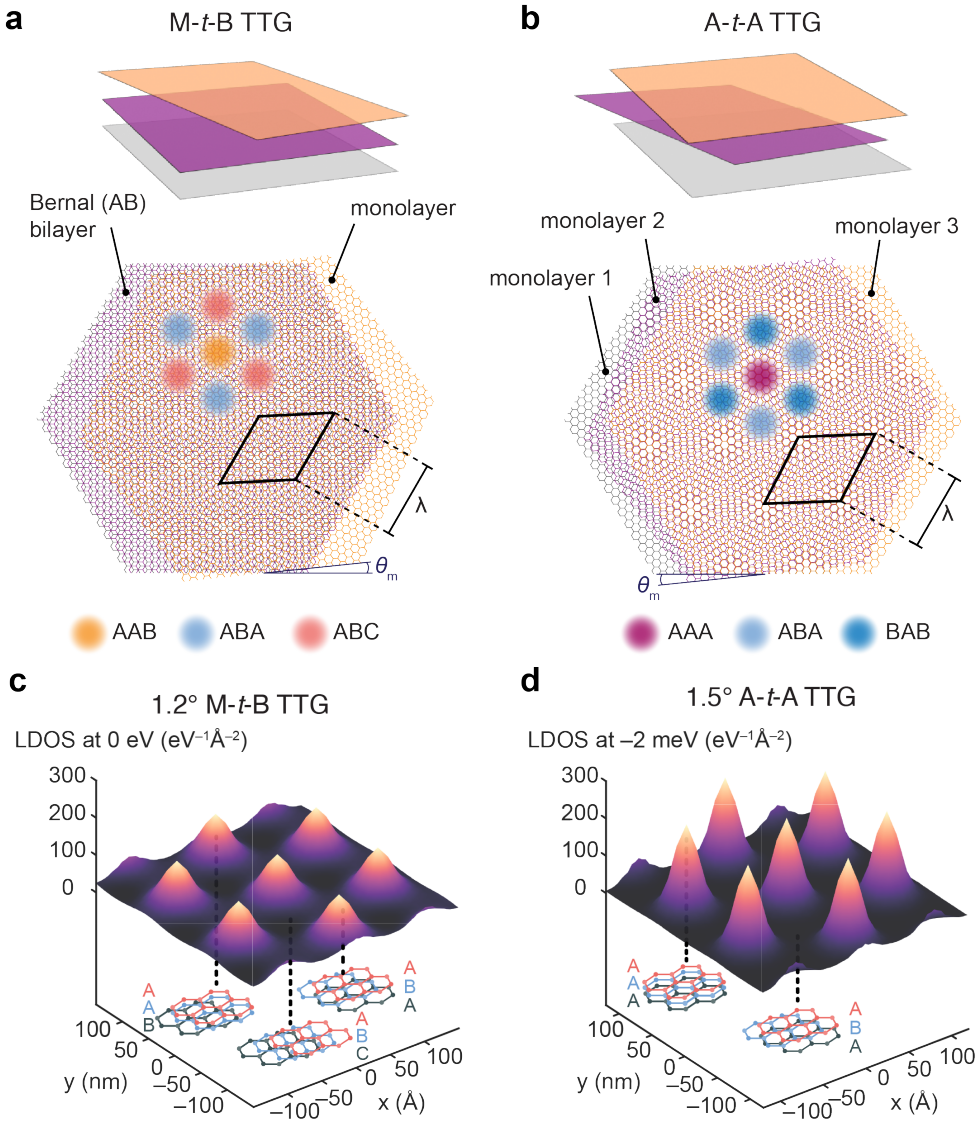

Figure 3.2: **a,b** Illustrations of two twisted trilayer graphene polytypes, with moiré wavelength λ. The black parallelogram outlines the moiré unit cell in each case. **c,d** Computed local DOS for 1.2° M-*t*-B **c** and 1.5° A-*t*-A **d**.

STM mode was utilized to first sever the graphene flakes into two or three pieces. The STM tip was centered under the microscope and the trace of cutting was confirmed by conducting a line scan before the tip touched the surface. The tip was then carefully lowered manually in 1 µm steps. The slight vibration of the live camera image was used as an indicator of when the tip landed on the surface. A slow line scan ($\approx$ 2 µm) was conducted for the tip to mechanically cleave the graphene. A longer line scan (than the cut) was then used to push graphene residues out of the flake of interest. The tip was then lifted and reapproached for the next cut if necessary.

Piezoelectric force microscopy (PFM) and scanning tunneling microscopy (STM) were used to evaluate the twist angle distribution and uniformity across the moiré samples (Figure 3.5b).[115] PFMs were performed on AIST-NT OmegaScope Reflection. Ti/Ir coated silicon probes from Nanosensor with a force constant of 2.8 Nm^{-1} and resonance frequency of 75 kHz were used. 2 V of AC bias with resonance frequencies at 820 kHz was used and the force was set at 25 nN. STM measurements were conducted using a Park NX10 STM module at room temperature and atmospheric pressure. Pt-Ir tips were prepared by electrochemical etching of 0.25 mm Pt-Ir wires in 1.5 M $CaCl_2$ solutions[101]. The scan images were taken with 0.2 V tip-sample bias and 100 pA current set point. More STM images of various samples can be found in Figure 3.3. Twist angles of various samples were determined using Delaunay triangulation on the Gaussian centers.[192,81]

The Raman maps for ABA/ABC trilayer graphene were obtained from the experimental Raman map data by fitting Lorentzian functions on spectra collected at each grid point. A Lorentzian function is defined as the following:

$$L(x) = \frac{A}{\pi}\left(\frac{\frac{\Gamma}{2}}{(x - x_0)^2 + \frac{\Gamma}{2}}\right) \tag{3.1}$$

where A is the amplitude, x_0 is the peak center, and $\frac{\Gamma}{2}$ is the half-width at half-maximum (hwhm). The full width at half maxima (fwhm) was obtained using fwhm = 2 $\times$ hwhm for each grid point's fitted Lorentzian function. The grid points were then colored using a diverging colormap, with the color red corresponding to larger fwhm, blue for smaller fwhm, and white for intermediate fwhm (see Figure 3.4).

Using SECCM, cyclic voltammograms (CVs) were measured with 2.0 mM $Ru(NH_3)_6^{3+}$—an ideal and well-established redox couple for interrogating outer-sphere ET kinetics[57, 192]—and 0.10 M KCl as the supporting electrolyte. In Figure 3.5c, a representative set of CVs collected from these different trilayer samples is shown. We find that the ABA domain of the flake shown in Fig. 2A exhibited the most sluggish rates of $Ru(NH_3)_6^{3+}$ electro-reduction, evinced by a half-wave potential ($E_{1/2}$) of –0.32 V, which is cathodically shifted substantially from the equilibrium potential, E^0, of –0.25 V for $Ru(NH_3)_6^{3+/2+}$ (all potentials are reported relative to the Ag/AgCl quasi-counter/reference electrode). However, the $E_{1/2}$ measured from the CV acquired at region II (ABC domain) of the same flake was –0.27 V, pointing to considerably more facile electroreduction kinetics on the rhombohedral trilayer as compared to the Bernal trilayer. For both tTG samples, reversible CVs with $E_{1/2} \approx$ –0.25 V were obtained, indicative of highly facile electrokinetics and heterogeneous electrochemical rate constants that exceed those of both ABA and ABC graphene considerably. These observations motivated the measurement of the variation of interfacial ET rates with θ_m.

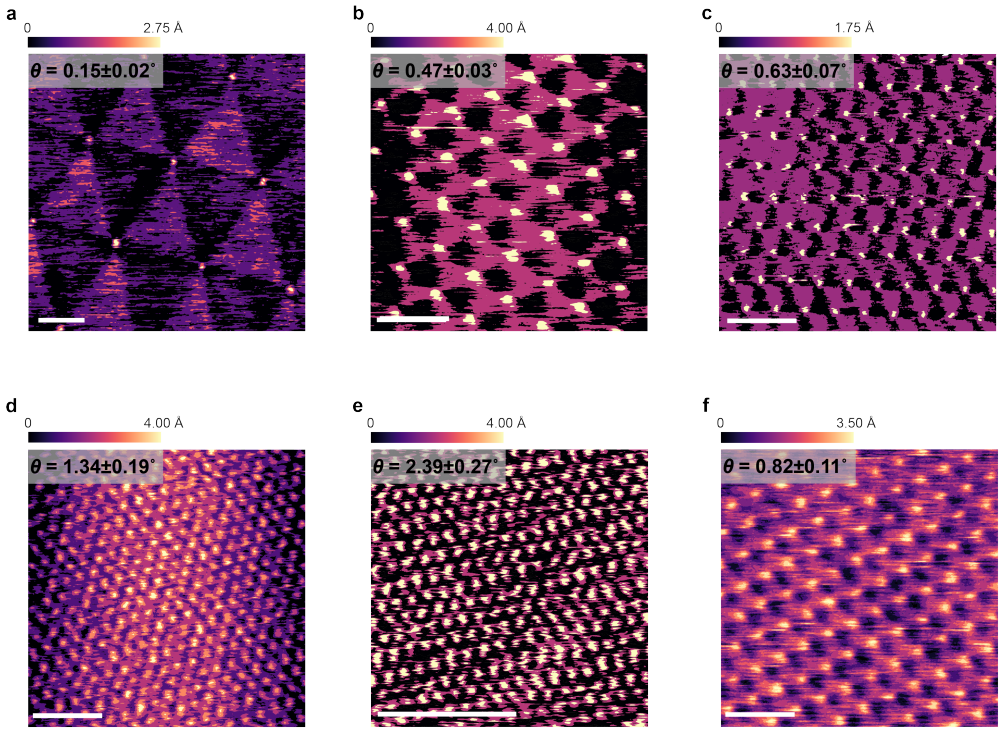

Figure 3.3: Representative constant current STM images of various M-*t*-B in **a** - **e** and B-*t*-M in **f** of different twist angles.

3.3 Angle-dependent electrochemistry on tTG

To quantitatively assess differences in interfacial kinetics associated with disparate electronic structures, we compared experimental CVs to those simulated with different standard rate constants, k^0, calculated with the Butler–Volmer model. The procedure is similar to what has been described in Chapter 2. Similarly, it is critical to account for the relatively small and potential-dependent quantum capacitance, C_q[192, 57] in these low-dimensional electrodes, which for a given applied potential, V_{app}, produces a dynamic electron or hole doping of the few-layer graphene by energy of eV_q (where e is the elementary charge and V_q is the chemical potential relative to the charge neutrality potential). The remainder, V_{dl}, persists as a drop across the electric double layer (so that $V_{app} = V_q + V_{dl}$). $C_q(V_q)$ was calculated for all trilayer systems (ABA, ABC, as well as M-*t*-B and A-*t*-A at various θ_m) (Figure 3.6A) using the respective computed band structures and DOS profiles. The corresponding plots of V_{dl}/V_{app} as a function of V_{app} are shown in Figure 3.6B. Taken together, these data reveal that flat electronic bands result in a more significant fraction of V_{app} partitioning

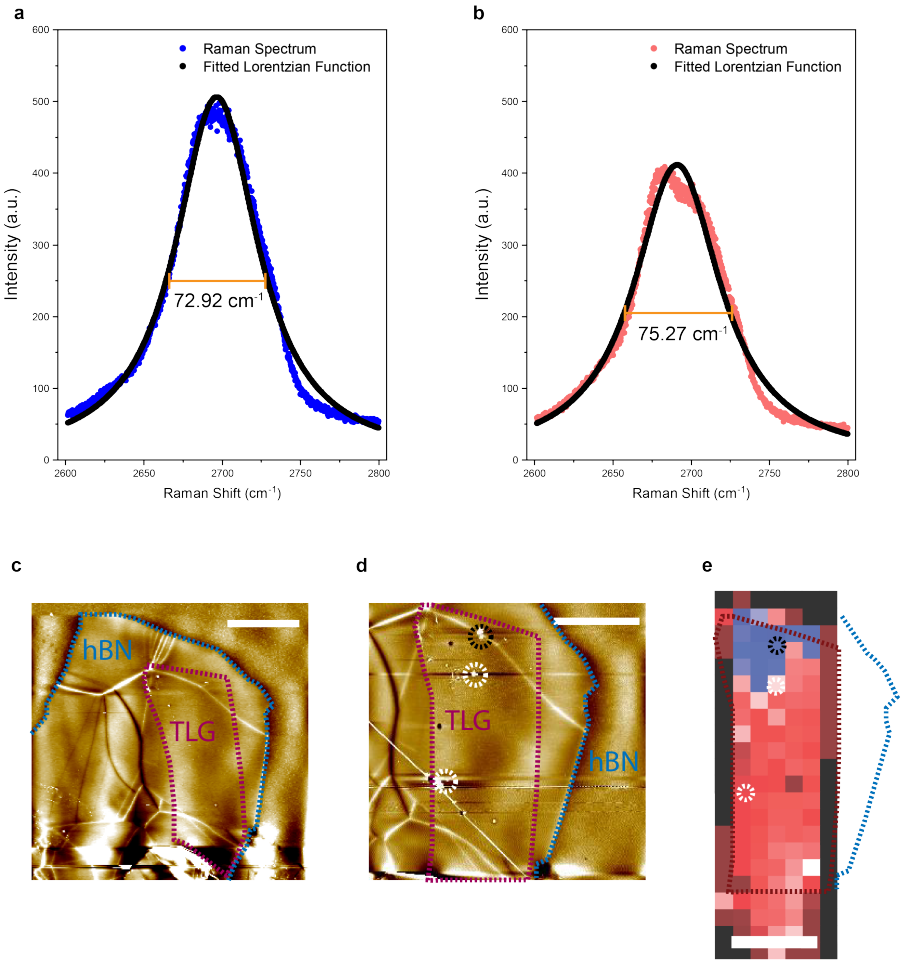

Figure 3.4: **a** Representative Raman spectrum of ABA graphene from 2550 - 2800 cm^{-1} (in blue) and a Lorentzian fitting of the spectrum. The full-width-half-max was determined to be 72.92 cm^{-1}. **b** Representative Raman spectrum of ABC graphene from 2550 - 2800 cm^{-1} (in red) and a Lorentzian fitting of the spectrum. The full-width-half-max was determined to be 75.27 cm^{-1}. **c-e** AFM images were measured on the same sample before in **c** and after **d** SECCM experiments. The red trace shows the trilayer graphene and the blue trace shows the bottom *h*BN. Black and white dotted circles highlighted residues from the measurements. Both images were taken on a Park AFM NX10 system with non-contact mode with a set point of 10 nm. **e** Raman map overlayed with the traces of the trilayer graphene and *h*BN. The measurements on the black dotted circle were used as rates on ABA graphene and those on the white circles were used as rates on ABC. Scale bar: 10 µm.

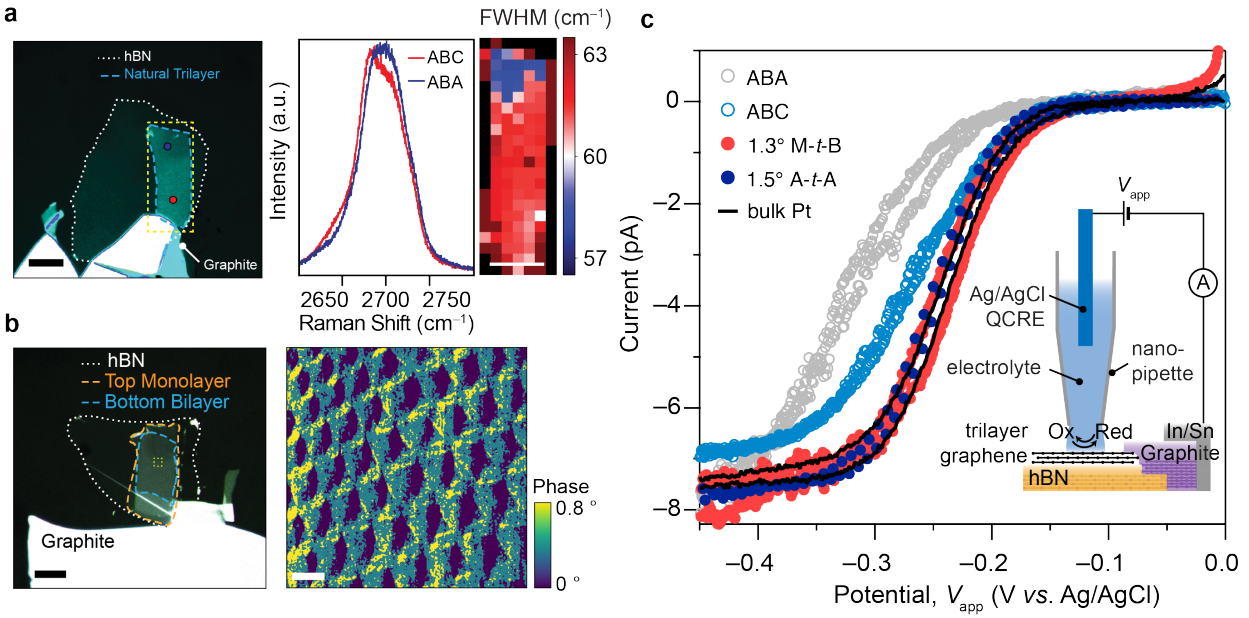

Figure 3.5: **a** Left: Optical micrograph of a device fabricated from an exfoliated trilayer graphene flake on hBN. Right: Confocal Raman spectra acquired in the sites in **a** marked with red (ABC domain) and blue (ABA domain) dots, along with the Raman map of the region indicated with a yellow box in **a**. Scale bars: 10 μm. **b** Left: Optical micrograph of an M-*t*-B device on hBN (Scale bar: 10 µm). Right: A lateral PFM phase image over the yellow boxed region in **b** reveals the moiré superlattice pattern. Scale bar: 50 nm. **c** Representative steady-state voltammograms of 2 mM $Ru(NH_3)_6^{3+}$ in 0.1 M KCl solution obtained at ABA and ABC trilayer graphene, along with 1.3° M-*t*-B and 1.5° A-*t*-A, compared to that obtained at a $\sim$ 40 nm thick platinum film. Scan rate, 100 mVs^{-1}. Inset illustrates the SECCM technique.

into V_{dl} near the charge neutrality potential. Notably, as shown in Figure 3.6a, changes in θ_m tune $C_q(V_q)$ and 'magic-angle' ($\approx 1.5°$) A-*t*-A displays higher C_q than 'magic-angle' ($1.2 - 1.3°$) M-*t*-B consistent with its overall greater DOS (Figure 3.5d).

After determining V_{dl} in this manner, we extracted k^0 values by identifying the simulated CV that was in closest agreement with the experiment[192]. The θ_m dependence of k^0 was measured by preparing M-*t*-B tTG devices with varying θ_m between 0.08° and 8.0° and acquiring CVs of $Ru(NH_3)_6^{3+}$ electroreduction by SECCM for each sample.

The SECCM nanopipettes were fabricated from single-channel quartz capillaries (inner and out diameters of 0.7 mm and 1.0 mm from Sutter Instrument) in a laser nano pipette puller. The program was set to heat 700, filament 4, velocity 20, delay 127, and pull 140 to generate pipettes of diameters around 200 nm, later confirmed with bright field TEM (see Figure 3.7). The transmission electron microscopy images of the nanopipettes were later obtained with a JEOL 1200EX transmission electron microscope operated at 100 keV. The top $\sim$ 1 mm portion of the pipette was attached to the

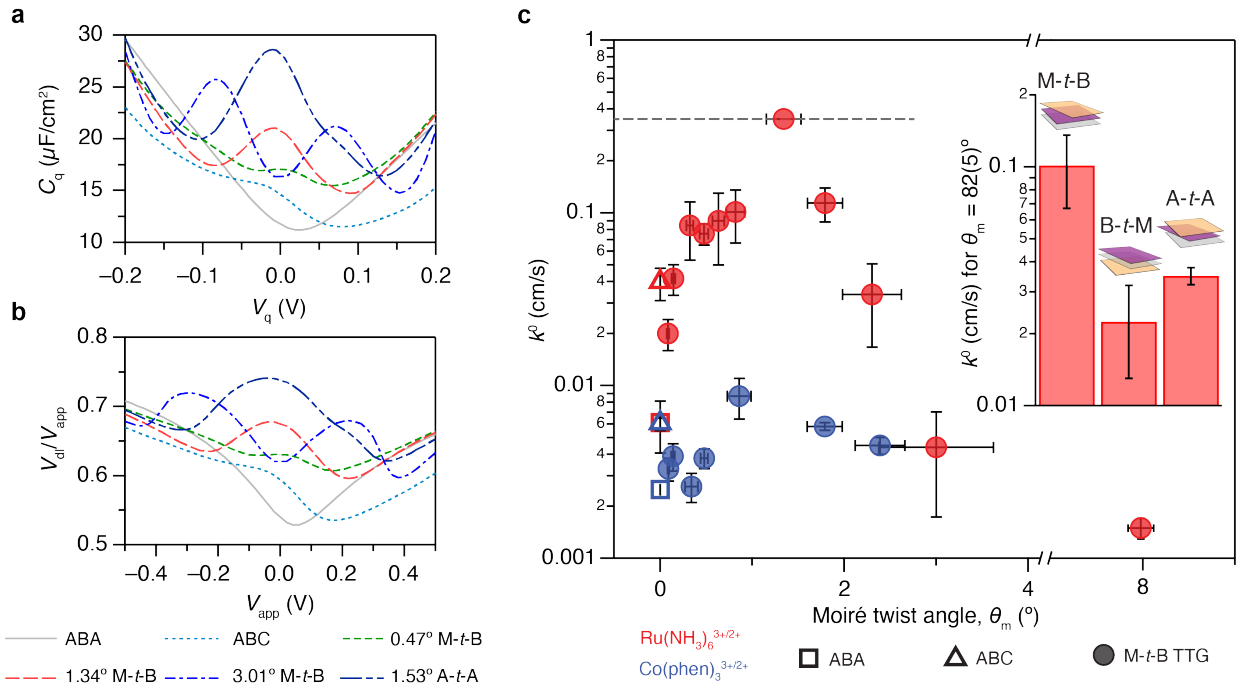

Figure 3.6: **a**, Calculated C_q as a function of the chemical potential (V_q) for ABA, ABC, and tTG using the respective computed band structures and DOS profiles. **b**, Calculated fraction of applied potential on the double layer (V_{dl}/V_{app}) as a function of the applied potential (V_{app}) for ABA, ABC, and tTG. V_q and V_{app} are relative to the charge neutrality potential. Taken together, these data reveal that flat electronic bands result in a more significant fraction of V_{app} partitioning into V_{dl} near the charge neutrality potential. **c**, Dependence of ET rate constant, k^0, on trilayer graphene stacking type (ABA, ABC) and θ_m for M-*t*-B tTG. Each marker denotes the mean of measurements made on samples within a standard deviation of the mean twist angle. The horizontal and vertical error bars represent the standard deviations of θ_m and the standard error of k^0. The inset shows comparison of k^0 values for M-*t*-B, B-*t*-M, and A-*t*-A tTG at $\theta_m = 0.82 \pm 0.05°$.

grid (PELCO Hole Grids) such that the pipette tip was positioned in the center hole, and the rest of the pipette was broken off. Selected area electron diffraction patterns were collected on an FEI Tecnai T20 S-TWIN transmission electron microscope with a LaB 6 filament operated at 200 kV.

The outer surfaces of the pipettes were silanized by dipping them into dichlorodimethylsilane for 3 - 5 seconds when nitrogen flowed through the inside of the pipettes. They were then filled with either $Ru(NH_3)_6^{3+}$ or $Co(phen)_3^{3+}$ solutions through a micro syringe. The pipettes were gently tapped and a gentle string of nitrogen was used to eliminate the bubbles. The pipettes were then inserted with a silver AgCl wire as a quasi-counter reference electrode (QCRE). The pipettes were carefully approached (0.2 µm/s) to the locations of interest while a -0.5 V (0.5 V for $Co(phen)_3^{3+}$) bias was applied. The meniscus achieved contact when a current of larger than 2 pA (or smaller than -2 pA) was observed. The pipette was allowed to stabilize for 30 s. Cyclic voltammograms (CVs) were then conducted by sweeping the potential at 100 mVs^{-1} between -0.6 to 0 V (0 to 0.8 V for $Co(phen)_3^{3+/2+}$) for 5 cycles. Multiple CVs were collected for each sample and small twist samples ($\theta \leq 0.15°$) with moiré wavelengths of more than 80 nm, only CVs recorded with nanopipettes more than 200 nm in diameter were included to ensure they surveyed multiple stacking domains. To survey electrochemical activities across a large sample, the pipette was retracted by 1 µm after CVs were measured and horizontally moved to a new location for a new approach.

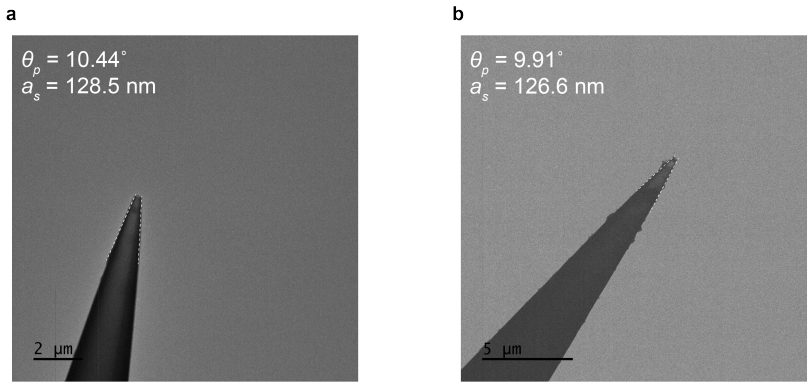

Figure 3.7: Representative TEM images of quartz pipettes used in SECCM before, in **a**, and after experiments in **b**.

Figure 3.6c shows the strong, non-monotonic variation in k^0 over two orders of magnitude from ABA and ABC graphene to $\theta_m = 8°$ M-*t*-B. For samples with $1° \leq \theta_m \leq 2°$ ET appears reversible within our accessible scan rates and so we cannot extract any kinetic information beyond noting that within this range of θ_m, $k^0 \geq 0.35$ cm/s. The quenched dependence of θ_m on k^0 (blue markers in Figure 3.6c) in analogous electrochemical measurements of the trisphenanthroline cobalt(III/II)

redox couple, $Co(phen)_3^{3+/2+}$ provides compelling evidence that it is the moiré flat bands that drive the observed angle-dependent electrokinetic modulation in tTG, as in tBLG.[192]

An unexpected observation of the factors controlling interfacial ET is made by comparing the electrochemical responses of tTG polytypes. A-*t*-A tTG, based on its massive DOS (Figure 3.2c,d) and giant C_q—which exceeds that of M-*t*-B (Figure 3.6a)—should be expected to yield the highest ET rates. However, while an effect of θ_m on k^0 is also observed in A-*t*-A samples, this variant of tTG displays consistently lower k^0 than M-*t*-B at similar θ_m (Figure 3.6c, inset). Further, B-*t*-M heterostructures, which consist of a Bernal bilayer placed with a twist atop a monolayer (*i.e.*, flipped versions of M-*t*-B), display markedly lower k^0 values than the corresponding M-*t*-B electrodes, notwithstanding an ostensibly identical overall electronic structure. These striking observations point clearly to effects governing the interfacial ET kinetics beyond simply the ensemble DOS.

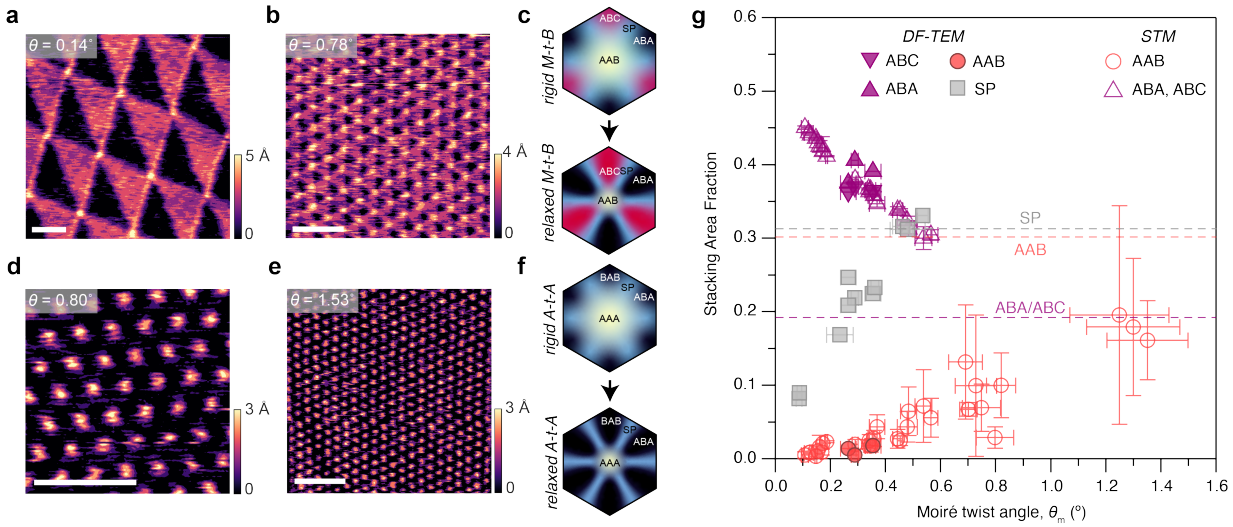

Figure 3.8: **a,b,d,e** Constant current STM images representative M-*t*-B **a,b** and A-*t*-A **d,e** samples. Scale bars: 50 nm **c,d** Qualitative illustrations of different stacking domains in rigid and relaxed M-*t*-B (**C**) and A-*t*-A **f** moiré unit cells. **g** Extracted area fraction of different stacking domains in M-*t*-B tTG. Error bars represent standard errors.

3.4 Local electron transfer kinetics in tTL

To fully understand these θ_m dependencies as well as the disparities between interfacial electron transfer kinetics of M-*t*-B, B-*t*-M, and A-*t*-A, we used STM (room temperature, constant current) to evaluate the role of lattice relaxation in controlling the area fraction of stacking domains in M-*t*-B and A-*t*-A tTG. In Figure 3.8a, a representative STM map of small-angle ($\theta_m = 0.14°$) M-*t*-B shows a clear contrast between the various stacking domains. Regions with higher local DOS appear

brighter than those with lower DOS since a larger tip-sample distance is required to maintain a constant current.[100] ABC domains, therefore, appear brighter than ABA domains owing to the native flatband of the ABC stacking type (Figure 3.1). These ABA and ABC domains (black and red regions, respectively) form alternating triangular patterns while the AAB region forms small circles of diameter $\approx$ 11 nm, which appear with the brightest contrast owing to the localization of the moiré flatband and associated large DOS on these AAB sites as shown in Figure 3.2c and Figure 3.9a (this is analogous to the localization of moiré flatbands on AA sites in tBLG[81]). For $\theta_m = 0.78°$ (Figure 3.8b), while the triangular ABA/ABC patterns have shrunk in size compared to those in Figure 3.8a, the diameters of AAB regions remained largely unchanged. For A-*t*-A, AAA domains are visible as bright spots (Figsure 3.8d,e), consistent with the localization of the large DOS on these regions (Figure 3.2d and Figure 3.9b),[168] with degenerate ABA and BAB regions requiring smaller tip–sample distances (dark regions) to sustain a constant STM current because of a lower local DOS.

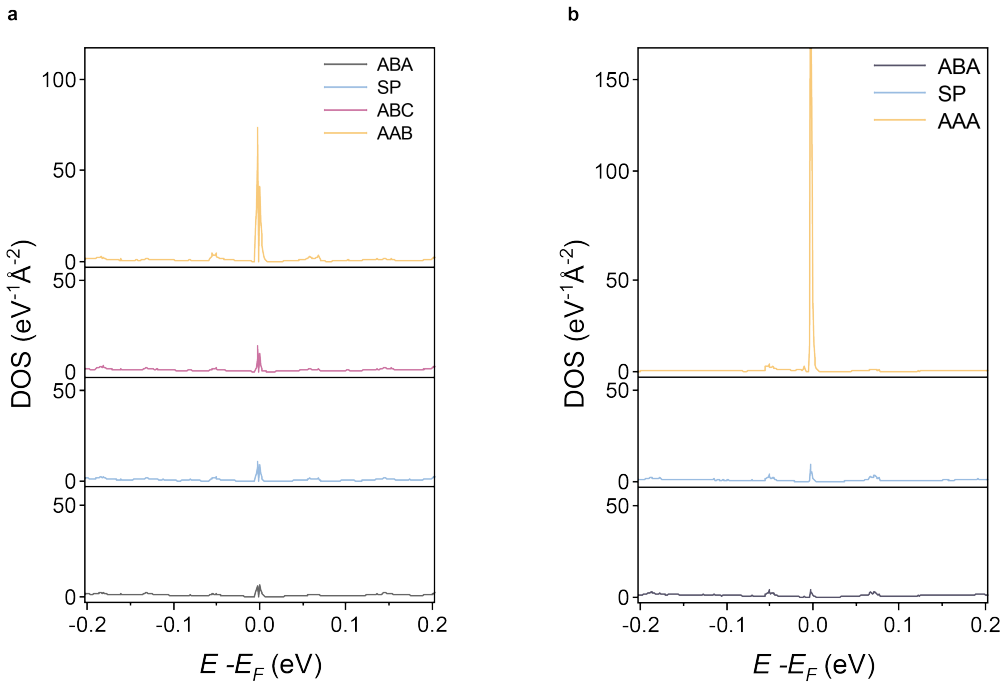

Figure 3.9: **a** Local density of states (LDOS) in $1.34°$ M-*t*-B. The yellow, red, blue, and black curves are the LDOS profile at AAB, ABC, saddle point (SP), and ABA regions respectively. **b** Local density of states (LDOS) in $1.53°$ M-*t*-B. The yellow, blue, and black curves are the LDOS profile at AAA, SP, and ABA regions respectively.

These area fraction distributions after structural relaxation explain the origin of the kinetic modulation observed in Fig. 3C at $\theta_m < 2°$ as being driven by θ_m-dependent area fractions of the

'topological defect'[152, 39] AAB and AAA sites. Our relaxation simulations (Figure 3.10) also show that at $\theta_m \leq 0.3°$, relaxation of these moiré superlattices reestablishes nearly commensurate ABA, BAB, and/or ABC domains with local DOS that should not deviate substantially from those of freestanding ABA and ABC trilayers. This observation is in line with previous experimental[79, 190, 100, 39] and theoretical studies[17, 39] of lattice relaxation in bilayer analogues. Therefore, by considering k^0 variations at $\theta_m < 1°$ in Figure 3.6c (which are also within the range of kinetically resolvable k^0), we can extract the local rate constant associated with the AAB and AAA stacking domains through equation 3.2 and equation 3.3 where β_i and κ_i^0 represent the area fraction and local standard heterogeneous ET rate constant, respectively, for stacking domain i.

$$k^0_{MtB} = \beta_{AAB}\kappa^0_{AAB} + \beta_{ABC}\kappa^0_{ABC} + \beta_{ABA}\kappa^0_{ABA} + \beta_{SP}\kappa^0_{SP} \tag{3.2}$$

$$k^0_{AtA} = \beta_{AAA}\kappa^0_{AAA} + \beta_{ABA}\kappa^0_{ABA} + \beta_{BAB}\kappa^0_{BAB} + \beta_{AAB}\kappa^0_{AAB} \tag{3.3}$$

As a result of the lattice relaxation effect discussed above, we can determine κ_{ABA} and κ_{ABC} from independent measurements of freestanding Bernal and rhombohedral trilayers (Figure 3.5c and 3.6c). In addition, we can assume that $\kappa^0_{SP} \approx \kappa^0_{ABA}$, which is justified on the basis of the STM images and calculated local DOS (Figure 3.10). This analysis allows us to extract standard electron transfer rate constants for the AAB (M-*t*-B), ABB (B-*t*-M), and AAA (A-*t*-A) topological defects.

Combined with previous electrochemical measurements at tBLG surfaces[192] we compare ET kinetics of $Ru(NH_3)_6^{3+/2+}$ among a wide array of stacking configurations from monolayer to trilayer graphene in Figure 3.11a. For atomic stacking orders naturally found in bulk graphite, we observed a gradual enhancement as the number of layers increases from monolayer to Bernal trilayer. This can be explained by a modest increase in DOS close to the Fermi level as the number of layers increases.[57] ABC graphene displays a pronounced augmentation in k^0 from that of ABA graphene associated with the intrinsic flat band of the rhombohedral system (Figure 3.1). Most notably, 'artificial' high energy stacking (AA, AAA, AAB, ABB) topological defects created by moiré superlattices exhibit extraordinarily high k^0 values, with that of AAB exceeding 3 cm/s, which is greater than that measured on bulk platinum electrodes (0.85-1.2 cm/s)[138], notwithstanding only consisting of three atomic layers.

3.5 Layer-dependent electron transfer kinetics in tTG

Figure 3.11a also shows the unexpected result that AAA sites display lower ET rates than AAB notwithstanding the higher DOS and C_q of AAA than AAB (Figure 3.2 and Figure 3.6). Strikingly, we also find that ABB sites yield slower ET kinetics than both AAB (despite identical overall DOS) and AA (despite higher overall DOS). Thus, while in-plane electronic localization and structural relaxation effects explain the dependence of k^0 on θ_m in tTG, the relative interfacial ET rates of AAB (M-*t*-B), ABB (B-*t*-M), and AAA (A-*t*-A) (Figure 3.6c inset and Figure 3.11a) appear not to correlate with DOS.

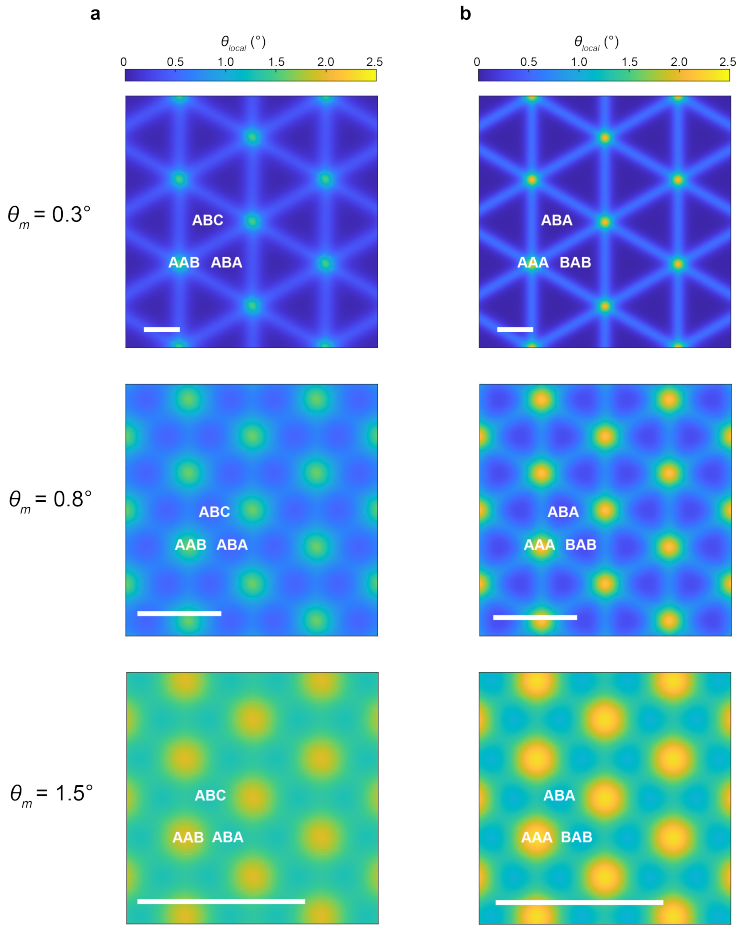

Figure 3.10: Calculated local rotation of M-*t*-B structures (in **a** and A-*t*-A structures (in **b**) at 0.3°, 0.8°, and 1.5°. Scale bar: 10 nm.

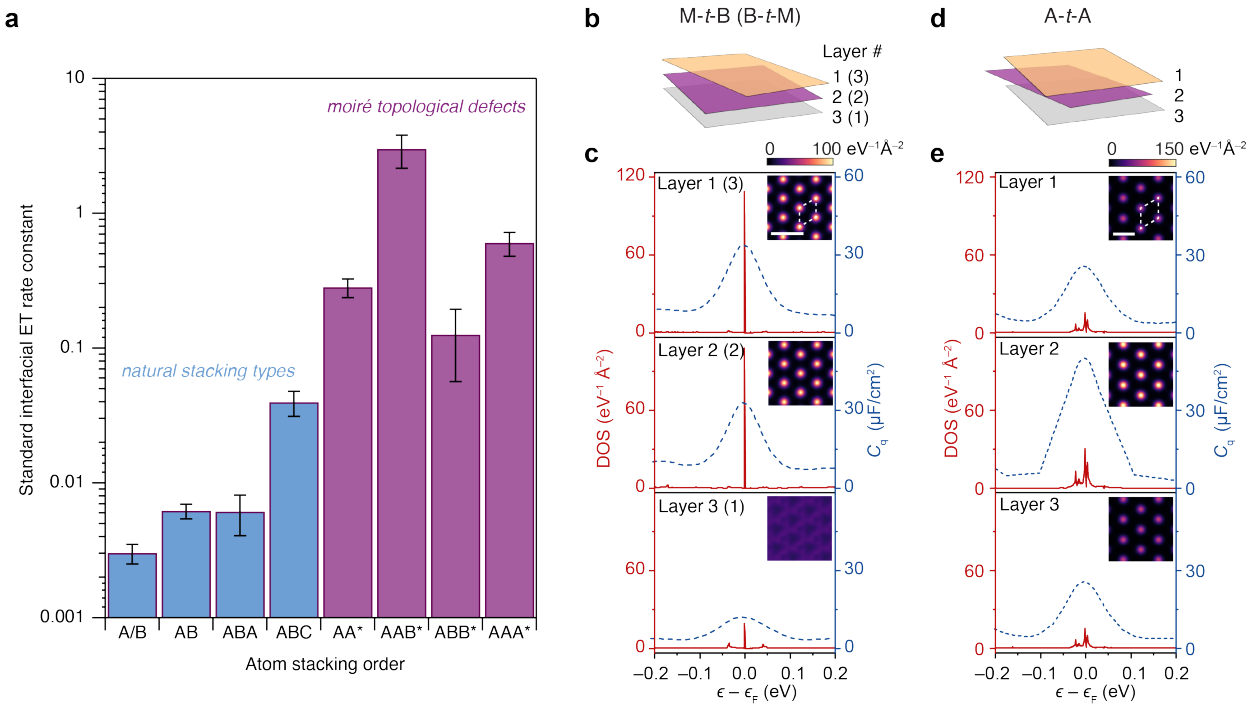

Figure 3.11: **a** Local standard $Ru(NH_3)_6^{3+/2+}$ ET rate constants at few-layer graphene in different stacking configurations. 'Artificial' moiré-derived stacking domains are labeled with an asterisk. Each bar is the mean local rate either measured (for natural stacking) or calculated (for artificial stacking) for small twist angle samples. The error bars represent the standard errors for the rates. **b** Schematic of M-*t*-B/B-*t*-M graphene layers. **c** Layer-dependent DOS profile for AAB stacking domains in M-*t*-B and B-*t*-M graphene at $\theta_m = 1.2°$. Insets show real space DOS maps of each layer at ϵ = -3 meV. **d** Schematic of the A-*t*-A layers. **e** Layer-dependent DOS profile for AAA stacking domains in A-*t*-A graphene at $\theta_m = 1.2°$. The insets show real space DOS maps of each layer at ϵ = -1 meV for $\theta_m = 1.2°$.

To explain these trends, Figure 3.11c–e shows layer-isolated local DOS(ϵ) profiles (Figure 3.11c,e) at the topological defects (AAB/ABB, AAA) along with calculated real-space DOS maps (insets in Figsure 3.11c,e). Figure 3.12 contains layer-dependent DOS at other twist angles. These calculations show how the DOS enhancements at AAB sites are distinctly localized on the top two layers of M-*t*-B structures (*i.e.* the 'AA' portions of AAB).[163] In contrast, the DOS at AAA sites are most strongly localized on the middle layer of A-*t*-A. This three-dimensional electronic localization (within a thickness of only three atomic layers) arising from different symmetries of these topological defects unveils the fundamental basis for the unexpected trends in ET rate constants at AAB, ABB, and AAA (Figure 3.6c and 3.11a): though the electrodes are only three atomic layers thick, ET rate constants are only correlated with the electronic properties precisely at the electrode-electrolyte interface.

These observations strongly hint at the role of interfacial electronic coupling (between the localized states on the electrode and the electron donor/acceptor in solution), electric double-layer effects, and/or interfacial reorganization energy as even more crucial than the overall DOS alone. Indeed, theoretical calculations based on the MHC model that accounts only for the θ_m-dependent DOS, but with a coupling strength, ν, and reorganization energy, λ, that are invariant with θ_m (see Supplementary Text and SI Fig. 7), vastly underestimate the dependence of k^0 on θ_m. These MHC calculations also likewise predict identical interfacial ET rates for M-*t*-B and B-*t*-M, which is clearly at odds with the experiment. Our experimental results, therefore, now motivate future theoretical work to adapt these MHC models to consider how electronic localization, which is deterministically tuned here by varying θ_m or tTG structure, modifies ν[132] — and/or λ[102], to bridge the gap between theory and experiment and extend our microscopic understanding of interfacial ET.

3.6 Conclusion

Controlling stacking geometries and twist angles in few-layer graphene, therefore, enables the manipulation of standard ET rate constants over three orders of magnitude. In particular, energetically unfavorable topological defects (AAA, AAB stacking domains), which are attainable only through the construction of a moiré superlattice, exhibit extraordinarily high standard rate constants. This electrochemical behavior arises from the moiré-derived flat bands that are localized in these topological defects. In addition to the effects of in-plane structural relaxation and electronic localization, the out-of-plane localization of the electron wavefunction on specific layers of twisted trilayer graphene results in measurable differences in ET rates at topological defects possessing different symmetries.

These results provide a powerful demonstration of the sensitivity of interfacial ET kinetics to the three-dimensional localization of electronic states at electrochemical surfaces and raise the question of whether traditional measurements of ET rates at macroscopic electrodes might severely underestimate the true local rate constant, which may be mediated by atomic defects that strongly localize electronic DOS, at these interfaces. In turn, SECCM measurements are shown to be powerful tools for probing layer-dependent electronic localization in atomic heterostructure electrodes.

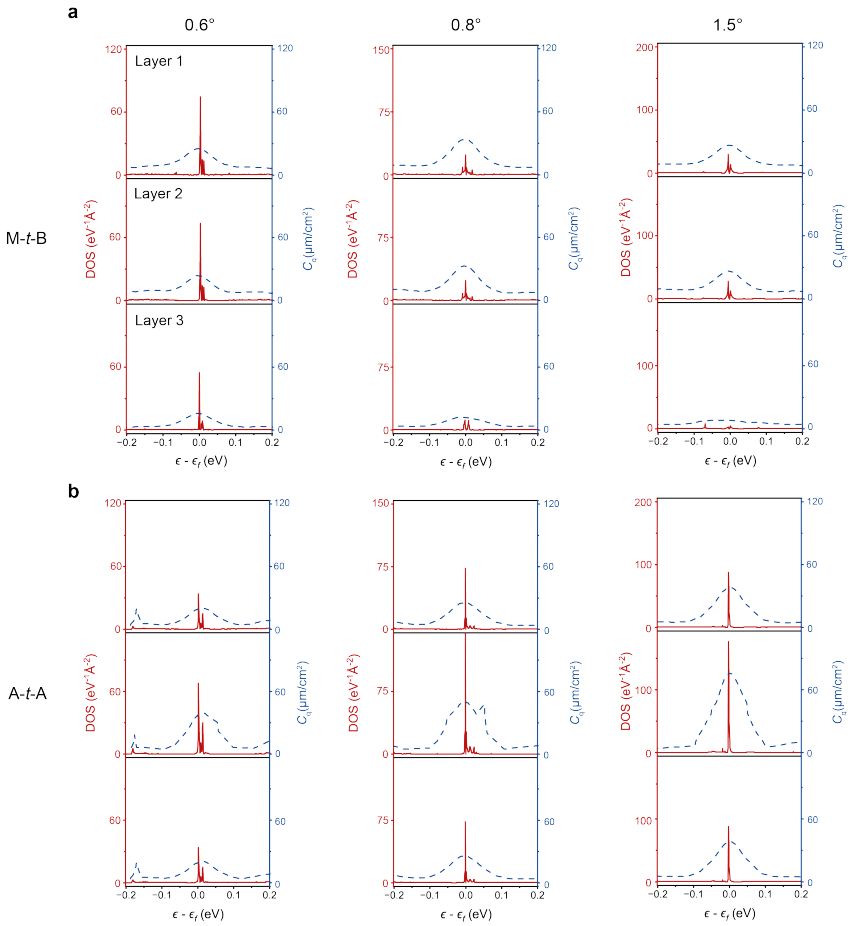

Figure 3.12: Layer-dependent local density of states on AAB domains of different twist angles M-*t*-B in (**a**) and on AAA domains of different twist angles A-*t*-A in (**b**). The twist angles here refer to the local twist angles at these stacking domains without considering relaxation.

Future experimental and theoretical work is needed to shed more light on the microscopic origin of these electron-transfer modulations in the context of reorganization energy, electronic coupling, and even electric double-layer structure. This work also heralds the use of moiré materials as a versatile and systematically tunable experimental platform for theoretical adaptations of the MHC framework applied to interfaces with localized electronic states, which are representative of defective surfaces that are ubiquitous to nearly all real electrochemical systems. In an applied context, twistronics is shown to be a powerful pathway for engineering pristine 2D material surfaces to execute charge transfer processes with facile kinetics, holding implications for electrocatalysis[191, 200] and other energy conversion device schemes that could benefit from ultrathin, flexible, and/or transparent electrodes that retain high electron-transfer kinetics.

Chapter 4

Towards tunable hydrogen evolution kinetics through moiré superlattices

4.1 Introduction

Hydrogen, as a clean and potent alternative to fossil fuels, stands prominently in the quest for sustainable and efficient energy sources.[145, 95] The electrochemical production of hydrogen, especially through the hydrogen evolution reaction (HER), has captured significant scientific interest as an alternative to the traditional industrial production methods such as steam reforming.[126, 136] This method not only addresses the escalating energy demands but also offers a renewable avenue for generating the primary material for one of the most critical industrial chemical processes, the Haber-Bosch process.[189]

The acidic electrochemical reduction of water via HER (see equation 4.1) is recognized as a two-step process. Initially, a proton is reduced to form the adsorbed hydride intermediate (H^*) through the Volmer reaction (equation 4.2). Subsequently, the intermediates combine to form H_2 either via the Heyrovsky reaction or the Tafel reaction (equations 4.3 and 4.4).

$$2H_3O^+ + e^- \rightarrow 2H_2O + H_2 \tag{4.1}$$

$$H^+ + e^- \rightarrow H^* \tag{4.2}$$

$$H^* + H^+ + e^- \rightarrow H_2 \tag{4.3}$$

$$H^* + H^* \rightarrow H_2 \tag{4.4}$$

The Sabatier principle[137], which posits that the interaction between a catalyst and reactant should be neither too strong nor too weak, is considered a crucial criterion in the search for optimal catalysts for electrochemical reactions, including the hydrogen evolution reaction (HER). This principle suggests that the overall reaction rate of a multi-step process will inevitably slow down if

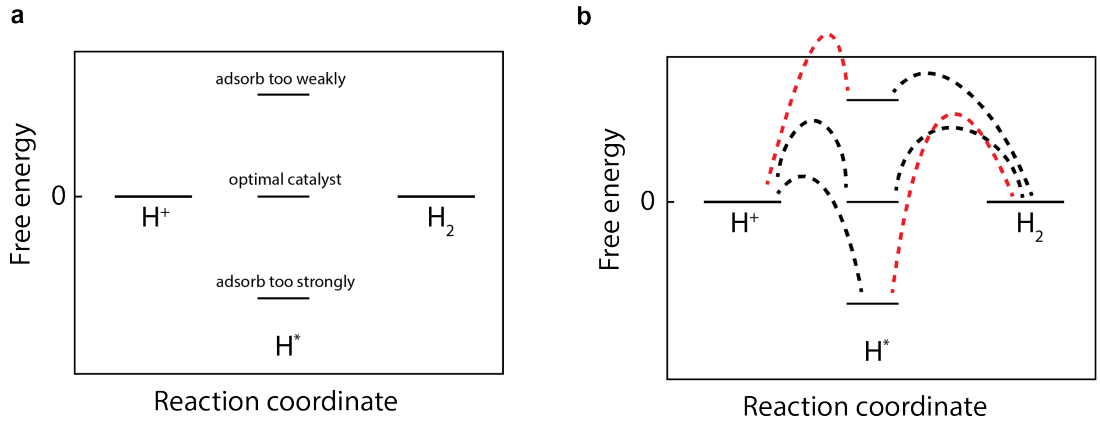

Figure 4.1: **a**, Free energy landscape for HER shows that the optimal catalysts should have thermal neutral adsorption. **b**, Transition state energy consideration based on Brønsted (Bell) – Evans – Polanyi (BEP) relationship. The red dotted line indicates the energy pathways for the rate-limiting step.

the intermediate either fails to transition to the product or fails to form on the surface (see Figure 4.1). Trasatti explored this relationship by plotting the exchange current density of HER on metal surfaces against the hydride bond strength.[165] This investigation yielded a "volcano plot," where metals like platinum, with intermediate bond strengths, outperform others.

Advancements in computational chemistry now permit the direct calculation of the binding energy between intermediates and catalytic surfaces.[54, 121] For HER, the calculated adsorption energy of the hydrogen intermediate (ΔG_{H^*}) has become a common metric to assess the strength of surface-proton interactions. Updated "volcano plots," which plot experimental catalytic reaction rates against ΔG_{H^*}, have reinforced the significance of thermoneutral intermediates for rapid catalysis.[66, 134, 122] The ΔG_{H^*} of ideal catalysts like platinum is close to zero, marking it as a key descriptor in the quest for alternative materials that can efficiently catalyze HER with minimal overpotentials and enhanced durability.[167, 66] This balance in interaction strength ensures that the catalyst facilitates rapid turnover rates by enabling easy formation and release of the intermediate hydrogen atoms, a critical aspect in achieving high-performance electrocatalysis.

In addition to the thermodynamically oriented Sabatier principle, experimental outcomes in catalysis are invariably influenced by kinetics. The Brønsted (Bell) – Evans – Polanyi (BEP) relationship provides a fundamental framework for understanding these kinetic effects by asserting a linear correlation between the free activation energy and the reaction free energy.[11, 21] As depicted in Figure 4.1b for the two-step HER process, a weak-binding catalyst typically shows a higher transition-state free energy for the first step due to its uphill nature in terms of free energy. Conversely, the BEP relationship indicates that for a strong-binding catalyst, the second elementary

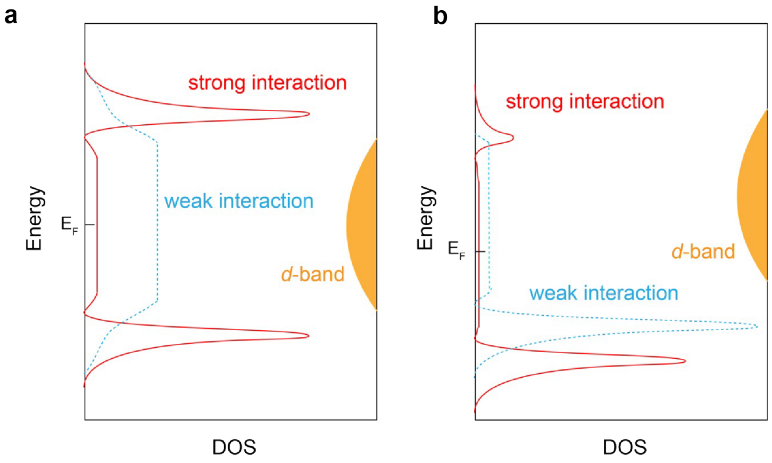

Figure 4.2: **a**, The reactant orbitals align with d-band and with stronger interaction (the red solid line), leading to better catalysis and **b**, The d-band is slightly higher than the reactant orbitals and with weak interaction (neon blue dashed line), leading to slower catalysis.

step will exhibit a higher transition-state free energy than the first.

The ideal scenario involves a thermoneutral catalyst, where the transition-state free energies for both steps are equivalent, and the overall highest transition state within the reaction landscape remains lower than those observed with either weak-binding or strong-binding catalysts. This scenario is reflected in the "volcano plots" and implies that optimal catalytic activity may require considerations beyond just ΔG_{H^*}.

Schmickler and colleagues have further explored these "volcano plots" using experimental data from oxide-free metal surfaces, challenging the universal applicability of this model while identifying additional factors contributing to the superior activity of platinum.[134, 144, 140] They concluded that a proficient catalyst should not only align with Sabatier's principle but also possess a d band that spans the Fermi level and engages in a strong and extensive interaction with the hydrogen 1s orbital. The significance of this long-range interaction, occurring over distances around $0.5\mathring{A}$ from the adsorption site, lies in its facilitation of electron transfer to the proton.[141] This interaction, as illustrated in Figure 4.2, leads to a more pronounced splitting and stabilization of the transition state when the d-band effectively interacts with hydrogen and is centered at the Fermi level (see red trace in Figure 4.2a). Such interactions lower the transition state energy, enhancing the kinetics of the rate-limiting step in HER, ultimately promoting faster catalytic processes.

As highlighted in Chapter 1, transition metal dichalcogenides (TMDs) stand out for their significant potential in catalytic applications.[121] Particularly notable is the adsorption energy at the edge sites of group six TMDs, specifically 2*H* MoS_2, which is comparable to that of platinum, as outlined in Table 4.1.[66, 95, 93, 8] However, the basal planes of these materials tend to be catalytically inert[8] and suffer from low conductivity due to their inherent semiconducting

properties. To optimize their catalytic performance, considerable effort has been directed towards increasing the number of active edge sites[70] and enhancing basal plane activity by introducing sulfur vacancies that mimic the edge-like properties.[95, 93]

The polymorphic nature of TMDs adds another layer of complexity and opportunity. For example, MoS_2 at room temperature predominantly exists in the 2*H* (trigonal prismatic) phase but can be transitioned to the more metallic 1*T* (octahedral) phase through electrochemical etching.[45] Similarly, $MoTe_2$ can be synthesized in both the 2*H* and the distorted octahedral $1T'$ phases, each offering distinct electronic and catalytic properties.[69, 105, 77] This phase tunability provides a promising avenue to engineer TMDs with enhanced metallic characteristics, potentially improving their activity towards hydrogen evolution reactions, as evidenced in Table 4.1.[45]

Table 4.1: ΔG_{H^*} of group VI TMDs. Edge is taken as metal exposed edge or in the case for $1T'MoTe_2$, metal exposed vacancies. Values are taken from reference [167] if not otherwise noted.

Group VI TMDs	**2*H* basal plane ΔG_{H^*} (eV)**	**2*H* edge ΔG_{H^*} (eV)**	**1*T*/1T' basal plane ΔG_{H^*} (eV)**	**1*T*/1T' edge ΔG_{H^*} (eV)**
MoS_2	1.92	0.06	0.12	0.12
$MoSe_2$	2.13	0.02	0.66	0.48
$MoTe_2$	-0.51[158]	–	-1.58[158]	0.77[146]
WS_2	2.23	-0.04	0.25	0.12
WSe_2	2.31	0.17	0.85	0.49

As highlighted in earlier chapters, the exciting field of "twistronics" offers new possibilities for tuning the electronic and chemical properties of materials, particularly for two-dimensional (2D) van der Waals (vdW) compounds such as transition metal dichalcogenides (TMDs).[78, 119, 80, 160] While graphene's potential through moiré pattern engineering has been extensively explored, TMDs present a unique set of characteristics that differentiate them from graphene, primarily due to their lack of $180°$ rotational symmetry. This asymmetry results in two distinctive types of moiré bilayer structures: parallel (P, near $0°$) (see Figure 4.5a) and anti-parallel (AP, near $180°$), each manifesting unique low-energy electronic band structures.

The AP orientation of group VI TMDs, including those based on molybdenum and tungsten, is particularly notable for exhibiting a series of ultraflat bands. These bands, attributed to in-plane lattice reconstruction and the formation of triangular moiré potential wells, span a range of twist angles rather than forming only at specific "magic" angles.[119, 92] This characteristic not only broadens the scope of potential applications but also enhances the versatility of TMDs for tuning material properties through twist angle variability. The additional phase variability of TMDs further increases the number of potential structural configurations, providing a rich template for optimizing interfacial reactivity across a broad spectrum of electrochemical reactions, especially in catalysis.

While previous studies have demonstrated the promise of TMD moiré superlattices in catalysis[72,

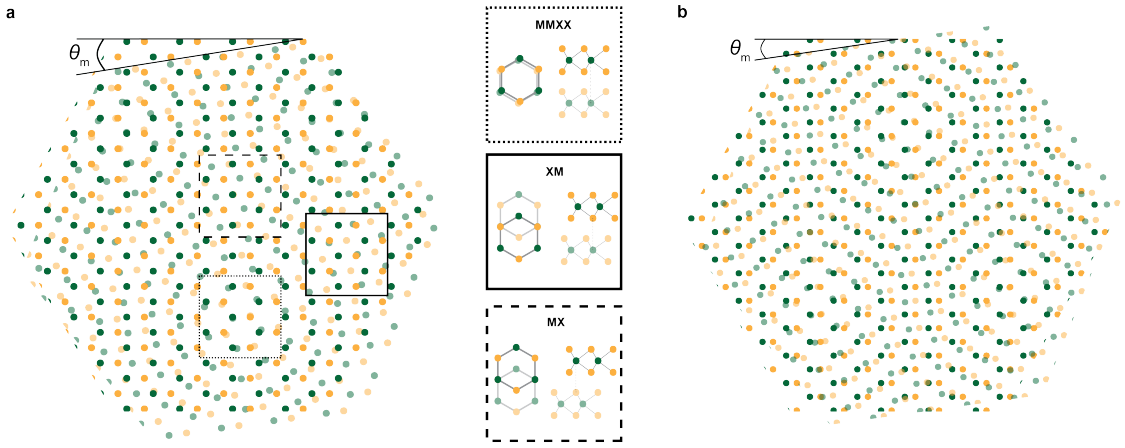

Figure 4.3: **a**, Illustration of a parallel stack of twisted bilayer MoS_2. The unique stacking domains are shown on the right. **b**, Illustration of a parallel stack of twisted bilayer $1T'$ $MoTe_2$.

180], these have predominantly utilized nano-scrolls of TMDs. This approach, however, leads to a non-uniform distribution of twist angles and introduces strain, potentially confounding the isolated effects of twisting on catalytic properties. Therefore, a dedicated study that methodically isolates and evaluates the impact of twisting on hydrogen evolution reaction (HER) catalysis remains a crucial next step. Such research could unlock further insights into the interplay between structural configuration and catalytic efficiency, paving the way for the development of next-generation catalysts that leverage the unique properties of TMD-based moiré superlattices.

Figure 4.3 shows two of the structures we have looked at. Parallel twisted MoS_2 (Figure 4.3a) resembles the structure of twisted bilayer graphene. Electron density of states localizes in MMXX stacking domains.[170, 201] This electron "hot spot" is interspersed by MX and XM stacking domains. The structure of twisted $1T$' has not been fully studied. This can be due to the difficulty in obtaining pristine monolayer $MoTe_2$ without surface oxidation.[118] Nevertheless, the structure of distorted $1T$ resembles that of twisted $1T$ structure.[202] We expect electron density to localize within regions where both Mo and Te are eclipsed. Furthermore, due to the semi-metallic nature of $1T$' $MoTe_2$, band flattening similar to twisted graphene structures is suggested.

4.2 Synthesis of TMDs

To ensure the highest quality of the crystals of transition metal dichalcogenides (TMDs) used in our device fabrication, we focused on growing single crystals of $2H$ MoS_2 and $1T'$ $MoTe_2$ via solid-state synthesis.[38] The presence of impurities and doping elements in commercially obtained crystals can drastically alter their electrochemical properties,[99] making it critical to control the synthesis

environment. The high melting points of these compounds are a significant challenge when growing Group VI TMDs from elemental powders.[199] To address this, we used fluxes—chemicals that lower the reaction mixture's melting temperature—to facilitate crystal growth. Specifically, Sn was used for MoS_2 synthesis[199] and NaCl for $1T'$ $MoTe_2$.[82]

In our procedure, elemental molybdenum (3N), sulfur (6N), and tin (5N) served as the starting materials for MoS_2. These were placed into a quartz ampoule, which was evacuated to 5.010^{-5} Pa and sealed. The ampoule was then positioned in a single-temperature-zone muffle furnace (Thermo Scientific, Asheville, NC, USA), where it was heated to 1150 °C over 20 hours and maintained at that temperature for an additional 25 hours. Following this, the system was cooled slowly to 1000 °C at a rate of 3 °C per hour, held for 20 more hours, then the melt-containing ampoule was centrifuged for 3 minutes at 1500 rpm. The resulting bulk MoS_2 single crystals were recovered after dissolving the Sn flux in concentrated hydrochloric acid for one day at room temperature.

For $1T'$ $MoTe_2$, a similar protocol was followed, albeit with NaCl as the flux agent. Here, the ampoule was quenched rapidly from 1000 °C, and stripe-shaped crystals were carefully selected from among the NaCl crystals.

Optical images of these millimeter-sized layered crystals (Figures 4.4a and d) exhibit their quality. The Raman spectrum of MoS_2 (Figure 4.4b) shows two peaks around 380 cm^{-1} and 405 cm^{-1}, corresponding to the $E^1{}_{2g}$ and A_{1g} phonon modes, consistent with previous reports.[199, 96, 129] The PXRD pattern of MoS_2 (Figure 4.4c) displays three recognizable peaks aligned with [00l] planes, indicating preferential crystal orientation.[67] Conversely, the PXRD pattern of $1T'$ $MoTe_2$ shows broadened peaks due to oxidation.[118] Detailed comparison with calculated spectra for 2*H* $MoTe_2$ and NaCl confirms that the crystals are phase-pure, setting a robust foundation for subsequent device applications.

4.3 SECCM investigation of twisted 2*H* MoS_2

Samples of twisted bilayer 2*H* MoS_2 (see Figure 4.5a and b) were fabricated via the "cut and stack" method described in Chapter 3. Compared to graphene-based samples, graphite was used as a bottom substrate instead of *h*BN to minimize lateral resistance of 2*H* MoS_2.[114] Samples were carefully examined with constant current STM. STM measurements were conducted using a Park NX10 STM module at room temperature and atmospheric pressure. The scan images were taken with -1.5 V tip-sample bias and 100 pA current set point. Higher bias was utilized to overcome the semiconducting nature of 2*H* MoS_2. [171] However, significant noise was present, making twist angle determination challenging. Previous STM studies of TMD moiré materials utilized low temperature environment.[147, 201, 92] Therefore, in order to achieve better resolution, one can resort to low temperature STM or post measurement TEM to elucidate the twist angle and reconstruction of twisted 2*H* MoS_2 samples.

SECCM was utilized to measure linear sweep voltammetry (LSV) on twisted bilayer, bilayer and bulk 2*H* MoS_2 samples. 0.5 M KCl and 0.5 M H_2SO_4 was used to fill the nanopipette of desired radius (100-400 nm). Ag/AgCl was used as the quasi-reference counter electrode (QRCE). The pipette was approached toward the surface slowly (2 μm/s) while -0.5 V vs. Ag/AgCl was applied to

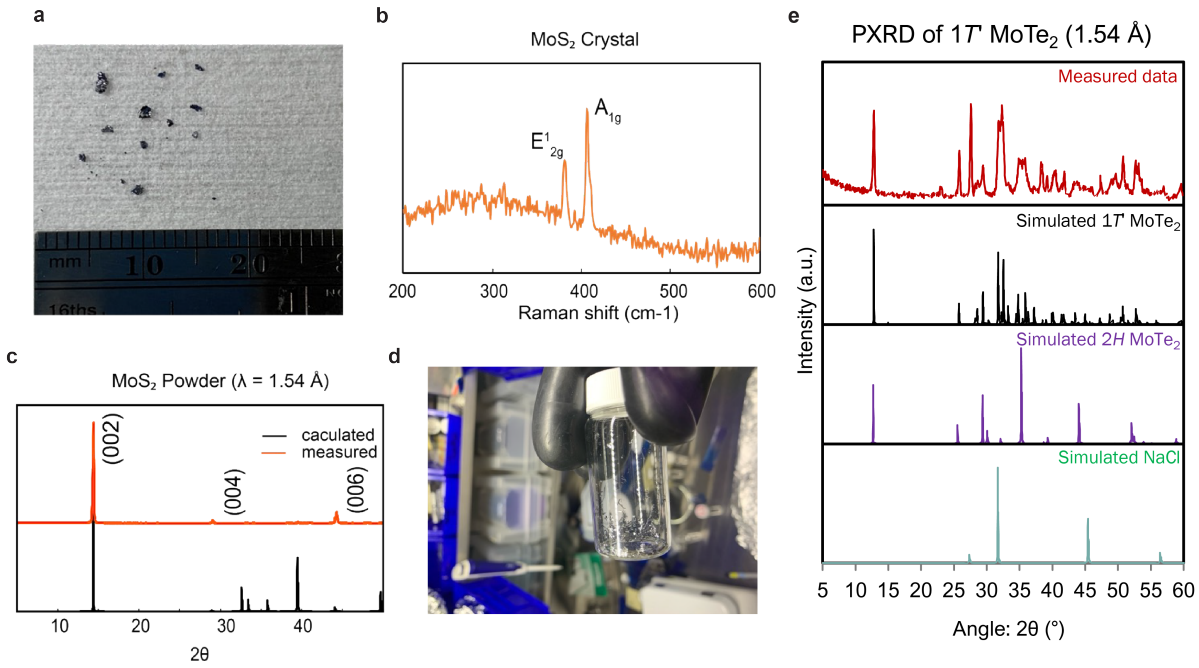

Figure 4.4: **a**, Image of the synthesized $2H$ MoS_2 crystals. **b**, Raman spectroscopy of $2H$ MoS_2 crystals.**c**, PXRD pattern of grounded MoS_2 cystals. **d**, Image of the as synthesized $1T'$ $MoTe_2$. **e**, PXRD pattern of grounded $1T'$ $MoTe_2$ crystals.

the sample. After contact, the droplet was allowed to stabilize for 30 seconds. SECCM-CV was conducted by sweeping potential from 0 to -1000 mV at 200 mV/s (see Figure 4.5d). Intriguingly, within cycled 5 times, the reaction rate of HER significantly increases, evidenced by the right shift of CVs. CV would only stabilize after 15 - 20 cycles. Initially, we hypothesized that this was caused by the instability of the meniscus. [172]

We tested our hypothesis by conducting electrochemically active surface area (EASA) measurements using the relationship,

$$i = C_{dl}\frac{dV}{dt} \tag{4.5}$$

where i is the current, C_{dl} is the double layer capacitance, and $\frac{dV}{dt}$ is the scan rate. The CV curves in a non-faradaic region (-0.2 to 0.45 V) were plotted as a function of various scan rates (10, 20, 30, 40, 50, 60, 80, 100, 120, 140, 180 mV/s) (Inset of Figure 4.5f). C_{dl} was assessed from the slope of the linear regression between the current differences ($\Delta i = (i_{anodic} - i_{cathodic})/2$) in the middle of the potential window of CV curves versus the scan rates (inset of Figure 4.5f). This measurement was conducted several times between CV scans to HER regions (-1000 mV). To our surprise, no significant change of C_{dl} was observed between CV scans, suggesting a relatively constant EASA. Therefore, the increasing rate of reaction probably suggests new formation of active sites in the

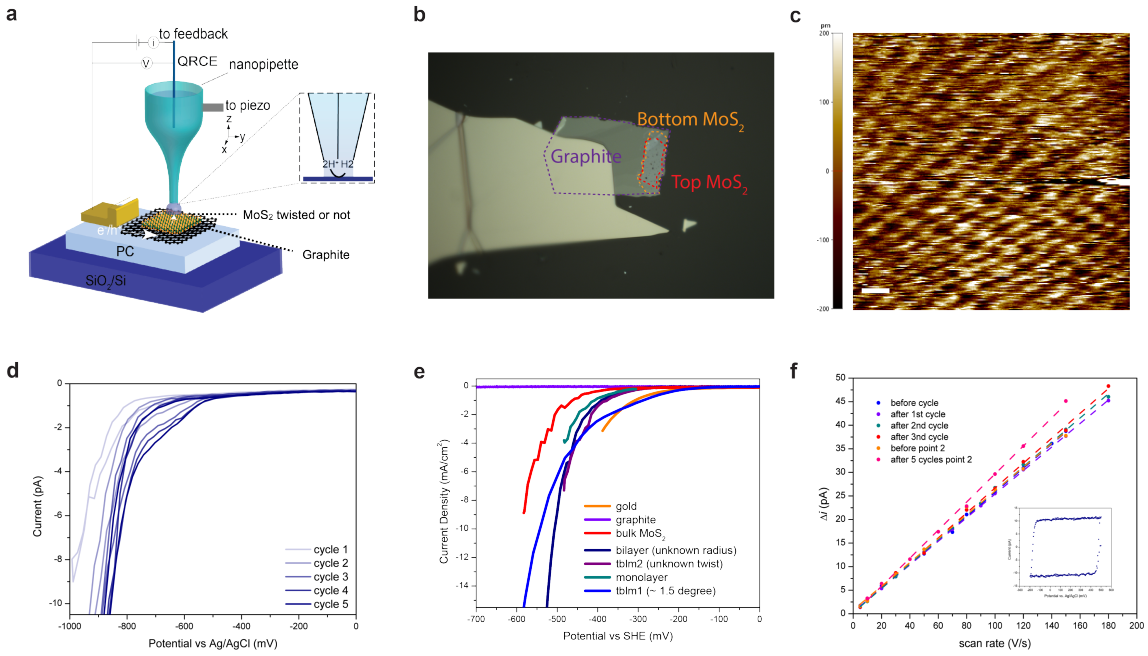

Figure 4.5: **a**, Schematic of the SECCM sample setup for twisted bilayer 2*H* MoS_2. **b**, Optical image of a representative sample. Scale bar: 10 µm **c**, Constant current STM images of a twisted bilayer 2*H* MoS_2 sample. Scale bar: 10 nm. **d**, Representative cyclic voltammogram (CV) of HER on twisted bilayer 2*H* MoS_2. The CV was cycled 5 times. Scan rate: 200 mV/s. **e**, Representative linear sweep voltammograms (LSV) of HER on various samples. Scan rate: 200 mV/s. **f**, Electrochemically active surface area (EASA) measurements conducted on a twisted bilayer 2*H* MoS_2 sample. The inset shows the CV collected at 70 mV/s.

form of vacancies on MoS_2. Previous studies indeed highlighted the possibility of electrochemical generation of S vacancies in MoS_2 when more than 0.4 V of overpotential is applied.[166]

The LSV of HER on various samples was collected after CV was used to cycle the sample past stability (see Figure 4.5e). Contrary to literature[95], all MoS_2 has slower kinetics than gold as more overpotential was required for these samples. This results suggests the pristine basal plane of synthesized MoS_2 even after electrochemical generation of S vacancies can be probed through SECCM without convolution by edges and grain boundaries. The twisted samples measured so far do not suggest any significant enhancement over that of bilayer MoS_2 (see blue and purple trace in Figure 4.5e). The twist in these samples has yet to be confirmed and can deviate from "magic angle" region. Furthermore, due to the semiconducting nature of MoS_2, flat band generation might not affect the kinetics of HER significantly. We therefore also investigated a semimetallic class of TMD.

4.4 SECCM investigation of twisted $1T'$ $MoTe_2$

Samples of twisted double bilayer $1T'$ $MoTe_2$ were fabricated using the "tear and stack" method outlined in Chapter 2, with all procedures carried out within the controlled environment of an argon-filled glovebox. Due to the air sensitivity of $1T'$ $MoTe_2$, employing STM tip cutting was impractical, as the oxidized interface between layers would result in weak interactions, effectively isolating each layer.

Upon completion of assembly, the samples were necessarily removed from the glovebox due to the experimental setup's requirements, exposing them to potential surface oxidation (Figures 4.6a and b). Consequently, STM measurements were challenging, making it necessary to determine the twist angle post-experimentally through TEM analysis.

For electrochemical characterization, Scanning Electrochemical Cell Microscopy (SECCM) was employed to perform linear sweep voltammetry (LSV) on twisted double bilayer, trilayer, and bulk $1T'$ $MoTe_2$ samples. The nanopipette used was filled with a solution of 0.5 M KCl and 0.5 M H_2SO_4, using Ag/AgCl as the quasi-reference counter electrode (QRCE). The approach of the pipette towards the sample surface was controlled at a rate of 2 µm/s, with an initial potential of -0.3 V vs. Ag/AgCl applied. After establishing contact, the system was allowed to stabilize for 30 seconds before commencing the SECCM-CV, sweeping the potential from 0 to -1000 mV at a rate of 200 mV/s (Figure 4.6c). Notably, $MoTe_2$ samples exhibited greater stability under overpotentials compared to MoS_2 samples.

To assess current density, the meniscus size was first estimated by measuring the nanopipette radius using brightfield TEM (Figure 4.6d; see also Chapter 3 for experimental details). Representative LSVs collected from $1T'$ $MoTe_2$ samples using two different nanopipettes are displayed in Figure 4.6e. These results indicated that the twisted double bilayer $MoTe_2$ exhibited faster kinetics than its trilayer and bulk counterparts. To address potential discrepancies caused by differences in estimated droplet sizes between the two pipettes, the LSVs recorded with pipette 3 were calibrated. Assuming the LSVs measured on bulk $MoTe_2$ were consistent, a proportionality constant derived from these measurements was applied to all other CVs recorded with this pipette, affirming the enhanced kinetics of the twisted double bilayer $MoTe_2$ (Figure 4.6f).

The twist angles were subsequently determined using selected area electron diffraction. After electrochemical testing, the twisted double bilayer $1T'$ $MoTe_2$/*h*BN samples were transferred onto a holey silicon nitride membrane. Diffraction patterns and darkfield images were obtained using a Thermo Fisher Scientific Titan-class microscope equipped with a Gatan UltraScan camera and operated at 60 kV (Figures 4.6g and h). The twist angle detected was significantly small ($\ll 1°$), likely due to substantial relaxation of the $MoTe_2$ post-fabrication. Future experiments should consider targeting larger initial twist angles to compensate for this relaxation.

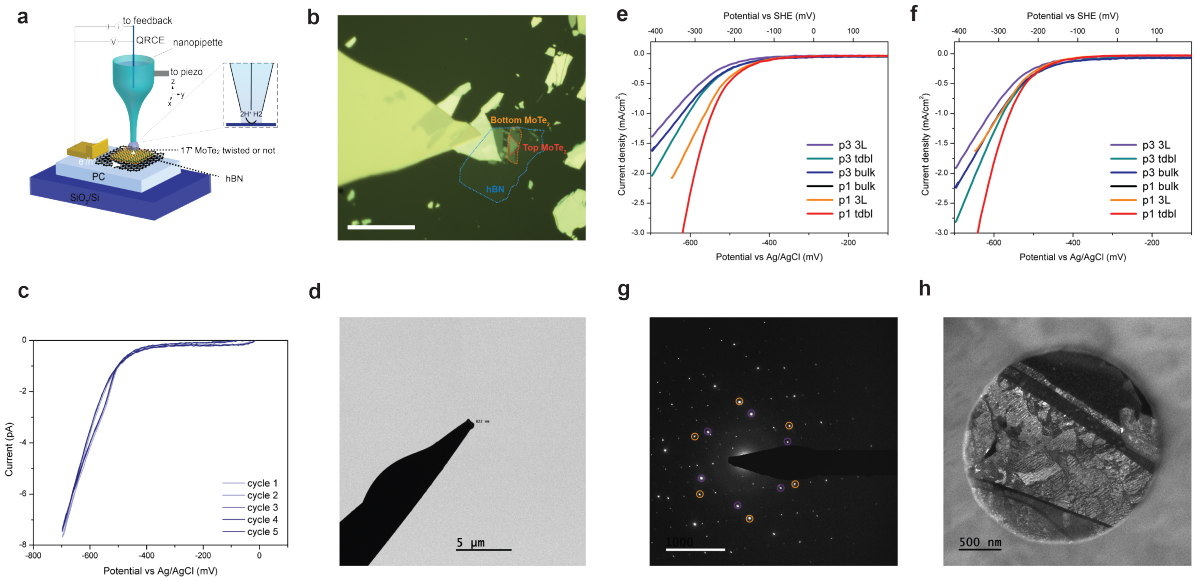

Figure 4.6: **a**, Schematic of the SECCM sample setup for twisted bilayer $1T'$MoTe$_2$. **b**, Optical image of a representative sample. Scale bar: 10 µm **c**, Representative cyclic voltammogram (CV) of HER on twisted bilayer $1T'$. The CV was cycled 5 times. Scan rate: 200 mV/s **d**, Typical bright-field TEM image of a nanopipette. **e**, LSVs measured on various samples with two pipettes (p1 and p3). Scan rate: 200 mV/s. **f**, Calibrated LSVs by assume LSVs measured on bulk $1T'$MoTe$_2$ are coincidental. **g**, Selected area diffraction of a $1T'$ MoTe$_2$ sample. The orange circles indicates diffraction peaks corresponding to $1T'$ MoTe$_2$ layers while the purple circles indicate those of the *h*BN layer. Scale bar: 5 nm^{-1} **g**, Dark field TEM image based on the diffraction peak of $1T'$ MoTe$_2$.

4.5 Exploring TEM window as a platform for studying electrochemistry on 2D materials

The inherent air sensitivity of transition metal dichalcogenides (TMDs), the minute dimensions of twisted 2D materials, and the potential instability of scanning electrochemical cell microscopy (SECCM) nanopipettes necessitate the exploration of new methods for probing electrochemical reactions on these materials. We have developed a method employing a transmission electron microscopy (TEM) membrane, specifically a 200 nm thick silicon nitride (SiN) layer, to conduct electrochemical reactions on designated regions of 2D materials. As depicted in Figure 4.7, a thin gold layer is evaporated onto the reverse side of the TEM grid to facilitate electrical contact. Using focused ion beam (FIB) technology, a small aperture with a 2 µm diameter is created to enable targeted electrochemical analysis.[135, 44]

The FIB setup employed utilized a scanning electron microscopy-focused ion beam with an

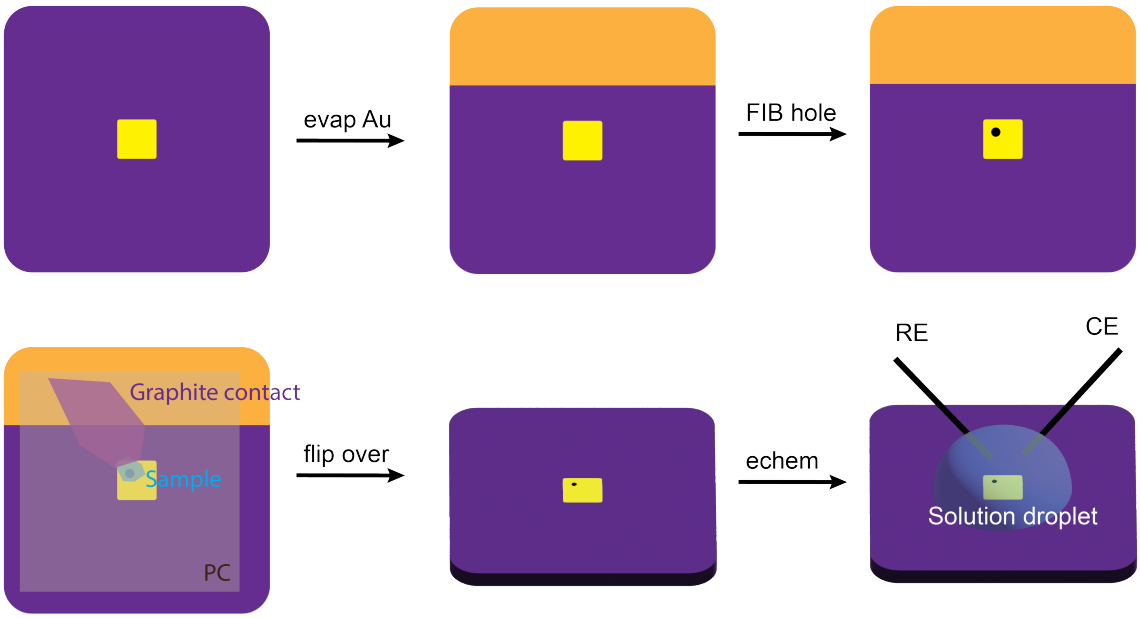

Figure 4.7: Schematic of TEM window electrochemistry sample preparation

accelerating voltage of 5 kV and a spot size of 5.5. Following the FIB process, a sample prepared using the PC/PDMS stamp method (described in Chapter 2) is meticulously aligned with the hole. An additional piece of graphite is picked up, ensuring a bridge between the sample and the gold contacts. The entire TEM grid is then inverted and affixed to a SiO_2/Si wafer by melting the polycarbonate (PC) at 170 °C.

The electrolyte solution is precisely deposited atop the FIB-created aperture. Care is taken when introducing the counter and reference electrodes into the solution to avoid damaging the membrane. The working electrode is directly connected to the gold-coated reverse side of the grid, ensuring a robust setup for detailed electrochemical analysis. This method allows for precise and localized electrochemical measurements, overcoming the challenges posed by the delicate nature of TMDs and the small scale of twisted 2D materials.

A working sample is shown in Figure 4.8a. This sample had a bilayer $1T'$ $MoTe_2$ positioned right on the FIB aperture (see Figure 4.8b). There are several advantage of using a TEM window. First, indium soldering will no longer be necessary. Therefore, sample fabrication can be fully conducted within the glovebox. Second, gold contacts can be fabricated in arbitrary geometry, allowing for multiple channels of bias. Third, the window opend by FIB can be shaped to fit the sample size. This is especially advantageous for materials that suffer from challenging fabrication process and small areal size. However, this method also risks leaking current through the membrane. Figure 4.8 shows a CV measured on a TEM membrane with gold contacts and no FIB hole or sample.

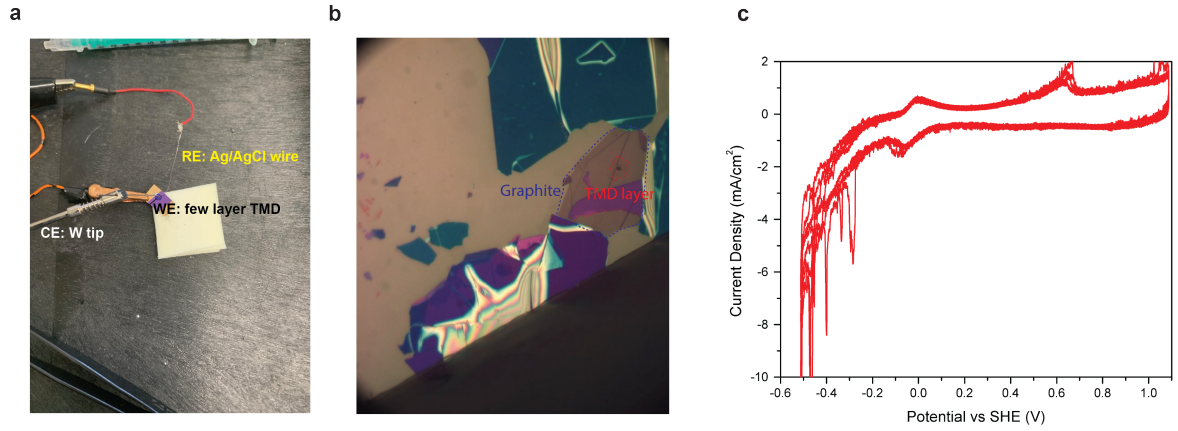

Figure 4.8: **a**, Image of an TEM electrochemistry sample setup. **b**, Optical micrograph of a bilayer $1T'$ $MoTe_2$ sample on a FIB engineered TEM window. **c**, Cyclic voltammogram measured on a TEM window with gold evaporated partially on one side. Scan rate: 100 mV/s

However, there is still significant current flowing, hinting at leakage through the SiO_2/Si. [198]. This leakage could have been caused by the gold evaporation over the edges of the TEM window. Therefore, future experiments utilizing this method can mask the edges during evaporation.

A practical example of this new method is illustrated in Figure 4.8a, where a bilayer $1T'$ $MoTe_2$ sample is precisely aligned over the FIB-created aperture, as shown in Figure 4.8b. Using a TEM window for electrochemical reactions offers several significant advantages. Firstly, the elimination of indium soldering simplifies the fabrication process, allowing all steps to be conducted within the controlled atmosphere of a glovebox. Secondly, the ability to fabricate gold contacts in various geometrical configurations enables the application of multiple bias channels, enhancing experimental flexibility. Thirdly, the FIB technique can tailor the window size to match that of the sample, which is particularly beneficial for materials that are difficult to fabricate or available only in small areas.

However, this method is not without its challenges. For instance, there is a potential risk of current leakage through the membrane. As depicted in Figure 4.8, a cyclic voltammetry (CV) experiment conducted on a TEM membrane equipped with gold contacts—but without a FIB hole or sample—still showed significant current flow, indicating leakage through the SiO_2/Si substrate.[198] This leakage might have been exacerbated by gold evaporation extending over the edges of the TEM window during fabrication. To mitigate this issue in future experiments, it is advisable to mask the edges during the gold evaporation process, thus ensuring the integrity and isolation of the electrochemical testing area.

4.6 Conclusion

The exploration of moiré superlattices within transition metal dichalcogenides (TMDs) marks a new direction in materials science, especially in catalytic applications such as the hydrogen evolution reaction (HER). The ability to precisely manipulate the electronic and structural properties of TMDs through controlled twisting and stacking presents new possibilities for enhancing catalytic efficiency and reactivity. This chapter has illustrated how variations in twist angle can alter the electrochemical properties of TMDs, potentially leading to the development of novel catalytic materials that may rival or even surpass traditional catalysts like platinum.

The deployment of advanced characterization techniques such as SECCM and TEM windows has opened new avenues for measuring catalytic reaction kinetics on twisted TMDs. However, these methods also present challenges that must be addressed to draw systematic conclusions. Future efforts will need to focus on refining these techniques and optimizing experimental conditions to ensure reliable results.

Moving forward, it will be crucial to further enhance the synthesis and manipulation methods of TMD moiré superlattices to achieve greater control over their properties. Additionally, tackling issues like scalability and stability under operational conditions will be essential for transitioning these materials from the lab to industrial applications. With ongoing research and innovation, the adjustable properties of TMD moiré superlattices promise to revolutionize the field of catalysis and expand their use in sustainable energy technologies.

Chapter 5

Conclusion and perspectives

Across the chapters presented in this thesis, we have explored the transformative potential of moiré superlattices in two-dimensional materials, with a focus on their electronic properties and implications for electrochemical applications. From understanding electron transfer kinetics in twisted bilayer and trilayer graphene to investigating hydrogen evolution kinetics in moiré-patterned transition metal dichalcogenides (TMDs), the insights gained underscore the significant impact of atomic-scale engineering on material functionalities. The interaction between twist angles, electronic structure, and local stacking configurations dramatically influences electrochemical reactivity and catalytic efficiency.

Looking ahead, the realm of 2D materials beckons with new opportunities. While electron transfer kinetics of $Ru(NH_3)_6^{3+}$ approach reversibility in twisted trilayer graphene, more complex structures such as twisted double bilayer graphene could be examined with different redox couples. Electrostatic gating has emerged as a versatile method for tuning electron transfer, offering opportunities to align band structures with specific molecular energies. Integrating electrostatic gating with moiré materials could further modify electrochemical reaction rates, opening new avenues for tuning specific catalytic reactions and advancing materials for sensing applications.

Additionally, the potential of Scanning Electrochemical Cell Microscopy (SECCM) as a local probe for electrochemical activities remains largely untapped. By fabricating smaller radius pipettes and stabilizing the reaction setup, we could potentially visualize differences in activity—or the lack thereof—across various stacking domains through direct probing.

The theoretical and experimental enhancement gap in twisted graphene also requires further elucidation. Future work should strive to bridge this gap by focusing on the microscopic origins of electron-transfer modulations in the context of reorganization energy, electronic coupling, and electric double-layer structure.

In the burgeoning field of moiré catalysis on TMDs, refining experimental techniques to draw systematic conclusions is essential. The scope should not be limited to group VI TMDs, as other layered materials also offer high potential for catalytic applications. Such efforts will pave the way for leveraging the unique properties of moiré superlattices in next-generation catalytic and electrochemical systems, potentially revolutionizing approaches to sustainable energy and beyond.

Bibliography

[1] Pulickel Ajayan, Philip Kim, and Kaustav Banerjee. “Two-dimensional van der Waals materials”. In: *Physics Today* 69.9 (2016), pp. 38–44.

[2] Jonathan S Alden et al. “Strain solitons and topological defects in bilayer graphene”. In: *PNAS* 110.28 (2013), pp. 11256–11260.

[3] Leon Balents et al. “Superconductivity and strong correlations in moiré flat bands”. In: *Nature Physics* 16.7 (2020), pp. 725–733.

[4] Allen J Bard, Larry R Faulkner, and Henry S White. *Electrochemical methods: fundamentals and applications*. John Wiley & Sons, 2022.

[5] Allen J Bard et al. “Scanning electrochemical microscopy. Introduction and principles”. In: *Analytical Chemistry* 61.2 (1989), pp. 132–138.

[6] Carlos MO Bastos et al. “Ab initio investigation of structural stability and exfoliation energies in transition metal dichalcogenides based on Ti-, V-, and Mo-group elements”. In: *Physical Review Materials* 3.4 (2019), p. 044002.

[7] Cameron L Bentley, Minkyung Kang, and Patrick R Unwin. “Nanoscale surface structure–activity in electrochemistry and electrocatalysis”. In: *J. Am. Chem. Soc.* 141.6 (2018), pp. 2179–2193.

[8] Cameron L Bentley et al. “Electrochemical maps and movies of the hydrogen evolution reaction on natural crystals of molybdenite (MoS 2): basal vs. edge plane activity”. In: *Chemical science* 8.9 (2017), pp. 6583–6593.

[9] Cameron L Bentley et al. “High-resolution ion-flux imaging of proton transport through graphene— nafion membranes”. In: *ACS nano* 16.4 (2022), pp. 5233–5245.

[10] Rafi Bistritzer and Allan H MacDonald. “Moiré bands in twisted double-layer graphene”. In: *PNAS* 108.30 (2011), pp. 12233–12237.

[11] Thomas Bligaard et al. “The Brønsted–Evans–Polanyi relation and the volcano curve in heterogeneous catalysis”. In: *Journal of catalysis* 224.1 (2004), pp. 206–217.

[12] Shannon W Boettcher and Yogesh Surendranath. “Heterogeneous electrocatalysis goes chemical”. In: *Nature Catalysis* 4.1 (2021), pp. 4–5.

[13] Marc Brunet Cabré et al. “Electrochemical kinetics as a function of transition metal dichalcogenide thickness”. In: *Electrochimica Acta* 393 (2021), p. 139027.

[14] Yang Cao. “Roadmap and direction toward high-performance MoS2 hydrogen evolution catalysts”. In: *ACS Nano* 15.7 (2021), pp. 11014–11039.

[15] Yuan Cao et al. “Correlated insulator behaviour at half-filling in magic-angle graphene superlattices”. In: *Nature* 556.7699 (2018), pp. 80–84.

[16] Yuan Cao et al. “Unconventional superconductivity in magic-angle graphene superlattices”. In: *Nature* 556.7699 (2018), pp. 43–50.

[17] Stephen Carr et al. “Relaxation and domain formation in incommensurate two-dimensional heterostructures”. In: *Phys. Rev. B* 98.22 (2018), p. 224102.

[18] John F Cassidy, Rafaela C de Carvalho, and Anthony J Betts. “Use of inner/outer sphere terminology in electrochemistry—a hexacyanoferrate II/III case study”. In: *Electrochem* 4.3 (2023), pp. 313–349.

[19] Guorui Chen et al. “Evidence of a gate-tunable Mott insulator in a trilayer graphene moiré superlattice”. In: *Nature Physics* 15.3 (2019), pp. 237–241.

[20] Guorui Chen et al. “Tunable correlated Chern insulator and ferromagnetism in a moiré superlattice”. In: *Nature* 579.7797 (2020), pp. 56–61.

[21] Jun Cheng et al. “Brønsted- Evans- Polanyi relation of multistep reactions and volcano curve in heterogeneous catalysis”. In: *The Journal of Physical Chemistry C* 112.5 (2008), pp. 1308–1311.

[22] Lei Cheng et al. “Scanning electrochemical cell microscopy platform with local electrochemical impedance spectroscopy”. In: *Analytical Chemistry* 93.49 (2021), pp. 16401–16408.

[23] Xinyi Chia and Martin Pumera. “Characteristics and performance of two-dimensional materials for electrocatalysis”. In: *Nature Catalysis* 1.12 (2018), pp. 909–921.

[24] Steven Chu and Arun Majumdar. “Opportunities and challenges for a sustainable energy future”. In: *nature* 488.7411 (2012), pp. 294–303.

[25] Richard Guy Compton and Craig E Banks. *Understanding voltammetry*. World Scientific, 2018.

[26] Chunxiao Cong et al. “Raman characterization of ABA-and ABC-stacked trilayer graphene”. In: *ACS Nano* 5.11 (2011), pp. 8760–8768.

[27] F Albert Cotton et al. *Advanced inorganic chemistry*. John Wiley & Sons, 1999.

[28] Ovidiu Cretu et al. “Migration and localization of metal atoms on strained graphene”. In: *Physical review letters* 105.19 (2010), p. 196102.

[29] Liming Dai et al. “Metal-free catalysts for oxygen reduction reaction”. In: *Chemical reviews* 115.11 (2015), pp. 4823–4892.

[30] Cory R Dean et al. “Hofstadter’s butterfly and the fractal quantum Hall effect in moiré superlattices”. In: *Nature* 497.7451 (2013), pp. 598–602.

[31] Andreas Dechant et al. “Geometric model of 3D curved graphene with chemical dopants”. In: *Carbon* 182 (2021), pp. 223–232.

[32] Dehui Deng et al. “Catalysis with two-dimensional materials and their heterostructures”. In: *Nature nanotechnology* 11.3 (2016), pp. 218–230.

[33] Trithep Devakul et al. “Magic in twisted transition metal dichalcogenide bilayers”. In: *Nature communications* 12.1 (2021), p. 6730.

[34] Yao Ding et al. “Stacking modes-induced chemical reactivity differences on chemical vapor deposition-grown trilayer graphene”. In: *ACS applied materials & interfaces* 10.27 (2018), pp. 23424–23431.

[35] Yao Ding et al. “Stacking-mode-induced reactivity enhancement for twisted bilayer graphene”. In: *Chemistry of Materials* 28.4 (2016), pp. 1034–1039.

[36] Neil Ebejer et al. “Localized high resolution electrochemistry and multifunctional imaging: Scanning electrochemical cell microscopy”. In: *Analytical chemistry* 82.22 (2010), pp. 9141–9145.

[37] Neil Ebejer et al. “Scanning electrochemical cell microscopy: a versatile technique for nanoscale electrochemistry and functional imaging”. In: *Annual review of analytical chemistry* 6 (2013), pp. 329–351.

[38] Drew Edelberg et al. “Approaching the intrinsic limit in transition metal diselenides via point defect control”. In: *Nano letters* 19.7 (2019), pp. 4371–4379.

[39] Rebecca Engelke et al. *Non-Abelian topological defects and strain mapping in 2D moiré materials*. 2022. DOI: 10.48550/ARXIV.2207.05276. URL: https://arxiv.org/abs/2207.05276.

[40] Royce C Engstrom and Christine M Pharr. “Scanning electrochemical microscopy”. In: *Analytical Chemistry* 61.19 (1989), 1099A–1104A.

[41] Andrea C Ferrari and Denis M Basko. “Raman spectroscopy as a versatile tool for studying the properties of graphene”. In: *Nature nanotechnology* 8.4 (2013), pp. 235–246.

[42] Ammon Fischer et al. “Unconventional superconductivity in magic-angle twisted trilayer graphene”. In: *npj Quantum Materials* 7.1 (2022), pp. 1–10.

[43] ZhuangEn Fu et al. “Layer and material-type dependent photoresponse in WSe2/WS2 vertical heterostructures”. In: *2D Materials* 9.1 (2021), p. 015022.

[44] Cian Gabbett et al. “Quantitative analysis of printed nanostructured networks using high-resolution 3D FIB-SEM nanotomography”. In: *Nature Communications* 15.1 (2024), p. 278.

[45] Xiaorong Gan et al. “2H/1T phase transition of multilayer MoS2 by electrochemical incorporation of S vacancies”. In: *ACS Applied Energy Materials* 1.9 (2018), pp. 4754–4765.

[46] Alejandro García-Miranda Ferrari et al. “Determination of the electrochemical area of screen-printed electrochemical sensing platforms”. In: *Biosensors* 8.2 (2018), p. 53.

[47] Hubert A Gasteiger and Nenad M Marković. "Just a dream—or future reality?" In: *science* 324.5923 (2009), pp. 48–49.

[48] Andre K Geim and Irina V Grigorieva. "Van der Waals heterostructures". In: *Nature* 499.7459 (2013), pp. 419–425.

[49] Andre K Geim and Konstantin S Novoselov. "The rise of graphene". In: *Nature materials* 6.3 (2007), pp. 183–191.

[50] H Gerischer. "Uber den Ablauf von Redoxreaktionen an Metallen und an Halbleitern". In: *Z. Phys. Chem. NF* 26 (1960), pp. 223–247. DOI: doi:10.1524/zpch.1960.26.3_4.223. URL: https://doi.org/10.1524/zpch.1960.26.3_4.223.

[51] H Gerischer. "Über den Ablauf von Redoxreaktionen an Metallen und an Halbleitern". In: *Zeitschrift für Physikalische Chemie* 26.3_4 (1960), pp. 223–247.

[52] Heinz Gerischer. "Electron-transfer kinetics of redox reactions at the semiconductor/electrolyte contact. A new approach". In: *The Journal of Physical Chemistry* 95.3 (1991), pp. 1356–1359. DOI: 10.1021/j100156a060. eprint: https://doi.org/10.1021/j100156a060. URL: https://doi.org/10.1021/j100156a060.

[53] Çağlar Ö Girit and Alex Zettl. "Soldering to a single atomic layer". In: *Applied Physics Letters* 91.19 (2007).

[54] Jeff Greeley et al. "Computational high-throughput screening of electrocatalytic materials for hydrogen evolution". In: *Nature materials* 5.11 (2006), pp. 909–913.

[55] Alexis Grimaud et al. "Anionic redox processes for electrochemical devices". In: *Nature materials* 15.2 (2016), pp. 121–126.

[56] Aleix G Guell et al. "Redox-dependent spatially resolved electrochemistry at graphene and graphite step edges". In: *ACS Nano* 9.4 (2015), pp. 3558–3571.

[57] Aleix G Güell et al. "Redox-dependent spatially resolved electrochemistry at graphene and graphite step edges". In: *ACS Nano* 9.4 (2015), pp. 3558–3571.

[58] Aleix G Güell et al. "Structural correlations in heterogeneous electron transfer at monolayer and multilayer graphene electrodes". In: *Journal of the American Chemical Society* 134.17 (2012), pp. 7258–7261.

[59] Zeyu Hao et al. "Electric field–tunable superconductivity in alternating-twist magic-angle trilayer graphene". In: *Science* 371.6534 (2021), pp. 1133–1138.

[60] Yongmin He et al. "Self-gating in semiconductor electrocatalysis". In: *Nature Materials* 18.10 (2019), pp. 1098–1104.

[61] Iddo Heller et al. "Electrochemistry at single-walled carbon nanotubes: the role of band structure and quantum capacitance". In: *Journal of the American Chemical Society* 128.22 (2006), pp. 7353–7359.

[62] Martin C Henstridge et al. "Marcus–Hush–Chidsey theory of electron transfer applied to voltammetry: A review". In: *Electrochim. Acta* 84 (2012), pp. 12–20.

[63] Joshua W Hill and Caleb M Hill. "Directly mapping photoelectrochemical behavior within individual transition metal dichalcogenide nanosheets". In: *Nano Letters* 19.8 (2019), pp. 5710–5716.

[64] Joshua W Hill and Caleb M Hill. "Directly visualizing carrier transport and recombination at individual defects within 2D semiconductors". In: *Chemical science* 12.14 (2021), pp. 5102–5112.

[65] Joshua W Hill et al. "Locally engineering and interrogating the photoelectrochemical behavior of defects in transition metal dichalcogenides". In: *The Journal of Physical Chemistry C* 124.31 (2020), pp. 17141–17149.

[66] Berit Hinnemann et al. "Biomimetic hydrogen evolution: MoS2 nanoparticles as catalyst for hydrogen evolution". In: *J. Am. Chem. Soc.* 127.15 (2005), pp. 5308–5309.

[67] Cameron F Holder and Raymond E Schaak. *Tutorial on powder X-ray diffraction for characterizing nanoscale materials*. 2019.

[68] Jonathan Hwang et al. "Perovskites in catalysis and electrocatalysis". In: *Science* 358.6364 (2017), pp. 751–756.

[69] Manoj K Jana et al. "Structure and Electron-Transport Properties of Anion-Deficient MoTe2: A Combined Experimental and Theoretical Study". In: *Zeitschrift für anorganische und allgemeine Chemie* 642.23 (2016), pp. 1386–1396.

[70] Thomas F. Jaramillo et al. "Identification of Active Edge Sites for Electrochemical H2 Evolution from MoS2 Nanocatalysts". In: *Science* 317.5834 (2007), pp. 100–102. ISSN: 0036-8075. DOI: 10.1126/science.1141483.

[71] Yuhang Jiang et al. "Charge order and broken rotational symmetry in magic-angle twisted bilayer graphene". In: *Nature* 573.7772 (2019), pp. 91–95.

[72] Zhenzhen Jiang et al. "MoS2 Moiré superlattice for hydrogen evolution reaction". In: *ACS Energy Letters* 4.12 (2019), pp. 2830–2835.

[73] Yan Jiao et al. "Activity origin and catalyst design principles for electrocatalytic hydrogen evolution on heteroatom-doped graphene". In: *Nature Energy* 1.10 (2016), pp. 1–9.

[74] Huanyu Jin et al. "Emerging two-dimensional nanomaterials for electrocatalysis". In: *Chemical reviews* 118.13 (2018), pp. 6337–6408.

[75] Rong Jin et al. "High spatial resolution electrochemical microscopic observation of enhanced charging under bias at active sites of N-rGO". In: *ACS Applied Energy Materials* 4.4 (2021), pp. 3502–3507.

[76] Rong Jin et al. "Highly spatial imaging of electrochemical activity on the wrinkles of graphene using all-solid scanning electrochemical cell microscopy". In: *Fundamental Research* 2.2 (2022), pp. 193–197.

[77] Apoorv Jindal et al. "Coupled ferroelectricity and superconductivity in bilayer Td-MoTe2". In: *Nature* 613.7942 (2023), pp. 48–52.

[78] Peng Kang et al. “Moiré impurities in twisted bilayer black phosphorus: Effects on the carrier mobility”. In: *Phys. Rev. B* 96.19 (2017), p. 195406.

[79] Nathanael P Kazmierczak et al. “Strain fields in twisted bilayer graphene”. In: *Nat. Mater.* 20.7 (2021), pp. 956–963.

[80] Dante M Kennes et al. “Moiré heterostructures as a condensed-matter quantum simulator”. In: *Nat. Phys.* 17.2 (2021), pp. 155–163.

[81] Alexander Kerelsky et al. “Maximized electron interactions at the magic angle in twisted bilayer graphene”. In: *Nature* 572.7767 (2019), pp. 95–100.

[82] Dong Hoon Keum et al. “Bandgap opening in few-layered monoclinic MoTe 2”. In: *Nature Physics* 11.6 (2015), pp. 482–486.

[83] Hyunjin Kim et al. “Evidence for unconventional superconductivity in twisted trilayer graphene”. In: *Nature* 606.7914 (2022), pp. 494–500.

[84] Kyounghwan Kim et al. “van der Waals heterostructures with high accuracy rotational alignment”. In: *Nano Letters* 16.3 (2016), pp. 1989–1995.

[85] Paul M Kirkman et al. “Spatial and temporal control of the diazonium modification of sp2 carbon surfaces”. In: *Journal of the American Chemical Society* 136.1 (2014), pp. 36–39.

[86] Akichika Kumatani et al. “Chemical dopants on edge of holey graphene accelerate electrochemical hydrogen evolution reaction”. In: *Advanced Science* 6.10 (2019), p. 1900119.

[87] Rachel Kurchin and Venkatasubramanian Viswanathan. “Marcus–Hush–Chidsey kinetics at electrode–electrolyte interfaces”. In: *J. Chem. Phys.* 153.13 (2020), p. 134706.

[88] AM Kuznetsov. *Charge transfer in physics, chemistry and biology: physical mechanisms of elementary processes and an introduction to the theory, 1st ed.* Gordon Breach, 1995.

[89] Sylvain Latil and Luc Henrard. “Charge carriers in few-layer graphene films”. In: *Phys. Rev. Lett.* 97.3 (2006), p. 036803.

[90] Tataiana Latychevskaia et al. “Stacking transition in rhombohedral graphite”. In: *Frontiers of Physics* 14.1 (2019), pp. 1–7.

[91] Chun Ning Lau et al. “Reproducibility in the fabrication and physics of moiré materials”. In: *Nature* 602.7895 (2022), pp. 41–50.

[92] En Li et al. “Lattice reconstruction induced multiple ultra-flat bands in twisted bilayer WSe2”. In: *Nat. Commun.* 12.1 (2021), p. 5601.

[93] Guoqing Li et al. “All the catalytic active sites of MoS2 for hydrogen evolution”. In: *Journal of the American Chemical Society* 138.51 (2016), pp. 16632–16638.

[94] Guoqing Li et al. “Engineering substrate interaction to improve hydrogen evolution catalysis of monolayer MoS2 films beyond Pt”. In: *ACS nano* 14.2 (2020), pp. 1707–1714.

[95] Hong Li et al. “Activating and optimizing MoS2 basal planes for hydrogen evolution through the formation of strained sulphur vacancies”. In: *Nature materials* 15.1 (2016), pp. 48–53.

[96] Hong Li et al. “From bulk to monolayer MoS2: evolution of Raman scattering”. In: *Advanced Functional Materials* 22.7 (2012), pp. 1385–1390.

[97] Hongyuan Li et al. “Global control of stacking-order phase transition by doping and electric field in few-layer graphene”. In: *Nano Letters* 20.5 (2020), pp. 3106–3112.

[98] Jinfeng Li et al. “Carbon-nanotube–electrolyte interface: quantum and electric double layer capacitance”. In: *ACS nano* 12.10 (2018), pp. 9763–9774.

[99] Mengge Li et al. “P-type doping in large-area monolayer MoS2 by chemical vapor deposition”. In: *ACS applied materials & interfaces* 12.5 (2020), pp. 6276–6282.

[100] Si-yu Li et al. “Imaging topological and correlated insulating states in twisted monolayer-bilayer graphene”. In: *Nature Communications* 13.1 (2022), pp. 1–7.

[101] L Libioulle, Y Houbion, and J-M Gilles. “Very sharp platinum tips for scanning tunneling microscopy”. In: *Rev. of Scientific Instruments* 66.1 (1995), pp. 97–100.

[102] Aditya M. Limaye, Wendu Ding, and Adam P. Willard. “Understanding attenuated solvent reorganization energies near electrode interfaces”. In: *J. of Chem. Phys.* 152.11 (2020), p. 114706.

[103] Dan-Qing Liu et al. “Adiabatic versus non-adiabatic electron transfer at 2D electrode materials”. In: *Nature Communications* 12.1 (2021), p. 7110.

[104] Dan-Qing Liu et al. “Metal support effects in electrocatalysis at hexagonal boron nitride”. In: *Chemical communications* 55.5 (2019), pp. 628–631.

[105] Song Liu et al. “Two-step flux synthesis of ultrapure transition-metal dichalcogenides”. In: *ACS nano* 17.17 (2023), pp. 16587–16596.

[106] Xiangye Liu et al. “The critical role of electrolyte gating on the hydrogen evolution performance of monolayer MoS2”. In: *Nano letters* 19.11 (2019), pp. 8118–8124.

[107] Yulong Liu et al. “Electrochemical visualization of gas bubbles on superaerophobic electrodes using scanning electrochemical cell microscopy”. In: *Analytical Chemistry* 93.36 (2021), pp. 12337–12345.

[108] Yulong Liu et al. “Visualization and quantification of electrochemical H2 bubble nucleation at Pt, Au, and MoS2 substrates”. In: *ACS sensors* 6.2 (2020), pp. 355–363.

[109] Xiaobo Lu et al. “Superconductors, orbital magnets and correlated states in magic-angle bilayer graphene”. In: *Nature* 574.7780 (2019), pp. 653–657.

[110] Chun Hung Lui et al. “Imaging stacking order in few-layer graphene”. In: *Nano Letters* 11.1 (2011), pp. 164–169.

[111] Chen Luo et al. “In Situ transmission electron microscopy characterization and manipulation of two-dimensional layered materials beyond graphene”. In: *Small* 13.35 (2017), p. 1604259.

[112] Rudolph A Marcus. “On the theory of oxidation-reduction reactions involving electron transfer. I”. In: *The Journal of chemical physics* 24.5 (1956), pp. 966–978.

[113] Ruperto G Mariano et al. “Selective increase in CO2 electroreduction activity at grain-boundary surface terminations”. In: *Science* 358.6367 (2017), pp. 1187–1192.

[114] Sonal Maroo et al. “Decoupling Effects of Electrostatic Gating on Electronic Transport and Interfacial Charge-Transfer Kinetics at Few-Layer Molybdenum Disulfide”. In: *ACS Nanosci. Au* 3.3 (2023), pp. 204–210.

[115] Leo J McGilly et al. “Visualization of moiré superlattices”. In: *Nat. Nanotechnol.* 15.7 (2020), pp. 580–584.

[116] Jessica C McGlynn et al. “Molybdenum ditelluride rendered into an efficient and stable electrocatalyst for the hydrogen evolution reaction by polymorphic control”. In: *Energy Technology* 6.2 (2018), pp. 345–350.

[117] Rafael G Mendes et al. “Electron-driven in situ transmission electron microscopy of 2D transition metal dichalcogenides and their 2D heterostructures”. In: *ACS nano* 13.2 (2019), pp. 978–995.

[118] Gioele Mirabelli et al. “Air sensitivity of MoS2, MoSe2, MoTe2, HfS2, and HfSe2”. In: *Journal of Applied Physics* 120.12 (2016).

[119] Mit H Naik et al. “Origin and evolution of ultraflat bands in twisted bilayer transition metal dichalcogenides: Realization of triangular quantum dots”. In: *Phys. Rev. B* 102.7 (2020), p. 075413.

[120] R Narayanan et al. “Dimensionality-dependent electrochemical kinetics at the single-layer graphene–electrolyte interface”. In: *The Journal of Physical Chemistry Letters* 8.17 (2017), pp. 4004–4008.

[121] Jens Kehlet Nørskov et al. “Towards the computational design of solid catalysts”. In: *Nature Chemistry* 1.1 (2009), pp. 37–46.

[122] Jens Kehlet Nørskov et al. “Trends in the exchange current for hydrogen evolution”. In: *Journal of The Electrochemical Society* 152.3 (2005), J23.

[123] Christina HM van Oversteeg et al. “In situ X-ray absorption spectroscopy of transition metal based water oxidation catalysts”. In: *Chemical Society Reviews* 46.1 (2017), pp. 102–125.

[124] Daniela Pacile et al. “Near-edge X-ray absorption fine-structure investigation of graphene”. In: *Physical review letters* 101.6 (2008), p. 066806.

[125] Matthieu Paillet et al. “Graphene and related 2D materials: An overview of the Raman studies”. In: *Journal of Raman Spectroscopy* 49.1 (2018), pp. 8–12.

[126] Daniel R Palo, Robert A Dagle, and Jamie D Holladay. “Methanol steam reforming for hydrogen production”. In: *Chemical reviews* 107.10 (2007), pp. 3992–4021.

[127] Jeong Min Park et al. “Tunable strongly coupled superconductivity in magic-angle twisted trilayer graphene”. In: *Nature* 590.7845 (2021), pp. 249–255.

[128] Youngju Park, Bheema Lingam Chittari, and Jeil Jung. “Gate-tunable topological flat bands in twisted monolayer-bilayer graphene”. In: *Phys. Rev. B* 102.3 (2020), p. 035411.

[129] William M Parkin et al. “Raman shifts in electron-irradiated monolayer MoS2”. In: *ACS nano* 10.4 (2016), pp. 4134–4142.

[130] Anisha N Patel, Kim McKelvey, and Patrick R Unwin. “Nanoscale electrochemical patterning reveals the active sites for catechol oxidation at graphite surfaces”. In: *Journal of the American Chemical Society* 134.50 (2012), pp. 20246–20249.

[131] Hollie V Patten et al. “Electrochemical Mapping Reveals Direct Correlation between Heterogeneous Electron-Transfer Kinetics and Local Density of States in Diamond Electrodes”. In: *Angew. Chem., Int. Ed.* 51.28 (2012), pp. 7002–7006.

[132] Sergey V Pavlov et al. “Role of graphene edges in the electron transfer kinetics: insight from theory and molecular modeling”. In: *J. of Phys. Chem. C* 123.11 (2019), pp. 6627–6634.

[133] David Polcari, Philippe Dauphin-Ducharme, and Janine Mauzeroll. “Scanning electrochemical microscopy: a comprehensive review of experimental parameters from 1989 to 2015”. In: *Chemical reviews* 116.22 (2016), pp. 13234–13278.

[134] Paola Quaino et al. “Volcano plots in hydrogen electrocatalysis–uses and abuses”. In: *Beilstein journal of nanotechnology* 5.1 (2014), pp. 846–854.

[135] Nitul S Rajput et al. “A user-friendly FIB lift-out technique to prepare plan-view TEM sample of 2D thin film materials”. In: *Ultramicroscopy* 235 (2022), p. 113496.

[136] Apoorva M Ranjekar and Ganapati D Yadav. “Steam reforming of methanol for hydrogen production: A critical analysis of catalysis, processes, and scope”. In: *Industrial & Engineering Chemistry Research* 60.1 (2021), pp. 89–113.

[137] Paul Sabatier. *La catalyse en chimie organique*. Vol. 3. C. Béranger, 1920.

[138] E Santos, T Iwasita, and W Vielstich. “On the use of the coulostatic method for the investigation of fast redox systems”. In: *Electrochim. Acta.* 31.4 (1986), pp. 431–437.

[139] E Santos, MTM Koper, and W Schmickler. “A model for bond-breaking electron transfer at metal electrodes”. In: *Chemical physics letters* 419.4-6 (2006), pp. 421–425.

[140] Elizabeth Santos, Paola Quaino, and Wolfgang Schmickler. “Theory of electrocatalysis: hydrogen evolution and more”. In: *Physical Chemistry Chemical Physics* 14.32 (2012), pp. 11224–11233.

[141] Elizabeth Santos and Wolfgang Schmickler. “Electrocatalysis of hydrogen oxidation—theoretical foundations”. In: *Angewandte Chemie International Edition* 46.43 (2007), pp. 8262–8265.

[142] Elizabeth Santos and Wolfgang Schmickler. “Fundamental aspects of electrocatalysis”. In: *Chem. Phys.* 332.1 (2007), pp. 39–47.

[143] Elizabeth Santos and Wolfgang Schmickler. “Models of electron transfer at different electrode materials”. In: *Chem. Rev.* 122.12 (2022), pp. 10581–10598.

[144] Wolfgang Schmickler and Elizabeth Santos. *Interfacial electrochemistry*. Springer Science & Business Media, 2010.

[145] Zhi Wei Seh et al. “Combining theory and experiment in electrocatalysis: Insights into materials design”. In: *Science* 355.6321 (2017), eaad4998.

[146] Jinbong Seok et al. “Active hydrogen evolution through lattice distortion in metallic MoTe2”. In: *2D Materials* 4.2 (2017), p. 025061.

[147] Sara Shabani et al. “Deep moiré potentials in twisted transition metal dichalcogenide bilayers”. In: *Nature Physics* 17.6 (2021), pp. 720–725.

[148] Mamta Devi Sharma, Chavi Mahala, and Mrinmoyee Basu. “2D thin sheet heterostructures of MoS2 on MoSe2 as efficient electrocatalyst for hydrogen evolution reaction in wide pH range”. In: *Inorganic Chemistry* 59.7 (2020), pp. 4377–4388.

[149] Aaron L Sharpe et al. “Emergent ferromagnetism near three-quarters filling in twisted bilayer graphene”. In: *Science* 365.6453 (2019), pp. 605–608.

[150] Cheng Shen et al. “Correlated states in twisted double bilayer graphene”. In: *Nature Physics* 16.5 (2020), pp. 520–525.

[151] Vojislav R Stamenkovic et al. “Energy and fuels from electrochemical interfaces”. In: *Nature materials* 16.1 (2017), pp. 57–69.

[152] “Strain solitons and topological defects in bilayer graphene”. In: *Proceedings of the National Academy of Sciences* 110.28 (July 2013), pp. 11256–11260.

[153] Lyndi E Strange et al. “Investigating the redox properties of two-dimensional MoS2 using photoluminescence spectroelectrochemistry and scanning electrochemical cell microscopy”. In: *The Journal of Physical Chemistry Letters* 11.9 (2020), pp. 3488–3494.

[154] Peng Sun and Michael V Mirkin. “Kinetics of electron-transfer reactions at nanoelectrodes”. In: *Analytical chemistry* 78.18 (2006), pp. 6526–6534.

[155] Yasufumi Takahashi et al. “High-Resolution Electrochemical Mapping of the Hydrogen Evolution Reaction on Transition-Metal Dichalcogenide Nanosheets”. In: *Angewandte Chemie International Edition* 59.9 (2020), pp. 3601–3608.

[156] Chaoliang Tan et al. “Recent advances in ultrathin two-dimensional nanomaterials”. In: *Chemical reviews* 117.9 (2017), pp. 6225–6331.

[157] Bijun Tang et al. “Recent advances in synthesis and study of 2D twisted transition metal dichalcogenide bilayers”. In: *Small Structures* 2.5 (2021), p. 2000153.

[158] Qing Tang. “Enhanced 1T-Phase Stabilization and Chemical Reactivity in a MoTe2 Monolayer through Contact with a 2D Ca2N Electride”. In: *ChemPhysChem* 20.4 (2019), pp. 595–601.

[159] Binglin Tao, Patrick R Unwin, and Cameron L Bentley. “Nanoscale variations in the electrocatalytic activity of layered transition-metal dichalcogenides”. In: *The Journal of Physical Chemistry C* 124.1 (2019), pp. 789–798.

[160] Shengdan Tao et al. “Designing ultra-flat bands in twisted bilayer materials at large twist angles: theory and application to two-dimensional indium selenide”. In: *J. Am. Chem. Soc.* 144.9 (2022), pp. 3949–3956.

[161] H Taube. “Mechanisms of redox reactions of simple chemistry”. In: *Advances in inorganic chemistry and radiochemistry*. Vol. 1. Elsevier, 1959, pp. 1–53.

[162] Chloe L Tolbert and Caleb M Hill. “Electrochemically probing exciton transport in monolayers of two-dimensional semiconductors”. In: *Faraday Discussions* 233 (2022), pp. 163–174.

[163] Ling-Hui Tong et al. “Spectroscopic visualization of flat bands in magic-angle twisted monolayer-bilayer graphene: coexistence of localization and delocalization”. In: *Physical Rev. Letters* 128.12 (2022), p. 126401.

[164] G Trambly de Laissardière, Didier Mayou, and Laurence Magaud. “Localization of Dirac electrons in rotated graphene bilayers”. In: *Nano letters* 10.3 (2010), pp. 804–808.

[165] Sergio Trasatti. “Work function, electronegativity, and electrochemical behaviour of metals: III. Electrolytic hydrogen evolution in acid solutions”. In: *Journal of Electroanalytical Chemistry and Interfacial Electrochemistry* 39.1 (1972), pp. 163–184.

[166] Charlie Tsai et al. “Electrochemical generation of sulfur vacancies in the basal plane of MoS2 for hydrogen evolution”. In: *Nature communications* 8.1 (2017), pp. 1–8.

[167] Charlie Tsai et al. “Theoretical insights into the hydrogen evolution activity of layered transition metal dichalcogenides”. In: *Surface Science* 640 (2015), pp. 133–140.

[168] Simon Turkel et al. “Orderly disorder in magic-angle twisted trilayer graphene”. In: *Science* 376.6589 (2022), pp. 193–199.

[169] Patrick R Unwin, Aleix G Guell, and Guohui Zhang. “Nanoscale electrochemistry of sp2 carbon materials: from graphite and graphene to carbon nanotubes”. In: *Acc. Chem. Res.* 49.9 (2016), pp. 2041–2048.

[170] Madeline Van Winkle et al. “Rotational and dilational reconstruction in transition metal dichalcogenide moiré bilayers”. In: *Nat. Commun.* 14.1 (2023), p. 2989.

[171] Péter Vancsó et al. “The intrinsic defect structure of exfoliated MoS2 single layers revealed by Scanning Tunneling Microscopy”. In: *Scientific reports* 6.1 (2016), p. 29726.

[172] Swapnil Varhade et al. “Elucidation of alkaline electrolyte-surface interaction in SECCM using a pH-independent redox probe”. In: *Electrochimica Acta* 460 (2023), p. 142548.

[173] Matej Velicky et al. “Electron transfer kinetics on mono-and multilayer graphene”. In: *ACS Nano* 8.10 (2014), pp. 10089–10100.

[174] OJ Wahab et al. “Proton transport through nanoscale corrugations in two-dimensional crystals”. In: *Nature* 620.7975 (2023), pp. 782–786.

[175] Lei Wang et al. “Correlated electronic phases in twisted bilayer transition metal dichalcogenides”. In: *Nat. Mater.* 19.8 (2020), pp. 861–866.

[176] Lei Wang et al. “Tunable intrinsic strain in two-dimensional transition metal electrocatalysts”. In: *Science* 363.6429 (2019), pp. 870–874.

[177] Yan Wang et al. “Field effect modulation of electrocatalytic hydrogen evolution at back-gated two-dimensional MoS2 electrodes”. In: *Nano letters* 19.9 (2019), pp. 6118–6123.

[178] Yan Wang et al. “Field effect modulation of heterogeneous charge transfer kinetics at back-gated two-dimensional MoS2 electrodes”. In: *Nano Lett.* 17.12 (2017), pp. 7586–7592.

[179] Jilin Xia et al. “Measurement of the quantum capacitance of graphene”. In: *Nature Nanotechnology* 4.8 (2009), pp. 505–509.

[180] Lingbin Xie et al. “WS2 moiré superlattices derived from mechanical flexibility for hydrogen evolution reaction”. In: *Nature Communications* 12.1 (2021), pp. 1–9.

[181] Pan Xiong et al. “Unilamellar metallic MoS2/graphene superlattice for efficient sodium storage and hydrogen evolution”. In: *ACS Energy Letters* 3.4 (2018), pp. 997–1005.

[182] Rui Xu et al. “Direct probing of the stacking order and electronic spectrum of rhombohedral trilayer graphene with scanning tunneling microscopy”. In: *Phys. Rev. B* 91.3 (2015), p. 035410.

[183] Shuigang Xu et al. “Tunable van Hove singularities and correlated states in twisted monolayer–bilayer graphene”. In: *Nature Physics* 17.5 (2021), pp. 619–626.

[184] Xiangdong Xu et al. “The new era of high-throughput nanoelectrochemistry”. In: *Analytical Chemistry* 95.1 (2023), pp. 319–356.

[185] Kai Yan et al. “Formation of bilayer bernal graphene: layer-by-layer epitaxy via chemical vapor deposition”. In: *Nano letters* 11.3 (2011), pp. 1106–1110.

[186] GM Yang et al. “Density functional theory calculations for the quantum capacitance performance of graphene-based electrode material”. In: *J. Phys. Chem. C* 119.12 (2015), pp. 6464–6470.

[187] Huan Yang et al. “On-chip electrocatalytic microdevice: an emerging platform for expanding the insight into electrochemical processes”. In: *Chemical Society Reviews* 49.10 (2020), pp. 2916–2936.

[188] Matthew Yankowitz et al. “Tuning superconductivity in twisted bilayer graphene”. In: *Science* 363.6431 (2019), pp. 1059–1064.

[189] Dongpei Ye and Shik Chi Edman Tsang. “Prospects and challenges of green ammonia synthesis”. In: *Nature Synthesis* 2.7 (2023), pp. 612–623.

[190] Hyobin Yoo et al. “Atomic and electronic reconstruction at the van der Waals interface in twisted bilayer graphene”. In: *Nat. Mater.* 18.5 (2019), pp. 448–453.

[191] Yun Yu, Madeline Van Winkle, and D. Kwabena Bediako. “Tuning interfacial chemistry with twistronics”. In: *Trends in Chemistry* 4 (2022), pp. 857–859.

[192] Yun Yu et al. “Tunable angle-dependent electrochemistry at twisted bilayer graphene with moiré flat bands”. In: *Nat. Chem.* 14.3 (2022), pp. 267–273.

[193] Yi Zeng et al. "Simple formula for Marcus–Hush–Chidsey kinetics". In: *Journal of Electroanalytical Chemistry* 735 (2014), pp. 77–83. ISSN: 1572-6657. DOI: https://doi.org/10.1016/j.jelechem.2014.09.038. URL: https://www.sciencedirect.com/science/article/pii/S1572665714004330.

[194] Kaidi Zhang et al. "Anomalous Interfacial Electron-Transfer Kinetics in Twisted Trilayer Graphene Caused by Layer-Specific Localization". In: *ACS Cent. Sci.* (2023).

[195] Kuan Zhang and Ellad B Tadmor. "Structural and electron diffraction scaling of twisted graphene bilayers". In: *J. Mech. Phys. Solids* 112 (2018), pp. 225–238.

[196] Shishu Zhang et al. "Spotting the differences in two-dimensional materials–the Raman scattering perspective". In: *Chemical Society Reviews* 47.9 (2018), pp. 3217–3240.

[197] Shuai Zhang et al. "Domino-like stacking order switching in twisted monolayer–multilayer graphene". In: *Nature Materials* 21.6 (2022), pp. 621–626.

[198] Weihang Zhang et al. "Analysis of leakage mechanisms in AlN nucleation layers on p-Si and p-SOI substrates". In: *IEEE Transactions on Electron Devices* 66.4 (2019), pp. 1849–1855.

[199] Xixia Zhang et al. "Flux method growth of bulk MoS 2 single crystals and their application as a saturable absorber". In: *CrystEngComm* 17.21 (2015), pp. 4026–4032.

[200] Yang Zhang, Claudia Felser, and Liang Fu. "Moiré metal for catalysis". In: (2021). DOI: 10.48550/ARXIV.2111.03058. URL: https://arxiv.org/abs/2111.03058.

[201] Zhiming Zhang et al. "Flat bands in twisted bilayer transition metal dichalcogenides". In: *Nature Physics* 16.11 (2020), pp. 1093–1096.

[202] Wei-Min Zhao et al. "Moiré enhanced charge density wave state in twisted 1T-TiTe2/1T-TiSe2 heterostructures". In: *Nature Materials* 21.3 (2022), pp. 284–289.

[203] Haihong Zheng et al. "Strain tuned efficient heterostructure photoelectrodes". In: *Chinese Chemical Letters* 33.3 (2022), pp. 1450–1454.

[204] Yao Zheng et al. "Hydrogen evolution by a metal-free electrocatalyst". In: *Nature communications* 5.1 (2014), p. 3783.

[205] Jin-Hui Zhong et al. "Quantitative correlation between defect density and heterogeneous electron transfer rate of single layer graphene". In: *Journal of the American Chemical Society* 136.47 (2014), pp. 16609–16617.

[206] Haoxin Zhou et al. "Superconductivity in rhombohedral trilayer graphene". In: *Nature* 598.7881 (2021), pp. 434–438.

[207] Yu Zhou et al. "Revealing the contribution of individual factors to hydrogen evolution reaction catalytic activity". In: *Advanced Materials* 30.18 (2018), p. 1706076.

[208] Pengcheng Zhu and Yuyuan Zhao. "Cyclic voltammetry measurements of electroactive surface area of porous nickel: Peak current and peak charge methods and diffusion layer effect". In: *Materials Chemistry and Physics* 233 (2019), pp. 60–67.

[209] Xiaohui Zhu, Chenyang Wang, and Lei Fu. “Engineering electrocatalytic microcells for two-dimensional materials”. In: *Cell Reports Physical Science* 1.9 (2020).

[210] Ziyan Zhu et al. “Twisted trilayer graphene: A precisely tunable platform for correlated electrons”. In: *Physical review letters* 125.11 (2020), p. 116404.